uOttawa

L'Université canadienne
Canada's university

FACULTÉ DES ÉTUDES SUPÉRIEURES ET POSTOCTORALES

uOttawa

L'Université canadienne
Canada's university

FACULTY OF GRADUATE AND POSDOCTORAL STUDIES

Delphine F. Courmier
AUTEUR DE LA THÈSE / AUTHOR OF THESIS

Ph.D. (Chemistry)
GRADE / DEGREE

Department of Chemistry
FACULTÉ, ÉCOLE, DÉPARTEMENT / FACULTY, SCHOOL, DEPARTMENT

The Reactivity of Water Ice and its Characterization by XAS

TITRE DE LA THÈSE / TITLE OF THESIS

Alain St-Amant
DIRECTEUR (DIRECTRICE) DE LA THÈSE / THESIS SUPERVISOR

John T. Tse
CO-DIRECTEUR (CO-DIRECTRICE) DE LA THÈSE / THESIS CO-SUPERVISOR

EXAMINATEURS (EXAMINATRICES) DE LA THÈSE / THESIS EXAMINERS

Javier Giorgi (absent)

Jim S. Wright

Peter Kusalik

Tom Woo

Gary W. Slater
Le Doyen de la Faculté des études supérieures et postdoctorales / Dean of the Faculty of Graduate and Postdoctoral Studies

The reactivity of water ice and its characterization by XAS

by

Delphine Félicie COURMIER

Thesis submitted to the
Faculty of Graduate & Postdoctoral Studies
In partial fulfillment of the requirements
for the PhD degree in Chemistry

Department of Chemistry
Faculty of Science
University of Ottawa

Your file Votre référence
ISBN: 978-0-494-41607-5
Our file Notre référence
ISBN: 978-0-494-41607-5

Author's Declaration

I hereby declare that I am the sole author of this thesis.
I authorize the University of Ottawa to lend this thesis to other institutions or individuals for the purpose of scholarly research.

I further authorize the University of Ottawa to reproduce this thesis by photocopying or by other means, in total or in part, at the request of other institutions or individuals for the purpose of scholarly research.

This work was evaluated by the following Committee:

Professor Alain St-Amant, Supervisor
Professor John S. Tse, Supervisor
Professor Javier B. Giorgi, Internal Examiner
Professor Tom K. Woo, Internal Examiner
Professor James S. Wright, Internal Examiner (Carleton)
Professor Peter G. Kusalik, External Examiner
Jérôme Doutriaux, representative of the Dean of FGPS

Abstract

Water seems at first sight to be a very simple substance. However, it possesses numerous anomalous properties, and despite the fact that a huge number of models have been developed, none can properly account for all those properties. Hydrogen bonded systems are of major interest in many different fields and water is perhaps the simplest model of a hydrogen bonded system.

The first section of this thesis focuses on the reactivity of hydrogen bonded systems. First, the reaction of formaldehyde with ammonia to generate NH_2CH_2OH, an amino acid precursor, is studied at various levels of theory. The reaction mechanism consists of a nucleophilic attack of the carbon by the lone pair on the nitrogen, accompanied by the simultaneous transfer of a proton to the formaldehyde oxygen. In the presence of water, the proton transfer occurs via a chain of proton transfers and the activation energy is lowered with the addition of two water molecules.

This first study having proven that water molecules can catalyze a reaction, another question arises: how do extended hydrogen bond networks modify the properties of water molecules. Water is well known to present cooperative effects. The present work tries to evaluate the extent of such an effect in water ice structures using both cluster and periodic models. The cooperative effect is shown to be very important. It is proven here that even if the charge transfer plays a major role for the shorter chains, electrostatic interactions become the most important factor as the chains lengthen. The extent of the cooperativity depends on the method and basis set employed, but whatever the methodology, a small cluster seems to be a very poor model to mimic the cooperativity present in ice structures.

Finally, the characterization of various ice and water structures are studied by means of calculated X-ray absorption spectra. DFT calculations have been performed on spherical clusters cut out from the experimental structures of the four proton ordered ices, i.e. ices II, VIII, IX and XI as well as on water and various amorphous ice structures ranging between

the HDA and LDA structures. The influence of the periodic crystalline environment is examined by computing spectra calculated for the naked clusters and for the same clusters surrounded by point charge distributions designed to reproduce the Madelung potential of the crystal. A systematic study of the influence of the size of the quantum cluster is also performed. Small clusters (70 water molecules, radius $\approx$ 7Å) can be used, as long as the cluster is subjected to a converged Madelung potential and the total dipole moment of the cluster is small. In the case of water and amorphous ices, sampling a large number of oxygen centers is required to obtain a converged spectrum. The directly bound nearest neighbors of the active oxygen center have been reported to exert considerable influence on the spectral lineshape. Therefore, a study of the influence of the basis set on those nearest neighbors is performed. The outer coordination shells and the long-range electrostatic potential must be taken into account in a quantitative simulation. A reasonable agreement is obtained with experimental results. However, while the method used here seems to perform well in the pre-edge region, it fails to reproduce the post-edge region exactly as a localized basis set, even one including diffuse functions, cannot account for a delocalized band structure. In the case of amorphous ices, for which calculated spectra do not provide good results, multiple electron transitions might have to be considered in the calculation of X-ray absorption spectra.

Acknowledgements

Le présent travail a pu être réalisé grâce à l'aide de plusieurs personnes. Je dois d'abord remercier le professeur Dennis Salahub qui m'a permis de venir pour la premiere fois à Montréal puis de revenir à Ottawa.

Je dois bien sur un grand merci à mes superviseurs, les professeurs Alain St-Amant et John Tse pour avoir encadré et guidé mon travail.

Je tiens à remercier tous les membres du groupe passés et présents aussi bien à l'université qu'au NRC Etienne Paradis, Sébastien Osborne, Daniel Matusek, Michelle Shaw, Seongho Moon, Gwang-Soo Kim...sans oublier les membres du groupe de Tom Woo, Federico Zahariev, David Gerbasi, Chris Rowley, James Hooper qui m'ont aidée par leurs questions et suggestions lors des group meeting et je ne dois pas oublier les membres du département de chimie qui m'ont aidée pour les TAs et l'enseignement et en premier Dan, Bob et Jenny.

Je dois aussi un merci tout particulier au Dr Serguei Partchkovskii pour l'aide qu'il m'a apportée en tout ce qui concerne le chapitre sur les calculs XAS ainsi qu'au Dr Dennis Klug qui m'a permis de rester au NRC après le départ de John.

Je remercie spécialement mes amis Dennis Ramos et Michelle Shaw pour leur aide précieuse dans la correction et le formatage de ma thèse.

Je tiens enfin a remercier ma famille et mes amis pour leur soutien et leur affection et en tout premier lieu mon père qui m'a toujours soutenue dans mes choix et encouragée et qui est un support infaillible.

Dedication

A mon père.

Table of Contents

List of Figures

List of Tables

General Introduction

A theme connecting the thesis research is the study of cooperativity in H-bonded systems. Cooperativity, or cooperative effect, is a phenomenon, most common in biochemistry, displayed by macromolecules such as enzymes or receptors that have multiple binding sites. It is characterized by changes in the affinity for ligands when the amount of ligands already bound increases. If the binding of a ligand at one site increases the affinity for ligand at another site, the macromolecule is said to exhibit positive cooperativity. On the other hand, the macromolecule exhibits negative cooperativity or anticooperativity if the binding of a ligand at one site lowers the affinity for a ligand at another site.

Cooperativity is also observed in large chain molecules comprise of identical subunits such as DNA, proteins, and phospholipids, when a substrate binds to the active site of one subunit and the rest of the subunits are stimulated and become active. This can be the case when those macromolecules undergo phase transitions such as melting, unfolding or unwinding.

On a more general perspective, cooperativity also affects the energetic of chemical processes. A chemical reaction involving multiple units, can be enhanced or hindered by the addition of multiple independent units. A classic example is the unwinding of DNA. Cooperativity among adjacent DNA nucleotides facilitates the unwinding of a whole group of adjacent nucleotides (called the cooperative unit size) compare to unwinding the same number of nucleotides spread out along the DNA chain. Other examples of the importance of cooperativity in biological processes are the folding and unfolding of proteins and the melting of phospholipid chains that make up the membranes of cells.

Entropy can play a major role in cooperativity. For example, the binding affinity of haemoglobin for oxygen is increased by the oxygen saturation of the macromolecule. When

a subunit protein in haemoglobin becomes oxygenated, a conformational change is induced in the whole complex, causing the other subunits to gain an increased affinity for oxygen. The first oxygen has four different places available for binding (higher entropy) when the last oxygen has only one site where it can bind. Going from the non-oxygenated to the 4-oxygenated haemoglobin structures, the first oxygen must overcome a larger entropy change than the last oxygen. This entropy difference is a major reason of the cooperativity in binding oxygen to haemoglobin.

Several models have been proposed to account for the binding cooperativity observed in proteins. In the MWC (Monod-Wyman-Changeux) model, the protein possesses two states of different affinity: a low-affinity state and a high-affinity state. The low-affinity state being thermodynamically favored, at low amounts of bound ligand. On the other hand, as the amount of bound ligand increases, the protein favours the high-affinity state. Unfortunately, this model cannot be used to explain anticooperativity. A second model is the KNF (Koshland-Némethy-Filmer) sequential model, in which ligand binding at one site is assume to cause a local conformational change, called induced fit, that causes small conformational changes at nearby binding sites consequently affecting their affinity for ligands. In this model, the protein has many different conformational states, corresponding to all possible modes of ligand binding. Unfortunately, none of these models elucidate the origin of cooperativity and, therefore, are not expected to be completely reliable models.

The origin of cooperativity is the subject of much debate. Some studies have suggested that an electrostatic model could fully describe these effects. Therefore, they were not produced by electron delocalization in the hydrogen-bonded systems [1-3]. In response to an external electric field generated by a neighbouring molecule, the molecular charge distribution polarizes, resulting in induced dipoles and electric moments of higher order. The strength of this electrostatic interaction is further influenced by the presence of other molecules, constituting a non-additive effect [4]. On the other hand, charge transfer was also

presented as a major factor [5, 6] and electron density redistribution has been shown to be associated with hydrogen bonding interactions.

Interactions among water molecules are the key to a proper description of a water model that is essential to so many biological, chemical and physical processes. Water structures, particularly in their crystalline forms of ice, where the hydrogen bonds are similar, represent ideal models to study cooperativity as they allow an easier account of cooperativity.

The presentation of this thesis is as follows. After a description of the theoretical background and the hydrogen bonded H_2O structures studied, results of three projects will be discussed. The first project is on the study of the catalytic formation of an amino alcohol by lengthening the chain of water molecules involved in the reaction. The second project concerns with the semi quantitative evaluation of cooperativity in ice in order to determine the minimum size a cluster can have such that it can be used to mimic the cooperative effects in bulk ice. Finally, the last project is devoted to the investigation of the local structure of liquid water on the X-ray absorption spectra. It demonstrated the importance of including cooperativity, through the Madelung potential, is needed in order to obtain reasonable agreement with experiment.

Chapter 1
Theoretical Background

The Schrödinger equation can be solved exactly for only a few problems. However, a large variety of computational methods have been developed to find approximate solutions. Hartree-Fock theory is a basic model to solve many-electron problems and is the starting point for more complicated and accurate approximations.

1.1 Approximate solutions to the Schrödinger equation

The stationary state of an isolated system (atom or molecule) comprised of M nuclei and N electrons can be described by a wave function Φ that is continuous and differentiable at every point and that is an eigenfunction of the time-independent Schrödinger equation [7-11]. Hartree-Fock theory states that each electron can be described by a single-particle function or orbital which does not depend explicitly on the instantaneous positions of the other electrons. These orbitals only approximate reality, except for one electron atoms whose orbitals are exact eigenfunctions of the full electronic Hamiltonian [7-11].

1.1.1 The Variation Method

Generally speaking, the variation method is an important approach to finding approximate solutions to the eigenvalue problem. It is particularly useful for the time-independent Schrödinger equation:

$$H|\Phi>=E|\Phi> \qquad 1\text{-}1$$

where H is the hermitian Hamiltonian operator, $|\Phi>$ the wave function and E the energy.

The variation principle states that given a normalized wave function $\tilde{\Phi}$ that satisfies the appropriate boundary conditions (the wave function vanishes at infinity), the expectation value of the Hamiltonian is an upper bound to the exact ground state energy:

$$\left\langle \tilde{\Phi} \middle| H \middle| \tilde{\Phi} \right\rangle \geq E_0 \qquad 1\text{-}2$$

This implies, for the ground state, that the energy of an approximate wave function is always too high. Therefore, the energy is a good measure of the quality of a wave function in that the lower the energy, the better the wave function. The variation principle is the basis of the variation method in which we take a normalized trial function which depends on certain parameters and vary these parameters until the expectation value reaches a minimum. This is the variational estimate of the exact ground state energy. If only linear variations of the trial functions are allowed

$$\left| \tilde{\Phi} \right\rangle = \sum_{i=1}^{N} c_i \left| \Psi_i \right\rangle \qquad 1\text{-}3$$

where $\{|\Psi_i\rangle\}$ is a fixed set of N basis functions, then the problem of finding the optimum set of coefficients $\{c_i\}$ can be reduced to a matrix diagonalization HC=EC.

1.1.2 The Born-Oppenheimer Approximation

In atomic units, the non-relativistic time-independent Schrödinger equation, the Hamiltonian for N electrons and M nuclei can be written as:

$$H = \underbrace{-\sum_{i=1}^{N}\frac{1}{2}\nabla_i^2}_{\text{kinetic energy of electrons}} \underbrace{-\sum_{A=1}^{M}\frac{1}{2M_A}\nabla_A^2}_{\text{kinetic energy of nuclei}} \underbrace{-\sum_{i=1}^{N}\sum_{A=1}^{M}\frac{Z_A}{r_{iA}}}_{\text{Coulomb attraction between electrons and nuclei}} + \underbrace{\sum_{i=1}^{N}\sum_{j>i}^{N}\frac{1}{r_{ij}}}_{\text{repulsion between electrons}} + \underbrace{\sum_{A=1}^{M}\sum_{B>A}^{M}\frac{Z_A Z_B}{R_{AB}}}_{\text{repulsion between nuclei}} \quad 1\text{-}4$$

where M_A is the ratio of the mass of nucleus A to the mass of an electron and Z_A is the atomic number of nucleus A.

Nuclei are much heavier than electrons and therefore they move more slowly. Hence, N electrons in a molecule can be considered to be moving in the field of the M fixed nuclei. Within this approximation, the kinetic energy of the nuclei can be neglected and the repulsion between the nuclei can be considered to be constant. The nuclei are treated as classic distinguishable particles. The remaining terms in the Hamiltonian form the electronic Hamiltonian describing the motion of N electrons in the field of M point charges:

$$E_{tot} = E_{elec} + \sum_{A=1}^{M}\sum_{B>A}^{M}\frac{Z_A Z_B}{R_{AB}} \quad 1\text{-}5$$

The electronic Schrödinger equation becomes:

$$H_{elec}\Phi_{elec} = E_{elec}\Phi_{elec} \quad 1\text{-}6$$

where

$$H_{elec} = -\frac{1}{2}\sum_{i=1}^{N}\nabla_i^2 - \sum_{i=1}^{N}\sum_{A=1}^{M}\frac{Z_A}{r_{iA}} + \sum_{i=1}^{N}\sum_{j>i}^{N}\frac{1}{r_{ij}} \quad 1\text{-}7$$

1.1.3 The Antisymmetry or Pauli Exclusion Principle

The electronic Hamiltonian depends only on the spatial coordinates of the electrons but to completely describe a fermion (electron), it is also necessary to specify its spin in the wave function. Spin will be described by two spin functions $\alpha(\omega)$ and $\beta(\omega)$, ω being a spin variable. Those two spin functions form a complete and orthonormal set. An electron is now described by three spatial coordinates and one spin coordinate $x=\{\mathbf{r}, \omega\}$. The wave function for an N-electrons system is a function of $x_1, x_2, \ldots, x_N$ and the spatial orbital $\varphi(r)$ now becomes a spin orbital $\chi(x)$, the product of a spatial orbital with the spin function.

If the electrons ignore each other, then the Hamiltonian would be separable, and the total electronic wave function would just be the product of atomic wave functions (spin orbitals). A wave function of this general form is known as a Hartree product:

$$\Psi_{\text{Hartree-product}}(x_1, x_2, \cdots, x_N) = \chi_1(x_1)\chi_2(x_2)\cdots\chi_N(x_N) \qquad 1\text{-}8$$

This functional form fails to satisfy the antisymmetry principle, which states that a many-electron wave function must be antisymmetric with respect to the interchange of the coordinate x of any two electrons. This requirement is implied by the Pauli exclusion principle, which strictly forbid the coordinates x_i and x_j of two electrons to be the same (Fermi hole).

To tackle this problem, a determinant of spin orbitals, called a Slater determinant, can be introduced. Thanks to this functional form, the electrons are all indistinguishable, consistent with the principles of quantum mechanics.

$$\Psi(1,2,\ldots,N) = \frac{1}{\sqrt{N!}}\begin{vmatrix} \chi_1(x_1) & \chi_2(x_1) & \cdots & \chi_N(x_1) \\ \chi_1(x_2) & \chi_2(x_2) & \cdots & \chi_N(x_2) \\ \vdots & \vdots & \ddots & \vdots \\ \chi_1(x_N) & \chi_2(x_N) & \cdots & \chi_N(x_N) \end{vmatrix} = \frac{1}{\sqrt{N!}}\left|\chi_1\chi_2\cdots\chi_N\right\rangle \qquad 1\text{-}9$$

A Slater determinant is equivalent to the assumption that each electron moves independently of all the others except that it feels the repulsion due to the *average* positions

of all electrons. Hence, Hartree-Fock theory is also referred to as an independent particle model or a mean field theory.

1.1.4 Hartree-Fock Theory

The Hartree-Fock method, following the variational principle, seeks to approximately solve the electronic Schrödinger equation. It assumes that the wave function can be approximated by a single Slater determinant.

Applying the variational theorem to the spin orbitals and constraining them to remain orthonormal (i.e. the overlap between spin orbitals i and j is given by $\langle i \mid j \rangle = \int \chi_i^*(x)\chi_j(x)dx = \delta_{ij}$ with Lagrange multipliers, one can obtain the Hartree-Fock equation in terms of new operators:

$$\left[h(1) + \sum_{j \neq i} J_j(1) - \sum_{j \neq i} K_j(1) \right] \chi_i(1) = \varepsilon_i \chi_i(1) \qquad 1\text{-}10$$

where ε_i is the energy eigenvalue associated with orbital χ_i. The first term in equation 1-10 is the core Hamiltonian one electron operator that is the kinetic energy and potential energy of the attraction to the nuclei of a single electron:

$$\hat{h}(i) = -\frac{1}{2}\nabla_i^2 - \sum_{A=1}^{M} \frac{Z_A}{r_{iA}} \qquad 1\text{-}11$$

The associated energy is given by:

$$\langle i|h|j\rangle = \int dx \chi_i^*(x) h(r_i) \chi_j(x) \qquad 1\text{-}12$$

The second term in equation 1-10 gives the Coulomb interaction or average local potential of an electron in spin orbital χ_i with the average charge distribution of the other electrons. This is called the Coulomb term, and this two-electron operator is defined as:

$$\hat{J}_j(1)\chi_i(1) = \left[\int_{x_2} \chi_j^*(2)\frac{1}{r_{12}}\chi_j(2)dx_2\right]\chi_i(1) \qquad 1\text{-}13$$

The last term in equation 1-10 does not have a simple classical analog and arises from the antisymmetry requirement of the wave function. Hence, it is called the exchange term and the two-electron exchange operator is defined as:

$$\hat{K}_j(1)\chi_i(1) = \left[\int_{x_2} \chi_j^*(2)\frac{1}{r_{12}}\chi_i(2)dx_2\right]\chi_j(1) \qquad 1\text{-}14$$

The energy associated with a two-electron integral is:

$$[ij|kl] = \int dx_1 dx_2 \chi_i^*(x_1)\chi_j(x_1)\frac{1}{r_{12}}\chi_k^*(x_2)\chi_l(x_2) \qquad 1\text{-}15$$

Hence, the Fock operator is defined as:

$$\hat{f}_i = \hat{h}(i) + \sum_{j=1}^{N}\left[\hat{J}_j(i) - \hat{K}_j(i)\right] \qquad 1\text{-}16$$

And the Hartree-Fock equations are given by:

$$f(1)\chi_i(1) = \varepsilon_i\chi_i(1) \qquad 1\text{-}17$$

The Fock operator is hermitian. Therefore, its eigenfunctions form a complete and infinite set. The total Hartree-Fock energy is now given by:

$$E_{HF} = \langle \Phi_0 | H | \Phi_0 \rangle = \sum_i \langle i | \hat{h} | i \rangle + \frac{1}{2} \left\{ \sum_{ij} [ii|jj] - [ij|ji] \right\} + \sum_{A<B} \frac{Z_A Z_B}{R_{AB}} \qquad 1\text{-}18$$

The Hartree-Fock equations can be solved either numerically or they can be solved in the space spanned by a set of basis functions by varying the parameters until the electronic energy E_{elec} is minimized. Introducing a basis set transforms the Hartree-Fock equations into the Roothaan equations. $\tilde{\chi}$ being the atomic orbital basis functions, one obtains the following expansion for each spin orbital i:

$$\chi_i = \sum_{\mu=1}^{K} C_{\mu i} \tilde{\chi}_\mu \qquad 1\text{-}19$$

Substituting in equation 1-17, multiplying by $\tilde{\chi}_\mu^*(1)$, and integrating yields, after introducing the matrix element notation $S_{\mu\nu}$ and $F_{\mu\nu}$, the Hartree-Fock-Roothaan equations:

$$\sum_v F_{\mu\nu} C_{vi} = \varepsilon_i \sum_v S_{\mu\nu} C_{vi} \qquad 1\text{-}20$$

or even more simply:

$$FC = SC\varepsilon \qquad 1\text{-}21$$

where

$$S_{\mu\nu} = \int dx_1 \tilde{\chi}_\mu^*(x_1) \tilde{\chi}_\nu(x_1)$$
$$F_{\mu\nu} = \int dx_1 \tilde{\chi}_\mu^*(x_1) \hat{f} \tilde{\chi}_\nu(x_1) \qquad 1\text{-}22$$

ε is a diagonal matrix of the orbital energies. A transformation of basis can be performed to obtain an orthogonal basis and therefore make S vanish. Since F depends on its own solution through the orbitals, the process must be done iteratively. Therefore, a starting guess of initial orbitals is needed and then an iterative procedure called a self-consistent-field (SCF) approach refines the guess [7-11].

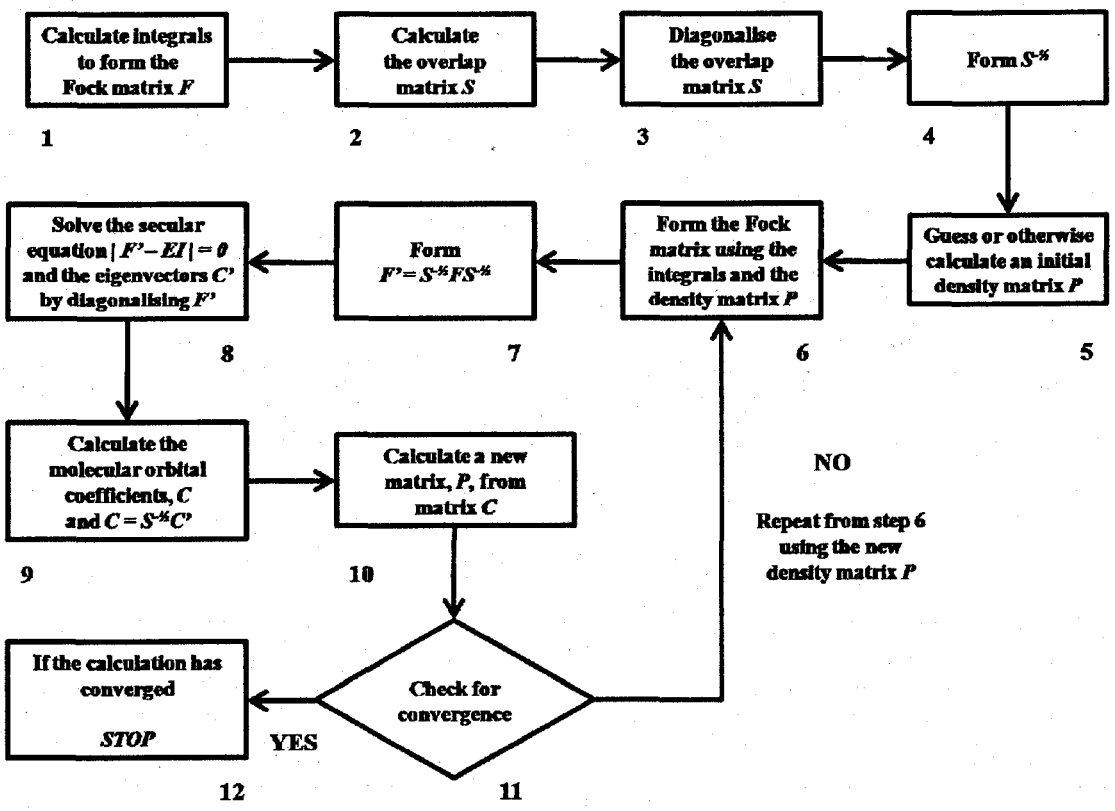

Figure 1-1 Flowchart of the Hartree-Fock-Roothaan procedure [12].

1.2 Post Hartree-Fock Methods

The SCF procedure makes several assumptions about the multi-body Schrödinger equation:

- The Born-Oppenheimer approximation
- The relativistic effects are completely neglected
- The basis set is composed of a finite number of functions
- The effects of electron correlation are completely neglected

With a good basis set, neglecting electron correlation is the most serious simplification, often leading to large deviations from experimental results. Post Hartree-Fock methods are the methods that have been devised to improve the Hartree-Fock method by including electron correlation with the multi-electron wave function. Most of those methods use as a starting point the Hartree-Fock wave function and then develop further from it. In fact, the definition of the correlation energy given by Löwdin is: $E_{corr} = E_{exact}^{\text{Non Relativistic}} - E_{HF}$

A number of different approaches are available, but only those used in the present work will be introduced here.

1.2.1 Moller-Plesset perturbation theory

Møller-Plesset perturbation theory, derived from Rayleigh-Schrödinger perturbation theory, includes in an approximate fashion, the effect of the electron correlation, mostly the dynamic correlation [7, 13-22]. The dynamic correlation, a consequence of the Coulomb hole, enables the electrons to stay apart and is, usually, the largest part of the total correlation. The static correlation represents the error introduced by the limitation of a single Slater

determinant in the HF wavefunction. In this method, the true Hamiltonian operator of a molecular system $\hat{H}$ is separated into two different contributions: a zeroth-order, unperturbed Hartree-Fock Hamiltonian $\hat{H}_0$ for which the energies and wave functions are known, and a perturbation $\hat{V}$ [7, 13-22].

$$\hat{H} = \hat{H}_0 + \lambda\hat{V} \qquad 1\text{-}23$$

λ is a parameter that can vary between 0 and 1 in order to gradually improve the eigenfunctions and eigenvalues of H. The eigenfunctions of the true Hamiltonian operator are Ψ_i with corresponding eigenvalues E_i. The eigenfunctions of the zeroth-order Hamiltonian are $\Psi_i^{(0)}$ with the energies $E_i^{(0)}$. If the perturbation is sufficiently small, the eigenfunctions and eigenvalues of $\hat{H}$ can be developed using the Taylor series expansion, in powers of λ:

$$\Psi_i = \Psi_i^{(0)} + \lambda\Psi_i^{(1)} + \lambda^2\Psi_i^{(2)} + \cdots = \sum_{n=0} \lambda^n \Psi_i^{(n)} \qquad 1\text{-}24$$

$$E_i = E_i^{(0)} + \lambda E_i^{(1)} + \lambda^2 E_i^{(2)} + \cdots = \sum_{n=0} \lambda^n E_i^{(n)} \qquad 1\text{-}25$$

where $E_i^{(n)}$ is the nth-order correction to the energy. These corrections to the energy can be calculated from the eigenfunctions as follows:

$$E_i^{(0)} = \int \Psi_i^{(0)} H_0 \Psi_i^{(0)} d\tau,\ E_i^{(1)} = \int \Psi_i^{(0)} V\ \Psi_i^{(0)} d\tau$$
$$E_i^{(2)} = \int \Psi_i^{(0)} V\ \Psi_i^{(1)} d\tau,\ E_i^{(3)} = \int \Psi_i^{(0)} V\ \Psi_i^{(2)} d\tau, \ldots \qquad 1\text{-}26$$

This requires the determination of the wave functions to a given order. In Møller-Plesset perturbation theory the unperturbed Hamiltonian $\hat{H}_0$ is the sum of the one-electron Fock operators for the N electrons:

$$\hat{H}_0 = \sum_{i=1}^{N} \hat{f}_i = \sum_{i=1}^{N} \left(\hat{h}(i) + \sum_{j=1}^{N} \left[\hat{J}_j(i) + \hat{H}_j(i) \right] \right) \qquad 1\text{-}27$$

The Hartree-Fock wave function $\Psi_0^{(0)}$ is an eigenfunction of $\hat{H}_0$ and its corresponding zeroth-order energy $E_0^{(0)}$ is equal to the sum of the orbital energies for the occupied molecular orbitals $E_0^{(0)} = \sum_{i=1}^{occupied} \varepsilon_i$.

The true Hamiltonian is equal to the sum of the nuclear attraction terms and electron repulsion terms:

$$\hat{H} = \sum_{i=1}^{N} \left(\hat{h}^{core} \right) + \sum_{i=1}^{N} \sum_{j=i+1}^{N} \frac{1}{r_{ij}} \qquad 1\text{-}28$$

The perturbation $\hat{V}$ is therefore given by:

$$\hat{V} = \hat{H} - \hat{H}_0 = \sum_{i=1}^{N} \sum_{j=i+1}^{N} \frac{1}{r_{ij}} - \sum_{j=1}^{N} \left(J_j + K_j \right) \qquad 1\text{-}29$$

The first-order energy is then defined as:

$$E_0^{(1)} = -\frac{1}{2} \sum_{i=1}^{N} \sum_{j=1}^{N} \frac{1}{r_{ij}} \left([ii|jj] - [ij|ij] \right) \qquad 1\text{-}30$$

Hence, the sum of the zeroth-order and first-order energies corresponds to the Hartree-Fock energy: $E_0^{(0)} + E_0^{(1)} = \sum_{i=1}^{N} \varepsilon_i - \frac{1}{2} \sum_{i=1}^{N} \sum_{j=1}^{N} \left([ii|jj] - [ij|ij] \right)$. To obtain an improvement, it is necessary to go beyond the first order and use at least second order (MP2).

The higher-order wave function $\Psi_0^{(1)}$ is expressed as linear combinations of solutions to the zeroth-order Hamiltonian: $\Psi_0^{(1)} = \sum_j c_j^{(1)} \Psi_j^{(0)}$. $\Psi_j^{(0)}$ includes single, double, ... excitations obtained by promoting electrons into the virtual orbitals obtained from a Hartree-Fock calculation. For example, the second-order energy (MP2) is given by:

$$E_0^{(2)} = \sum_{i}^{\text{occupied}} \sum_{j>1}^{\text{occupied}} \sum_{a}^{\text{virtual}} \sum_{b>a}^{\text{virtual}} \frac{\int\int d\tau_1 d\tau_2 \chi_i(2)\chi_j(2)\left(\frac{1}{r_{12}}\right)[\chi_a(1)\chi_b(2) - \chi_b(1)\chi_a(2)]}{\varepsilon_a + \varepsilon_b - \varepsilon_i - \varepsilon_j} \qquad 1\text{-}31$$

These integrals will be non-zero only for double excitations according to the Brillouin theorem.

Third (MP3), and fourth (MP4) order Møller-Plesset calculations are frequently used in computational chemistry. A great advantage of the many-body perturbation theory is that it is size-consistent. However, a serious drawback is that it is not variational and can give energies that are lower than the true energy [7, 13-22].

1.2.2 Coupled Cluster (CC)

Another way to incorporate the (dynamic) electron correlation is with a numerical technique called Coupled Cluster [23-30]. Two important theorems, the linked cluster theorem and the connected cluster theorem, are the basis of the coupled cluster approach [23-30].

1.2.2.1 Wave function ansatz and cluster operator

The Coupled Cluster theory supposes that there is an appropriate cluster operator $\hat{T}$ such that an ansatz wave function can be defined as:

$$|\Psi\rangle = e^{\hat{T}}|\Psi_0\rangle \qquad 1\text{-}32$$

In the above, $|\Psi_0\rangle$ is an appropriate reference function of some sort and the cluster operator, which is exponentiated, is defined by:

$$\begin{aligned}\hat{T} &= \hat{T}_1 + \hat{T}_2 + \cdots \\ \hat{T}_1 &= \sum_i \sum_a t_i^a \hat{a}_i \hat{a}_a^+ \\ \hat{T}_2 &= \frac{1}{4}\sum_{i,j}\sum_{a,b} t_{ij}^{ab} \hat{a}_i \hat{a}_j \hat{a}_a^+ \hat{a}_b^+\end{aligned} \qquad 1\text{-}33$$

The operators $\hat{a}$ and $\hat{a}^+$ are the creation and annihilation operators, respectively, and *i, j* and *a, b* respectively stand for occupied and unoccupied orbitals. $\hat{T}_1$ and $\hat{T}_2$ are called the one-particle excitation operator and the two-particle excitation operator because they effectively convert the reference function into a linear combination of singly- and doubly-excited Slater determinants.

When one substitutes the ansatz wave function into the Schrödinger equation, one obtains:

$$\begin{aligned}\hat{H}e^{\hat{T}}|\Psi_0\rangle &= Ee^{\hat{T}}|\Psi_0\rangle \\ \hat{G}|\Psi_0\rangle &= e^{-\hat{T}}\hat{H}e^{\hat{T}}|\Psi_0\rangle = E|\Psi_0\rangle\end{aligned} \qquad 1\text{-}34$$

where $\hat{G} = e^{-\hat{T}}\hat{H}e^{\hat{T}}$ is a transformed operator. The ansatz preserves the eigenvalues of the original Hamiltonian. However, it transforms at the same time the original Hamiltonian operator into the new operator $\hat{G}$. The transformation process does *not* preserve the

hermitian nature of the original Hamiltonian but it can preserve the hermiticity of the system if one makes sure that the cluster operator is antihermitian. $\hat{T}^{+} = -\hat{T}$

From the Taylor series expansion, one can see that higher order states are excited due to the compounding effect of repeated applications of the cluster operator:

$$e^{\hat{T}} = 1 + \hat{T} + \frac{\hat{T}^2}{2!} + \cdots = \sum_{n=0}^{\infty} \frac{\hat{T}^n}{n!} \qquad 1\text{-}35$$

It can be seen from equation 1-35 that the effect of excitations decreases as the denominator gets larger. Also, since the reference state represents a system of electrons, the Taylor series for the cluster operator terminates at a finite length due to the physical interpretation and relevance of the system of interest (the number of excitations cannot exceed the number of electrons).

A number of minor modifications have been made to the original framework of the Coupled Cluster theory so that certain special cases of molecules and their energies can be computed. These modifications include:

1. Imposing the operator $e^{\hat{T}}$ to be unitary
2. Adding higher order terms to the cluster operator $\hat{T}$

The abbreviations for coupled cluster methods usually begin with the letters "CC" followed by S for single excitations, D for double excitations, T for triple excitations and Q for quadruple excitations. Bracketed terms indicate that the higher order terms are calculated based on perturbation theory.

1.2.2.2 Description of the theory

The method gives the exact non-relativistic solution to the Schrödinger equation if the cluster operators are included up to the n^{th} order where n is the highest excitation level in the $\hat{T}$ operator (single, double excitations and so forth). However, the computational effort of solving the equations grows steeply with the order of the cluster operator and the method is limited to the first few orders in practice.

For a coupled-cluster singles and doubles (CCSD) calculation, one solves the Coupled-Cluster equation using the operator $\hat{T} = \hat{T}_1 + \hat{T}_2$, which produces all Slater determinants which differ from the reference determinant by one or two spin-orbitals. This approach has the effect of describing coupled two-body electron correlation effects and orbital relaxation effects. Because the operator $\hat{T}$ is exponentiated in coupled-cluster theory, higher-order "disconnected" electron correlations are also accounted for in an approximate way. It is also usual to include an approximate perturbative correction accounting for three-body electron correlations in a popular method named CCSD(T). It includes the triple excitations at the fourth order and the singles at the fifth order. For ground electronic states near their equilibrium geometries, CCSD(T) is often considered a gold standard because it provides results very close to those of a full configuration interaction calculation.

The coupled cluster equations are usually derived using a diagrammatic technique, as was initiated by Feynman, and result in nonlinear equations which can be solved in an iterative fashion [23-30].

1.3 Density Functional Theory

Another method to tackle the correlation problem is to use the density functional theory (DFT), an alternative approach that gives approximate solutions to both exchange and

correlation energies [31-43]. It decreases the complexity by replacing the wave function, which depends on four variables (the three spatial variables and the spin) for each electron, with the electron density which depends only on the three cartesian spatial coordinates. Unlike the wave function, the density is also a physically observable quantity (for example, by X-ray diffraction) [31-43].

The density function, a fundamental variable in statistical mechanics and a positive function, determines the probability of finding any of the N electrons within the volume element dr_1 while the other (N – 1) electrons have arbitrary positions and spins in the state represented by Ψ. In other words, it is the number of electrons per unit volume at a given point in space.

$$\rho(r_1) = N \underbrace{\int \cdots \int}_{N-1} |\Psi(r_1, r_2, r_3, \cdots, r_N)|^2 dr_2 dr_3 \cdots dr_N \qquad 1\text{-}36$$

Electrons are indistinguishable and the probability of finding any electron at a given position is, therefore, just N times the probability for one particular electron. In the simplest model, the electrons are considered as particles forming a uniform electron gas in which the electron density is uniform and there is a neutralizing background positive charge. The electrons, uniformly distributed in space, do not interact with each other. This model allowed Thomas and Fermi to derive an expression for the kinetic energy by applying statistics.

$$T_{TF}[\rho(r)] = C_F \int \rho^{5/3}(r) dr$$
$$C_F = \frac{3}{10}(3\pi^2)^{2/3} \qquad 1\text{-}37$$

They were then able to obtain the energy of the system:

$$E_{TF}[\rho(r)] = \underbrace{C_F \int \rho^{5/3}(r)dr}_{\text{kinetic energy}} - \underbrace{Z\int \frac{\rho(r)}{r} dr}_{\text{electron-nuclear attraction}} + \underbrace{\frac{1}{2}\iint \frac{\rho(r_1)\rho(r_2)}{r_{12}} dr_1 dr_2}_{\text{Coulomb repulsion}} \qquad 1\text{-}38$$

This simple model, which require an iterative procedure to be performed within the framework of the variational principle, and some further developments like the Thomas-Fermi-Dirac model, did not give good results for atoms and is unable to represent bonding, and therefore molecules. However, it was a pioneering work which initiated the use of the density to obtain the properties of atoms and molecules [31-43].

1.3.1 The Hohenberg - Kohn Theorems

The cornerstone of the density functional theory was provided in 1964 by Hohenberg and Kohn when they showed that a unique mapping between the ground-state electron density and the external potential v_{ext} exists based on the variational principle. This is the first Hohenberg and Kohn theorem and justified, a posteriori, the Thomas-Fermi models and allowed further development. It implies that every observable of a stationary quantum mechanical system, including the energy, can in principle be calculated exactly from the ground-state density alone. In other words, all properties can be written as functionals of the ground-state density. The second theorem states that the ground-state density can, in principle, be calculated exactly using a variational method involving only the density.

These theorems, which originally applied only to the time-independent ground-state, have been extended to excited states and time-dependant potentials.

The expression of the energy given by the Hohenberg - Kohn theory is then given by a sum of the kinetic and electron repulsion energies.

$$E_v[\rho] = \int \rho(r)v(r)d(r) + F_{HK}[\rho] \qquad 1\text{-}39$$

Unfortunately, no expression was given for F_{HK}. Furthermore, no method to calculate the energy or density from equation 1-39 was equally proposed.

1.3.2 The Kohn-Sham Approach

The next major advance in density functional theory came in 1965 when Kohn and Sham proposed a practical method to apply DFT to molecular systems. They developed a new and more accurate form of the kinetic energy functional.

The exact kinetic energy functional is given as a function of Kohn-Sham orbitals and their occupation numbers. It is very painful to calculate for a real chemical system due to the number of orbitals involved.

$$T = \sum_{i}^{N} n_i \langle \psi_i | -\frac{1}{2}\nabla^2 | \psi_i \rangle \qquad 1\text{-}40$$

Kohn and Sham simplified this expression by considering a system of non-interacting electrons with the same density as the interacting system (this is achieved by adjusting the external potential). The exact kinetic energy can be rewritten as a sum of two contributions: the energy from the reference system of non-interacting electrons $T_s[\rho]$ and the correction coming from the interaction between the electrons $(T[\rho]-T_s[\rho])$.

The exact density for the non-interacting gas is known and defined as:

$$\rho(r) = \sum_{i}^{N}\sum_{s} |\psi_i(r,s)|^2 \qquad 1\text{-}41$$

The kinetic energy of the non-interacting gas can then be written in terms of the wave function for the non-interacting system:

$$T_s[\rho] = \sum_{i}^{N} \langle \psi_i | -\frac{1}{2}\nabla^2 | \psi_i \rangle \qquad 1\text{-}42$$

The total Kohn-Sham (KS) energy can therefore be expressed using the non-interacting system as a reference state:

$$E_{KS}[\rho] = \underbrace{\int \rho(r)v(r)dr}_{\text{interaction of the density with the potential v(r)}} + \underbrace{T_s[\rho]}_{\text{kinetic energy of the reference system}} + \underbrace{J[\rho]}_{\text{Coulomb repulsion energy of the electrons}}$$

$$+ \underbrace{(T[\rho]-T_s[\rho])}_{\text{correction to the kinetic energy due to the interaction between electrons}} + \underbrace{(V_{ee}[\rho]-J[\rho])}_{\text{non-classical electron-electron contribution}} \qquad 1\text{-}43$$

The Kohn-Sham orbital equation, analogous to the HF equations, can be obtained by introducing the KS one-electron Hamiltonian which is a hermitian operator with respect to the electron density:

$$\hat{h}_{KS} = -\frac{1}{2}\nabla^2 + v(r) + \int \frac{\rho(r')}{|r-r'|} + \frac{\delta E_{XC}[\rho(r)]}{\delta\rho(r)} \qquad 1\text{-}44$$

where E_{XC} is the exchange correlation energy.

It is now necessary to find the set of orbitals ψ which give the density which minimizes the energy functional $E_{KS}[\rho]$ subject to the constraint that the orbitals have to be orthonormal and that the total density gives the total number of electrons. This minimization can be achieved using Lagrange multipliers:

$$\delta E_{KS}[\rho] - \lambda \sum_i^N \sum_j^N \varepsilon_{ij}\psi_i^*(r)\psi_j(r)dr = 0 \qquad 1\text{-}45$$

Solving equation 1-45 generates the set of one-electron Kohn-Sham equations:

$$\hat{h}_{KS}\psi_i = \sum_j^N \varepsilon_{ij}\psi_i \qquad 1\text{-}46$$

The canonical KS equation can be obtained from equation 1-46, on account of the Hamiltonian being a hermitian operator, by a diagonalization of ε_{ij}

$$\hat{h}_{KS}\psi_i = \varepsilon_i\psi_i \qquad 1\text{-}47$$

From this expression, the same approach that was used in Roothaan-HF can be applied. Therefore, the orbitals are expanded in a finite set of basis functions

$$\psi_i(r) = \sum_{\mu=1}^{K} C_{\mu i}\varphi_\mu(r) \qquad 1\text{-}48$$

and a matrix eigenvalue equation is obtained that can be solved iteratively:

$$H_{KS}C = SC\varepsilon \qquad 1\text{-}49$$

The SCF-KS calculation involves the following steps:

- start with a density (for the first iteration, it is usually the superposition of atomic densities)
- establish a grid for the charge density and exchange-correlation potential
  In order to limit expense of numerical integration during the SCF cycle, auxiliary functions fitted to charge density and exchange correlation potential are frequently used. This allows for much faster integral evaluation. These auxiliary fitting functions are usually uncontracted gaussians for which the integrals required for KS matrix can be calculated analytically. Different auxiliary sets are used for fitting charge density and exchange-correlation potential.
- compute the KS matrix elements and overlap matrix elements
- solve the equation for the expansion coefficients to obtain KS orbitals

- calculate the new density $\rho = \sum_{occupied} |\varphi(r)|^2$
- either the density or energy changed significantly, restart from the first step with the latest density, or, if the SCF cycle has converged, calculate the properties

1.3.3 Approximate Exchange-Correlation Functionals

Most of the contributions to the energy can be treated exactly in the KS formalism. The kinetic energy correction and the non-classical contributions are treated in the exchange-correlation functional (XC). In principle, the exact ground state properties can be obtained from the solution of the KS equations. Unfortunately we do not know the exact form of the energy functional $E_{XC}[\rho]$. Therefore, it is necessary to use approximations, as accurate as possible, to parts of the functional dealing with the correction to the kinetic energy, the exchange energy, and the correlation energy of the system. All approximations start from an ideal model, the homogeneous electron gas system, where electrons move in a uniformly distributed positive charge background. In this model, the electron density is a constant everywhere, which means that the local density can represent the electron density of the whole system.

1.3.3.1 Local Density and Local Spin Density Approximation (LDA and LSDA)

The simplest approximation, and the first developed, was the local density approximation (LDA). The LDA methods use the uniform-electron-gas approximation for the exchange

similarly to the TFD method. The correlation energy is assumed to be locally approximated by the uniform-electron-gas model.

The exchange-correlation energy in the LDA approximation is given by:

$$E_{XC}^{LDA}[\rho] = \int \rho(r)\varepsilon_{XC}(\rho)d(r) \qquad 1\text{-}50$$

where

$$\varepsilon_{XC}(\rho) = \varepsilon_X(\rho) + \varepsilon_C(\rho) \qquad 1\text{-}51$$

The exchange term $\varepsilon_X(\rho)$ is the Dirac term for the exchange energy in the framework of the uniform-electron-gas model. There is no explicit form of the correlation functional derived by mathematics. Vosko, Wilk and Nusair (VWN) [44] gave an approximate expression for $\varepsilon_C(\rho)$ using a Padé approximation to interpolate the results from quantum Monte-Carlo simulations carried out by Ceperly and Alder [45]. Other parameter values exist (standard self-interaction correction of Perdew and Zunger [46]).

LDA provides reasonable results for systems close to the ideal uniform-electron-gas model (i.e., the density varies slowly). For atoms and molecules, where the density can fluctuate rapidly, the results can sometimes be poor.

In a precursor to these approximate methods, Slater formulated, in 1951, a method called the Xα method which was an approximate solution to the HF equations. In this method, the non local Fock operator or HF exchange is approximated by a local operator:

$$\hat{F}_{X\alpha} = -\frac{1}{2}\nabla^2 + v(r) + \int \frac{\rho(r')}{|r-r'|} + v_{X\alpha}(r) \qquad 1\text{-}52$$

where $v_{X\alpha}(r) = -\frac{3}{2}\alpha\left\{\frac{3}{\pi}\rho(r)\right\}^{1/3}$. This expression for $v_{X\alpha}(r)$ is the Dirac exchange if α = 2/3 in the case of a homogeneous electron gas. The parameter α, was empirically optimized for each atom of the periodic table and its value is between 0.7-0.8 for most atoms.

A further evolution of the present approximation, the local spin density approximation (LSDA), will replace the electron density by the spin density, consequently giving more flexibility to the functional.

While the LDA uses the total electron density, $\rho(r) = \rho^{\alpha}(r) + \rho^{\beta}(r)$, the LSDA is based on the spin-polarized uniform electron gas that differentiate the spin-up and spin-down densities. This approximation becomes particularly significant when magnetic fields are present and is also required for systems with unpaired electrons. The electronic energy functional in the absence of magnetic field becomes:

$$E_{electron}^{LSDA}[\rho] = T_S[\rho^{\alpha},\rho^{\beta}] + J[\rho] + E_{XC}[\rho^{\alpha},\rho^{\beta}] \qquad 1\text{-}53$$

Hence, applying the variation principle to minimize the energy functional produces the two following sets of equations, one for each spin:

$$\hat{h}_{eff}^{\sigma}\varphi_{i\sigma}(r) = \varepsilon_i^{\sigma}\varphi_i(r) \text{ where } \sigma = \alpha,\beta$$
$$\hat{h}_{eff}^{\sigma} = -\frac{1}{2}\nabla^2 + v(r) + \int\frac{\rho(r')}{|r-r'|}dr' + \frac{\delta E_{XC}[\rho^{\alpha},\rho^{\beta}]}{\delta\rho^{\sigma}(r)} \qquad 1\text{-}54$$

The exchange-correlation functional can, once again, be divided into two parts, one for the exchange and one for the correlation. One of the most frequent and simple forms used for the exchange is the one derived by Slater for the spin polarized cases, which differ from Dirac's exchange only by the value of the parameter α :

$$E_X^{LSDA}[\rho^\alpha,\rho^\beta]=2^{1/3}\left(\frac{3}{4}\right)\left(\frac{3}{2}\right)\alpha\left[\frac{3}{\pi}\right]^{1/3}\int\left[(\rho^\alpha)^{4/3}+(\rho^\beta)^{4/3}\right]dr \qquad 1\text{-}55$$

The correlation energy functional is not as simple to express because the interactions between the spin-up and spin-down electrons do not allow isolating each component in the density. Nevertheless, the correlation can be defined from the polarization:

$$\varsigma=\frac{(\rho^\alpha-\rho^\beta)}{\rho} \qquad 1\text{-}56$$

and therefore the correlation energy becomes:

$$E_C^{LSDA}[\rho^\alpha,\rho^\beta]=\int\rho\varepsilon_C(r_s,\varsigma)dr \qquad 1\text{-}57$$

where the Wigner-Seitz radius r_S is related to the density as follows: $r_s=\left(\frac{3\pi}{4\rho}\right)^{1/3}$

and $\varepsilon_C(r_s,\varsigma)$ is the correlation energy per electron, which unfortunately does not have any exact form and has to be approximated. The popular approximation by Vosko, Wilk and Nusair is often used.

Despite the approximation of the uniform electron gas model, the LSDA gives fairly good results (comparable to, or even better than, HF) for equilibrium structures and vibrational frequencies of covalently coordinated molecules. This success of LSDA seems to originate in the fact that the exchange-correlation hole of the uniform electron gas satisfies most of the important properties established for the exact exchange-correlation hole. The spherically averaged LSDA hole is a good approximation to the exact hole in the bonding region, where the exact hole becomes more symmetric with respect to the reference electron than in the separated atoms. LSDA, however, does result in over-binding which makes molecules over-stabilized compared to the separated atoms. Furthermore, it cannot treat long-

range interactions such as van der Waals interactions and it does very poorly for hydrogen bonded systems.

1.3.3.2 Generalized Gradient Approximation (GGA)

The LSDA exchange functional is local as well as the correlation but the first contribution is larger. Therefore, it seems that the main problem of the LSDA lies in the exchange term of the exchange-correlation functional. Introducing a gradient correction to consider the inhomogeneity of the electron density is the general idea behind the GGA methods. The first functional including a gradient correction was derived from the Thomas-Fermi-Dirac model. Von Weizsacker added a component of the inhomogeneous electron distribution to the initial model by using the gradient of the density. In that case, the kinetic energy functional of Thomas and Fermi is rewritten as follows:

$$T_W[\rho(r)] = \frac{1}{8}\frac{\hbar^2}{m}\int\frac{|\nabla\rho(r)|^2}{\rho(r)}dr \qquad 1\text{-}58$$
$$T_{TFDW}[\rho(r)] = T_{TF}[\rho(r)] + \lambda T_W[\rho(r)]$$

This approach allows a description of binding but the strengths of the bonds are not accurate and the iterative approach that gives the density must be done numerically.

The GGA exchange-correlation functional can generally be written as follows:

$$E_{XC}^{GGA}[\rho^\alpha,\rho^\beta] = \int\varepsilon_{XC}(\rho^\alpha,\rho^\beta,\nabla\rho^\alpha,\nabla\rho^\beta)dr = E_X^{GGA}[\rho] + E_C^{GGA}[\rho^\alpha,\rho^\beta] \qquad 1\text{-}59$$

The GGA exchange energy functional takes the following general form:

$$E_X^{GGA}[\rho] = -\frac{3}{4}\left(\frac{3}{\pi}\right)^{1/3}\int\rho^{4/3}f(s)dr \qquad 1\text{-}60$$

where the LSDA is obtained for $f(s)=1$

Several forms of this gradient-corrected exchange functional have been proposed and one of the most popular, given by Becke [47, 48], is known as B88. In this functional derived from the LSDA, first order gradient corrections were added in the density in order to mimic some non-local behavior.

$$E_X^{B88}[\rho]=E_X^{LDA}[\rho]-\beta\sum_\sigma \int \rho_\sigma^{4/3}(r) f(x_\sigma)dr \qquad 1\text{-}61$$

where x_σ is the dimensionless reduced density gradient for the spin considered and is in fact a local inhomogeneity parameter which implies large values for large gradients and in regions of small densities (exponential tails far from the nuclei), and small values of x_σ for small gradients (bonding regions) and regions of large densities:

$$x_\sigma(r)=\frac{|\nabla\rho_\sigma(r)|}{\rho_\sigma^{4/3}(r)} \qquad 1\text{-}62$$

There are two different classes of function f for the GGA functionals. The first one is based on Becke's GGA exchange functional B88 where:

$$f(x_\sigma)=\frac{x_\sigma^2}{1+6\beta\, x_\sigma \sinh^{-1}(x_\sigma)} \qquad 1\text{-}63$$

This reproduces the proper asymptotic behavior for the exchange energy density. The parameter β was fitted on the exact atomic HF exchange energy of noble gas atoms.
Perdew's exchange functional used in the popular Perdew-Wang 91 (PW91) [49] functional has the same general form.

The second class of GGA exchange functionals, including B86 and PBE, uses a rational function of the reduced density gradient. A slightly different approach that still belong to the same class is given by Perdew who used a second-order expansion with a cut-off radius to

impose conditions to the exchange hole function and further simplification led to the Perdew-Wang 86 (PW86) exchange functional which is parameter free.

Gradient corrections can also be added to the correlation energy functional although they have more complicated mathematical forms and no physical significance. A very popular correlation functional was derived by Lee, Yang, and Parr and therefore is called LYP [50]. It involves a second-order gradient expansion of the density and was not based on the uniform electron gas:

$$E_C^{LYP}[\rho(r)] = -a\int \frac{\gamma(r)}{1+d\rho^{-1/3}(r)}\left[\rho(r) + 2b\rho^{-5/3}(r)f(\rho(r))e^{-c\rho^{-1/3}(r)}\right]dr \qquad 1\text{-}64$$

where:

$$f(\rho(r)) = 2^{2/3}C_F\left(\rho^{\alpha}(r)\right)^{8/3} + 2^{2/3}C_F\left(\rho^{\beta}(r)\right)^{8/3} - \rho(r)t_W(r) +$$
$$+\left(\frac{1}{9}\right)\left(\rho^{\alpha}(r)t_W{}^{\alpha}(r) + \rho^{\beta}(r)t_W{}^{\beta}(r)\right) + +\left(\frac{1}{18}\right)\left(\rho^{\alpha}(r)\nabla^2\rho^{\alpha}(r) + \rho^{\beta}(r)\nabla^2\rho^{\beta}(r)\right) \qquad 1\text{-}65$$
$$t_W(r) = \frac{1}{8}\left(\frac{|\nabla\rho(r)|^2}{\rho(r)} - \nabla^2\rho(r)\right)$$

A fitting procedure, using only the HF orbital of a helium atom, was used to obtain the coefficients a, b, c, and d.

Any exchange functional could, in principle, be combined with any of the correlation functionals, but only a few combinations are really used. The GGA functionals give better results particularly for hydrogen bonded systems and for thermochemistry than the LSDA. However, there are obstacles that are not entirely avoided by the GGA, starting with the fact that since the LDA exchange-correlation potential does not have the right asymptotic behavior at long distance, adding the gradient correction does not lead to significant improvement.

1.3.3.3 Hybrid Functionals

Even if the GGA improves the accuracy over the LSDA, it does not provide the exact exchange. The error in the exchange can be further reduced by introducing more terms such as the kinetic energy density (meta-GGA functionals) or the Laplacian of the density. However, an error in the exchange-correlation functional will always remain.

Becke [51] proposed an idea to tackle this problem by mixing the "exact" Hartree-Fock exchange energy (where the Hartree-Fock orbitals are replaced by the Kohn-Sham orbitals) with a traditional GGA exchange-correlation functional. An exchange term is added, which is obtained through the concept of the adiabatic connection, which connects a non interacting system to a fully interacting system:

$$E_{XC}[\rho] = \int_0^1 U_{XC}^{\lambda}[\rho] d\lambda \qquad 1\text{-}66$$

At $\lambda = 1$, the LSDA or GGA is used. At $\lambda = 0$, the non-interacting limit, the exchange-correlation energy becomes the exact KS exchange energy without dynamic correlation. The connection between the non interacting and the fully interacting systems is reached by varying λ. After a first crude attempt, using half exchange and half correlation for the fully interacting system, Becke introduced the new B3 hybrid functional [52]:

$$E_{XC}[\rho] = E_{XC}^{LSDA}[\rho] + a_0\left(E_X^{exact}[\rho] - E_X^{LSDA}[\rho]\right) + a_X \Delta E_X^{B88}[\rho] + a_C \Delta E_C[\rho] \qquad 1\text{-}67$$

The three a parameters were determined by a linear least-squares fit on an experimental reference data set. The first parameter *a* represents the correction to the LSDA (or GGA) exchange energy near the limit $\lambda = 0$. ΔE's are the corrections to the LSDA brought by the GGA.

The most popular hybrid functional, B3LYP, uses the LYP correlation functional in the equation above. In general, B3LYP gives better results than another hybrid functional, called

B3PW91 which uses PW91 for the correlation term, or other pure GGA functionals, particularly for organic molecules. Hybrid methods also represent a significant improvement over GGA and LSDA functionals for transition metal compounds and systems including hydrogen bonds [53] since they provide better asymptotic behavior for the exchange functionals [31-43].

Chapter 2
Water Ice

Water plays a crucial role in many biological, environmental and chemical systems and although it is the most abundant chemical species on Earth, it is not a simple one. Despite its great importance and the extensive studies carried out to determine its structure and chemistry, the structure and chemistry of liquid water are not fully understood. Ice, however, is a well-characterized solid with many interesting features and properties. Besides its environmental importance, ice is unique because of the interesting phenomena contained within its structure. The crystal structure of ice is very unusual because, while the molecules lie on a regular crystal lattice (oxygen atoms), there can be disorder in their orientations. This property leads to many interesting characteristics in electrical polarization and conductivity. Ice plays an important role in everyday life, in its well known phase I_h. However, ice actually has many other crystalline phases which exist at various temperatures and pressures.

2.1 The water molecule

The water molecule is v-shaped, consisting of two hydrogen atoms bonded to one oxygen atom [54-57]. The O-H bond length in the gas phase water molecule is 0.957 Å and the H-O-H angle is 104.5°, forming a system with a large intramolecular dipole moment of 1.855 D (this value is the experimental gas phase value) [54-57].

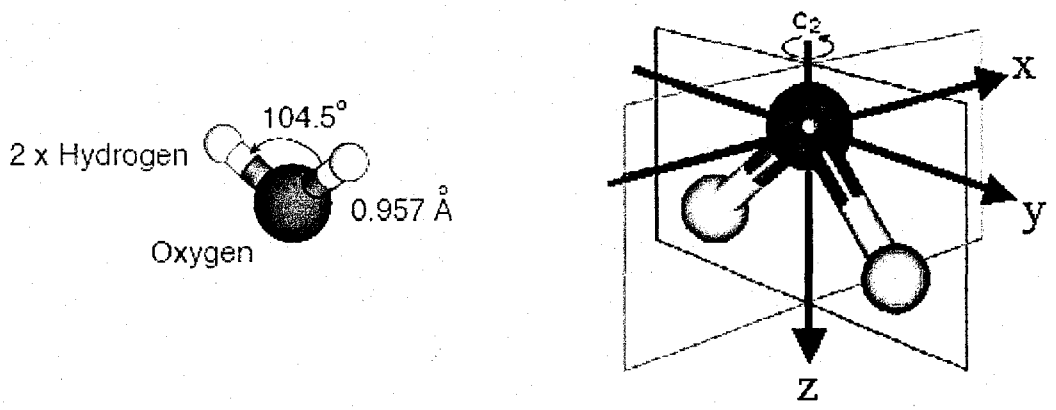

Figure 2-1 Geometry of a water molecule [58].

The molecular orbital diagram is as follows and the lowest energy structure is $(1a_1)^2(2a_1)^2(1b_2)^2(3a_1)^2(1b_1)^2$:

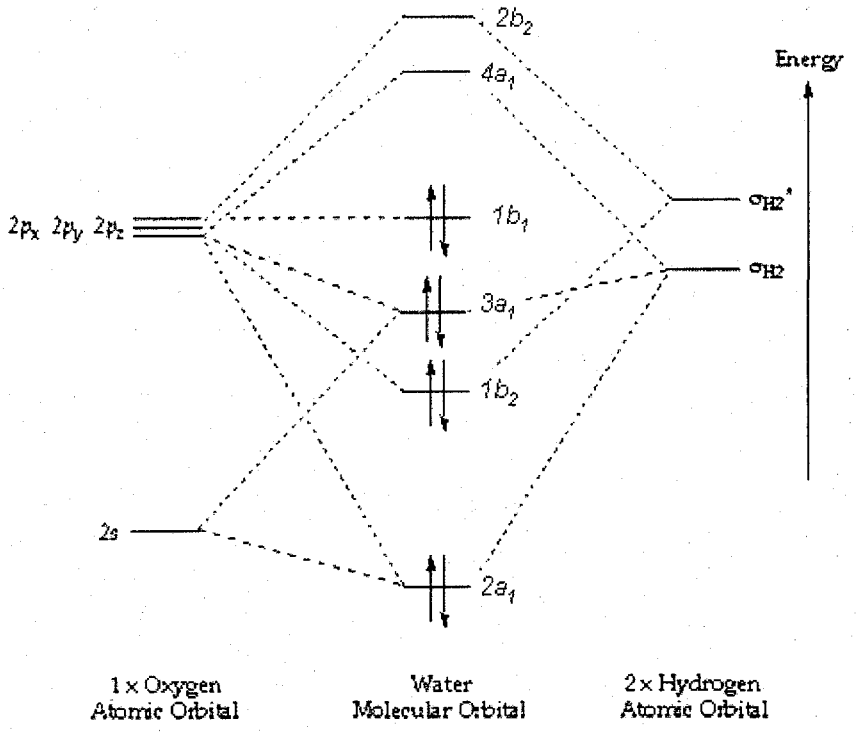

Figure 2-2 Molecular orbital diagram of the water molecule.

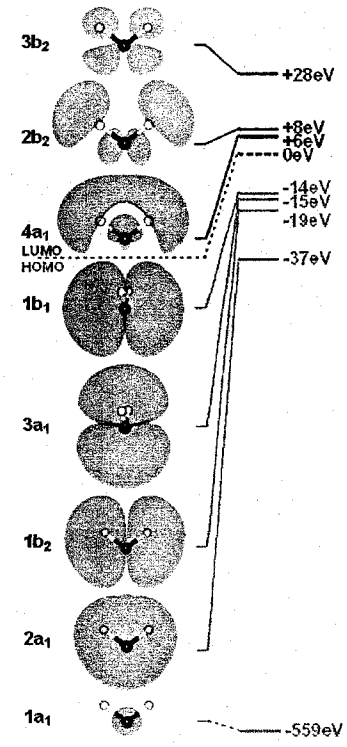

Symmetry properties and Orbital energies for the water molecule					
	Symmetry Behavior Under			Symmetry Classification	Orbital Energy (au)
Atomic Orbitals on Oxygen	C_2	σ_{xz}	σ_{yz}		
1s	+1	+1	+1	a_1	-20.669
2s	+1	+1	+1	a_1	-1.244
$2p_x$	-1	+1	-1	b_1	
$2p_y$	-1	-1	+1	b_2	-0.632
$2p_z$	+1	+1	+1	a_1	
Atomic Orbitals on Hydrogen					
$(1s_1+1s_2)$	+1	+1	+1	a_1	-0.500
$(1s_1-1s_2)$	-1	-1	+1	b_2	

Molecular Orbital Energies for H2O (au)				
$1a_1$	$2a_1$	$1b_2$	$3a_1$	$1b_1$
-20.565	-1.339	-0.728	-0.595	-0.521

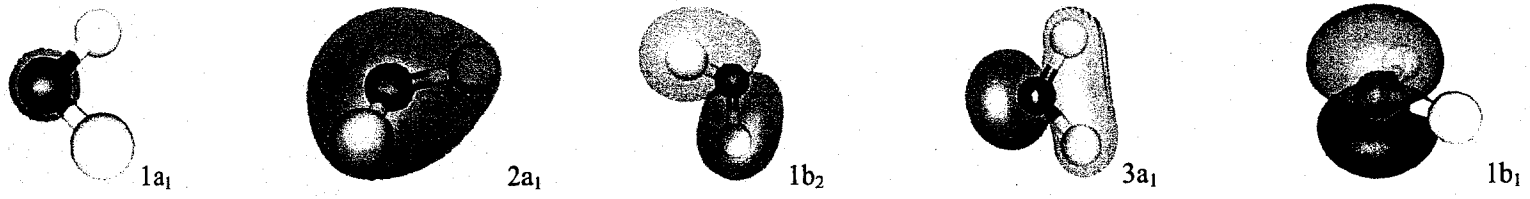

Figure 2-3 Molecular Orbitals of the water molecule. Energies calculated at the RHF/6-31G** level. Orbitals are given in the yz plane (x-axis downwards) except $1b_1$ and $3a_1$ which are in the xz plane (y-axis upwards) [58].

The lowest energy orbitals $1a_1$ and $2a_1$ primarily come from the 1s and 2s orbitals of the oxygen atom, respectively, and therefore are approximately spherical. The $1b_2$, $3a_1$ and $1b_1$ orbitals are orthogonal around the oxygen atom. The $1b_1$ orbital is predominantly the $2p_z$ orbital of the oxygen atom, without any contribution from the 1s hydrogen orbital. It essentially is a lone pair. The orbitals $2a_1$, $1b_2$ and $3a_1$ contribute to the O-H bond. The two lowest unoccupied orbitals $4a_1$ and $2b_2$ are O-H antibonding and become partially occupied when hydrogen bonds are formed. The $1b_2$ and $3a_1$ orbitals participate largely in donation of hydrogen bonds, with the largest contributor of the two being the $3a_1$ orbital. Comparison of the single water molecule to water or ice is expected to show that these orbitals undergo an appreciable change when the environment in which they are placed changes. Therefore, one would expect that the orbitals of bulk water and ice look quite different than those for the single water molecule [54-57].

2.2 Structures: ices and liquid water

Liquid water molecules are associated through a hydrogen bonding network [59], formed as a result of internal polarization of covalent bonds [60]. The hydrogen bond is much weaker than internal covalent bonds, but strong enough that well-defined structures could form in liquid water. Those strongly polar hydrogen bonds are responsible for a set of unusual physical and chemical properties [60].

- decreased volume during melting
- maximum density at 4°C
- isothermic compressibility minimum at 46°C, i.e. in the ambient liquid range
- numerous crystalline polymorphs
- high dielectric constant
- anomalously high melting, boiling, and critical temperatures for a low-molecular weight substance that is neither ionic nor metallic
- increasing liquid fluidity with increasing pressure
- high-mobility transport for H^+ and OH^- ions

The origin of these anomalies is the nature of the hydrogen bond, a specific attraction that exists between hydrogen atoms and electronegative atoms when the hydrogen atom is chemically bonded directly to another electronegative atom. The strength of a hydrogen bond (4-15 kcal/mol) is ten times larger than for van der Waals interactions but an order of magnitude less than for covalent chemical bonds. It can also be found between molecules like hydrogen fluoride (HF) and ammonia (NH_3).

As a result of its shape, a water molecule can accommodate up to four hydrogen bonds and this network can therefore extend in all three directions. This hydrogen bond network, which exhibits flexibility as well as strength, is illustrated by the large amount of crystalline forms observed. The phase diagram of water/ice is a very complex one and several amorphous phases have been identified that are not even presented in the following diagram [59].

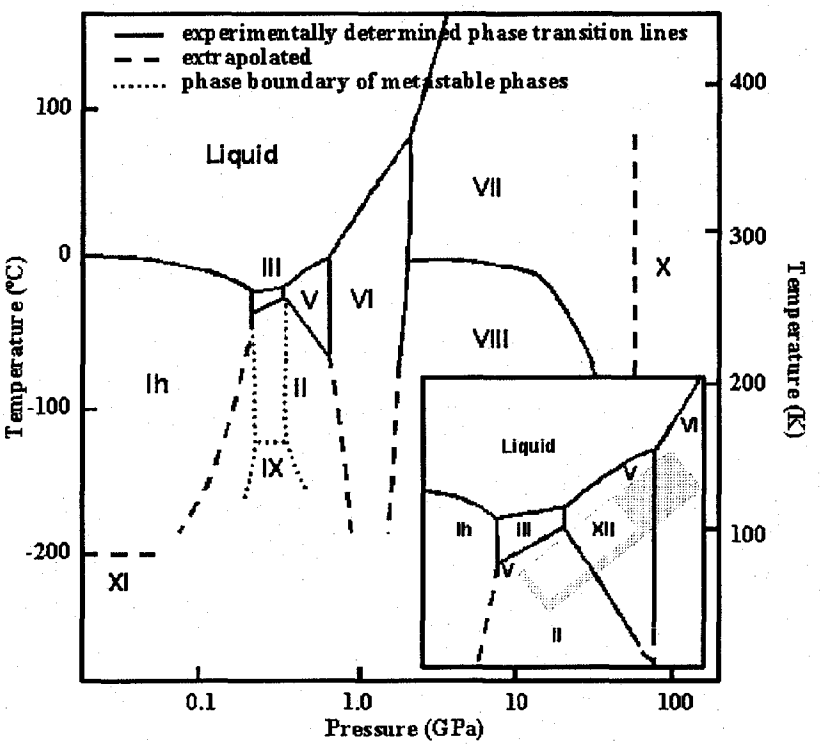

Figure 2-4 Phase diagram of water. The roman numerals indicate different crystalline polymorphs [58].

Ice is a perfect model to understand hydrogen bonding in water. For the ordinary ice I_h, every oxygen atom is at the center of a tetrahedron formed by four oxygen atoms each about 2.75 Å away. The angle between the oxygen atoms is of 109.5°. Every water molecule is hydrogen-bonded to its four nearest neighbors. Its O-H bonds are directed towards lone pairs of electrons on two of its neighbors resulting in two O-H···O hydrogen bonds. In turn each of its lone-pairs is directed towards an O-H bond of one of the other neighbors forming two O···H-O hydrogen bonds. Bernal and Fowler [61] gave a first insight into the possible arrangements of hydrogen atoms in ice I with their "ice rules" where only one hydrogen atom is present for each O-O bisectrix. The positions of the oxygen atoms in the lattice are fixed but the flexibility of the network comes from the randomly distributed hydrogen atoms which create the proton disordered ices. Only four of the thirteen structures in the phase diagram are proton-ordered ices: ices II, VIII, IX, and XI. Depending on the pressure, some deviations, like the bending of the hydrogen bonds, can be observed at moderate pressures. However, the perfect four hydrogen bonded neighbors arrangement is mostly respected and the structures of bulk ice are now relatively well understood.

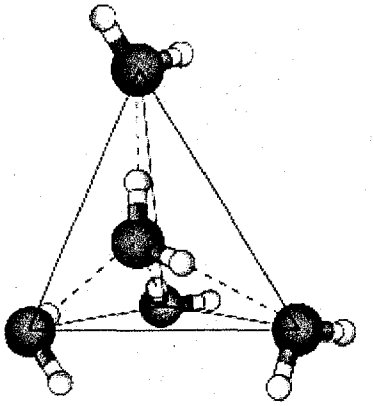

Figure 2-5 Hydrogen bond configuration in ice I_h includes four hydrogen bonds, two donating and two accepting. The hydrogen bonds follow the straight O-H - O line and the four water molecules form a tetrahedron around the central water molecule.

However, the space filling is very inefficient and the ice structure contains void spaces which become smaller and finally disappear upon melting and therefore cause the density to increase; this is the reason why liquid water is denser than ice.

The geometries of the structures studied in the present work will now be presented in greater detail. The four proton ordered ices as well as a model of liquid water will be introduced [60].

2.2.1 Ice II

Ice II (density of 1.17 g cm^{-3}) is formed by compressing ice I_h at 190 to 210 K and 300 MPa or by decompressing ice V at 240 K [62]. Heated ice II becomes ice III but the reverse process is difficult to accomplish. The unit cell is rhombohedral (space group R(-3)) but the structure can also be described as a larger hexagonal cell of 36 water molecules where two hexamers are hydrogen bonded, one chair-form and one almost flat. It contains hexagonal rings linked to one another and therefore ice II achieves a higher density than ice I_h.

In the crystal, all water molecules are hydrogen bonded to four others, two as donor and two as acceptor. The structure contains two crystallographic types of oxygen with equivalent weight. The H-O-H angle does not change much compared to that of the isolated molecule and therefore the hydrogen bonds are not straight. Some of the hydrogen bonds are further bent and much weaker than the hydrogen bonds in ice I_h. Ice II has no corresponding disordered phase, in contrast to the other proton ordered ices VIII, IX and XI. Ice II has triple points with ice I_h and ice III (-34.7°C, 212.9 MPa), ice III and ice V (-24.3°C, 344.3 MPa) and ice V and ice VI (estimated at -55°C, 620 MPa) [62].

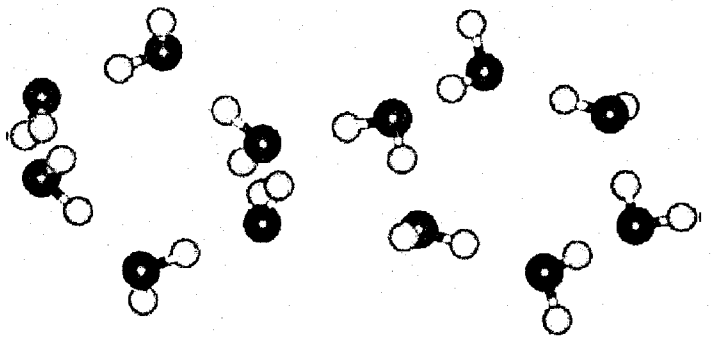

Figure 2-6 Ice II structure.

The geometry of the ice II structure used in the present work was taken from [63].

2.2.2 Ice VIII

Ice VIII is formed from ice VII by lowering its temperature to about 5°C. Ice VIII (density of about 1.5 g cm^{-3}) is the equivalent ordered structure of ice VII. That is, they have identical positions for the oxygen atoms but the protons in ice VII do not have fixed positions. However, the proton ordering causes a small distortion in the ice VII cubic lattice resulting in a tetragonal crystal structure ($I4_1/amd$). Ice VIII consists of two interpenetrating cubic ice lattices and forms a tetragonal crystal containing eight water molecules per unit cell. All the water molecules are hydrogen bonded to four others, two as donor and two as acceptor. All molecules experience identical molecular environments and, therefore, the structure contains only one crystallographic type of oxygen. Ice VIII has triple points with ice VI and ice VII (5°C, 2.1 GPa) and ice VII and ice X (100 K, 62 GPa).

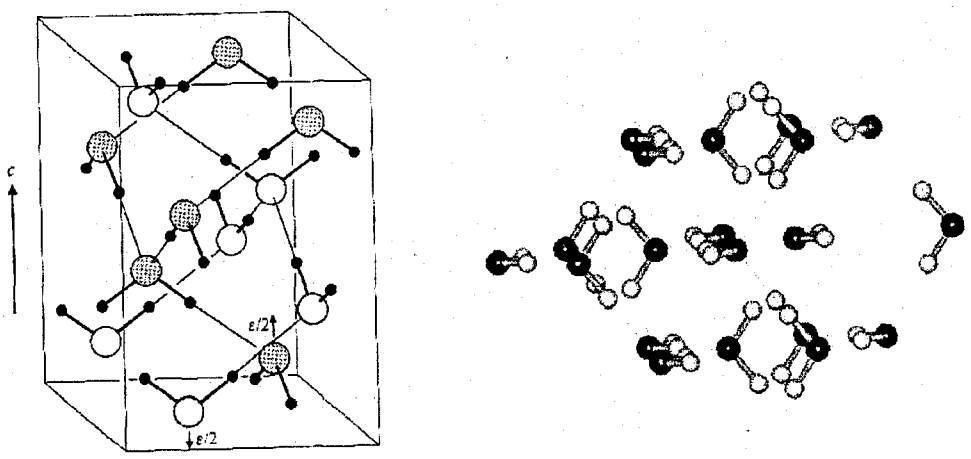

Figure 2-7 Ice VIII structure.

The geometry of the ice VIII structure used in the present work was taken from [64].

2.2.3 Ice IX

Ice IX (density of 1.16 g cm^{-3}) is the low temperature proton ordered structure of ice III and forms when ice III is rapidly cooled in liquid nitrogen (77 K to avoid the formation of ice II). The proton-ordering process that goes from ice III to ice IX has a first order transition near 126 K. The ordering of ice IX was determined by neutron diffraction to be antiferroelectric.

The unit cell is tetrahedral (space group P 4_1 2_1 2) and contains 12 water molecules. Its structure consists of tight right-handed four fold helices, containing two thirds of the water molecules, connected by the remaining water molecules. Therefore, the structure contains two crystallographic types of oxygen atoms, experiencing differing molecular environments, with non equivalent weight (1:2).

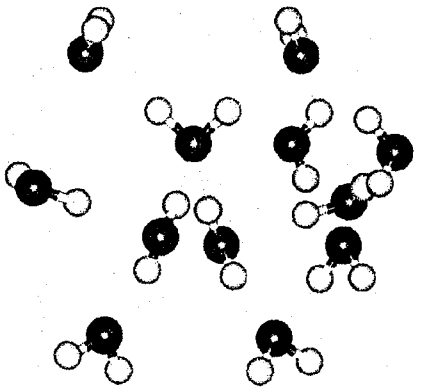

Figure 2-8 Ice IX structure.

The geometry of the ice IX structure used in the present work was taken from [65].

2.2.4 Ice XI

Ice XI is the low temperature proton ordered equilibrium structure of the hexagonal ice I_h [66-74]. It is prepared from dilute KOH solution kept just below 72 K but the transformation from hexagonal ice is very slow. The hydroxide ions create defects in the hexagonal ice and therefore enable the proton hopping process between the oxygen atoms (a process that is facilitated with increased pressure). The ions may also compensate for the large net dipole moment of the crystal lattice along the c-axis. The K^+ ions occupy interstitial sites in the hexagonal crystal. Ice XI is the thermodynamically favored form of ice at atmospheric pressure and low temperatures.

Ice XI forms orthorhombic crystals (space group C*mc*21). The structure contains two crystallographic types of oxygen atoms with equivalent weight. All bonds are parallel to the c-axis and oriented in the same direction and therefore ice XI is ferroelectric [66-73].

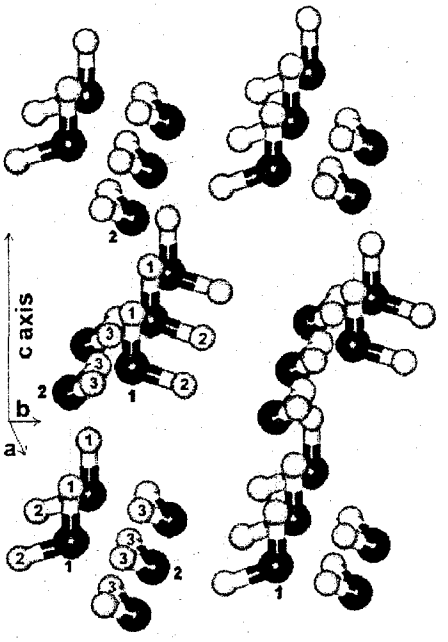

Figure 2-9 Ice XI structure.

The geometry of the ice IX structure used in the present work was taken from [75].

2.2.5 Liquid water

Contrary to ices, the structure of liquid water is a lot more difficult to elucidate. The hydrogen bonding patterns are random [60, 76]. The hydrogen bond length of water varies with temperature and pressure. The covalent bond lengths O-H do not vary much with temperature and pressure and therefore most of the changes must come from a reduction/increase in the hydrogen bond length. Hydrogen bond strength depends strongly on its length and it also depends on the temperature and pressure [77, 78].

Tetrahedral water structures are still found in liquid water but the hydrogen bond network can also be broken. For any water molecule, the four hydrogen bonds, the two hydrogen donors and the two hydrogen acceptors, can be located at any of the four sites around the oxygen. Water molecules surrounded by four hydrogen bonds tend to form clusters, for statistical and energetic reasons [79]. When a hydrogen bond forms between two water molecules, the redistribution of electrons changes the ability for further hydrogen bonding. The electron density of the water molecule donating the hydrogen atom increases in its lone pair region [80]. This will boost hydrogen bond acceptance. On the other hand, the electron density of the accepting water molecule decreases on its hydrogen atoms and remaining lone pair region [80]. This will boost further donation of hydrogen bonds. Accepting one hydrogen bond encourages the donation of another and discourages acceptance of another. Therefore, a water molecule with two hydrogen bonds where it acts as both donor and acceptor is stabilized relative to one where it is either the donor or acceptor of two [81, 82].

Hence, liquid water consists of a mixture of short, straight and strong hydrogen bonds and long, weak and bent hydrogen bonds with many intermediates between these two extreme cases. The water molecules in the liquid phase are all non-equivalent, differing in their molecular orbitals, their precise geometry and molecular vibrations due to their hydrogen bonding geometry which is influenced by the arrangement of the surrounding water molecules. Hydrogen bond lifetimes at ambient temperatures lie between 1 and 20 ps [83] whereas broken bond lifetimes are about 0.1 ps [84-86].

Many models have been developed but none has been able to account for all the properties of liquid water [87, 88]. A major problem is to understand the macroscopic properties of the liquid using statistical mechanics and to consider both the hydrogen bond strength and directionality remaining in the liquid phase with a relative large disorder. It is certain that the hydrogen bond network is a dynamical system that undergoes a constant evolution on the time scale of the breaking and reforming of the hydrogen bonds.

An assumption of most of these models is that we can simulate the structure of liquid water by using just two-body effects when many-body interactions have been proven to have

a considerable contribution [89]. So far, those models have failed to properly predict physical and molecular properties outside those used in their parameterization, and the agreement with experimental data is often poor. Generally, each model is developed to fit one particular physical structure or parameter. The more fitting parameters that are required by the model (some require over 50), the better the fit but it comes with an increase in the computational cost. Modeling may result in a picture of an average liquid water molecule that might be confusing as such average structures may not be relevant to liquid water and the purpose of this model is only to reproduce a specific property.

Some common models are presented in Figure 2-10. The model ***a***, also known as TIP3P [90], which only includes point charges on the oxygen and the two hydrogen atoms, will be used in chapter 5 to roughly determine the dipole moments of various water and ice structures.

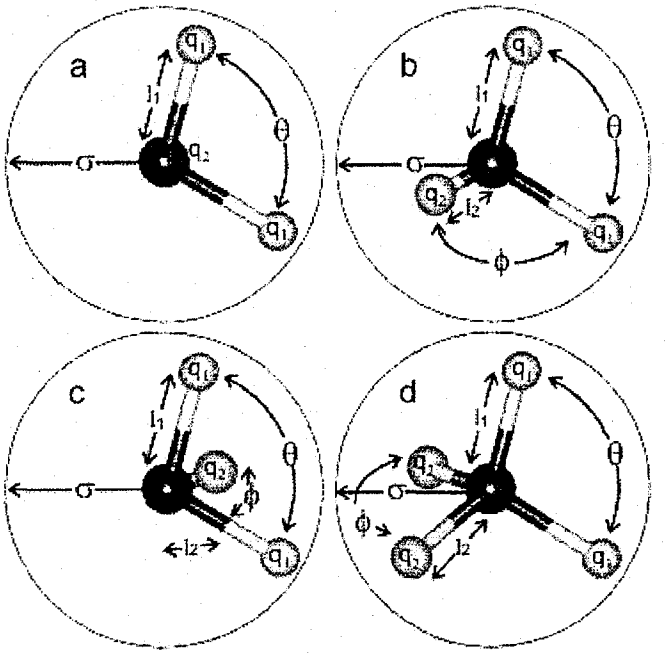

Figure 2-10 Water models. Models **a**, **b** and **c** are planar. Model **d** is almost tetrahedral [58].

The other models shown in Figure 2-10 can involve flexible bonding, induced dipoles or movable charges that may not coincide with the positions of the atoms. It will give a better fit, but at a significantly increased computational cost. Polarization strengthens the hydrogen bond and partially compensates for the lack of long range interactions and the dependence of these models on short ranged forces. Serious discrepancies concerning the first coordination shell of the hydrogen bond network have been noted between the molecular dynamics simulations using these models and X-ray absorption spectroscopy.

An arrangement with a strained geometry is very unlikely to last long. However, it may occur during the breakage, formation or partner switching of a hydrogen bond or arise from thermal effects or other molecular interactions in a long-lived hydrogen bond. A recent and controversial X-ray absorption spectroscopy study found that, at room temperature, 80% of the molecules of liquid water have one strong hydrogen bonded O-H group and one non, or only weakly, bonded O-H group at any instant. The remaining 20% molecules are tetrahedral and form four hydrogen bonds [91]. However, such instantaneous geometry is not presently the widely accepted time-averaged structure, which is basically tetrahedral with about 3.6 hydrogen bonds per water molecule [92-95]. On the other hand, Raman study supports the fully tetrahedral model. Instantaneous structures might not represent the time averaged structure. Hence, a QM/MM molecular dynamics simulation study showed that the time averaged hydrogen bond network gives about four hydrogen bonds per water molecule but the instantaneous value is significantly lower (about 2.8 hydrogen bonds per water molecule) [96].

Therefore, in order to understand the liquid structure, local and time averaged spatial arrangements of water molecules have to be defined. Averaged structures of a small region in the liquid were proposed as local persistent structures which are eventually interrupted by H_2O reorientation or translation. These structures correspond to a mean arrangement of the water molecules over a longer period than that required for intermolecular vibration but shorter than that required for diffusive motions of molecules. Several experiments (X-ray diffraction and neutron diffraction) found the averaged distribution of intermolecular distances and therefore the average number of neighbors (radial distribution functions) of a

water molecule in the liquid phase to be 4.7 neighbors at the mean distance of 2.75Å. Unfortunately, those methods do not provide any insight in the angular distribution.

The structure used for the water in the present work was obtained from a molecular dynamics simulation of liquid water at ambient temperature and pressure (300 K, 1 atm) using the SPC/E [97] intermolecular potential (Figure 2-10 **a**). The 18,70 Å cubic cell obtained from this simulation contains 216 water molecules.

Despite the fact that water can appear to be a very simple molecule, it remains very difficult to model realistically. A better understanding of the structure could help develop more accurate models [60, 76].

Chapter 3

Water-catalyzed reaction of formation of NH_2CH_2OH

3.1 Introduction

Over the past few decades, our knowledge of interstellar and cometary chemistry has dramatically increased [98-103]. The goal of astrochemistry, a field studying highly diluted interstellar space, is to understand how the most abundant elements found in this space, like H, C, N, and O, can combine to form molecules. The formation of such molecules can provide insight into the origin of the solar system and its evolution. Among the species found to date are small molecules containing the main functional groups from which larger molecules can form. Some of these larger molecules are also of biological interest. These molecules are detected in various environments like molecular clouds (10 to 20K in temperature and a density ranging from 10^3 to 10^5 H_2 molecules per cm^3) or environments closer to stars where the temperature is higher (a few hundreds Kelvin). The interstellar medium is composed mostly of gases (for more than 90%) and dust (diameter of a speck on the order of a micrometer) spread between stars. Some interstellar molecules detected to date include CO, CS, HCN, HNC, H_2S, SO_2, $HCONH_2$, $HC_{11}N$. In addition, more complex molecules like amino acids [104], are detected, though in trace amounts. However, this only represents a very small percentage of the total mass, but it exhibits a large variety since about 120 different molecules have been found in the interstellar clouds or in the "atmospheres" of comets. The presence of dust seems to play a major role as it protects the molecules against UV radiation that could destroy them and intervene in the reactivity of interstellar molecules. By releasing molecules trapped on the surface, the UV or cosmic radiation can act as a catalyst for reactions occurring at the surface of the dust grains. The study of these dust grains shows the existence of a layer of frozen gases comprised mostly of

water molecules, but also containing CO, CH_3OH, CO_2, NH_3, H_2, and H_2CO [105, 106]. These gases coat a nucleus formed by silicates and carbon compounds. When comets approach a nearby star, they start to release dusts and frozen gases under the effects of solar radiations and solar wind. This creates an envelope (spreading up to 10^5 km around the nucleus of the comet) of gases and dust and two trails of ions and dusts. The reactivity of the sublimate molecules is favored by a local temperature and molecular density higher than those found in the interstellar clouds. The omnipresence of ice [107] and the abundance of water molecules compared to other species imply that water molecules or ice has to be considered as an important factor in the reactivity of those interstellar molecules and is thought to play the role of a catalyst [108] in the reactions between species present in this environment.

Since there are obvious limitations on our ability to study such hard-to-access media, theoretical methods are indispensable for a thorough understanding of the chemical processes [109] occurring in such environments. We will focus on the formation of NH_2CH_2OH from two previously mentioned minor constituents of comets, NH_3 and H_2CO. Studying the formation of NH_2CH_2OH is a good example of how larger molecules can form from smaller molecules present in the cometary environment [110]. The reaction is studied in both the absence and presence of water molecules. Water is known to play the role of a catalyst in many reactions and, consequently, calculations in the presence of zero, one, two, and three water molecules are performed.

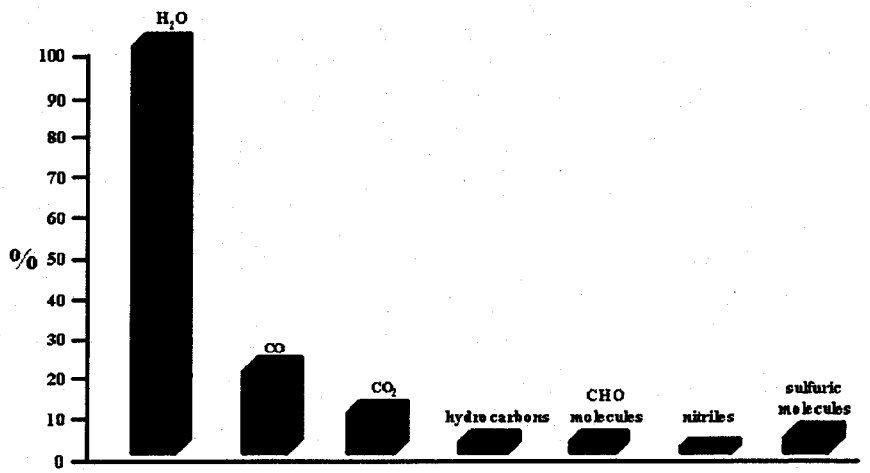

Figure 3-1 Example of a standard chemical composition of a comet.

3.2 Computational Method

The potential energy surface was explored at the MP2/6-311+G** and B3LYP/6-311+G** levels. A sufficiently large basis was required to properly describe the mechanism for the trihydrated complex. Use of a 6-31G** basis led to problems when trying to locate the MP2 transition state. Vibrational analyses were performed at the stationary points to characterize them as either local minima or transition states. CCSD(T)/6-311+G** single point energy calculations were then performed at each stationary point on the MP2 and B3LYP potential energy surfaces. Unless otherwise stated, the CCSD(T)/6-311+G**//MP2/6-311+G** and CCSD(T)/6-311+G**//B3LYP/6-311+G** energies reported in the following discussion include zero point energy corrections. As proposed by Scott and Radom [111], the MP2 frequencies were scaled by a factor of 0.9748 and the B3LYP frequencies were scaled by a factor of 0.9806. All calculations are performed with Gaussian 98 [112].

3.3 Results and Discussion

3.3.1 Non, mono, and dihydrated complexes

The reaction of ammonia and formaldehyde to produce NH_2CH_2OH, in the presence of zero, one, and two water molecules has previously been studied by Woon at a lower level of theory [113]. Rather than optimizing at the MP2/6-311+G** level, this prior work explored the MP2/6-31+G** potential energy surface. For single point calculations on this same system, Woon's previous work used the MP2/aug-cc-pVDZ and MP4/6-31+G** methods, but only when no water molecules were present. It should also be noted that these systems were first studied by Williams [114], albeit using the far less precise MP2/6-31G*//HF/3-21G approach. In the subsequent discussion on the non-, mono-, and dihydrated complexes, we will limit

the comparisons of our results to those of Woon [113]. The geometries as well as the total, zero point, activation, and reaction energies are provided in Tables 3-1 to 3-4 respectively. In the Figures depicting the structures of the reactive complex, transition states and final products, the energy of each structure is reported relative to the isolated molecules.

The formation of NH_2CH_2OH from H_2CO and NH_3 is proposed to occur via nucleophilic attack of the carbon atom in H_2CO by the lone pair of the nitrogen atom in NH_3. In a concerted approach, there is also a proton transfer step from NH_3 to H_2CO. In the absence of water, the proton is transferred directly from the nitrogen atom to the oxygen atom. However, in the presence of water, the transfer occurs via a chain of water molecules.

In the absence of water (Figure 3-2), our ZPE-corrected potential energy barrier is 36.8 kcal/mol at the CCSD(T)/6-311+G**//MP2/6-311+G** level. On the B3LYP potential energy surface, a nearly identical value, 36.4 kcal/mol, is found. Woon found barriers (not ZPE-corrected) of 31.0 and 35.5 kcal/mol with the MP2/aug-cc-pVDZ and MP4/6-31+G** methods, respectively, at the MP2/6-31+G** stationary points. Since the ZPE correction is of the order of +0.5 kcal/mol for this system, our results agree well with the previous work of Woon. Such a high activation energy most likely precludes the direct reaction of NH_3 and H_2CO within the interstellar medium. Water must therefore play an important role.

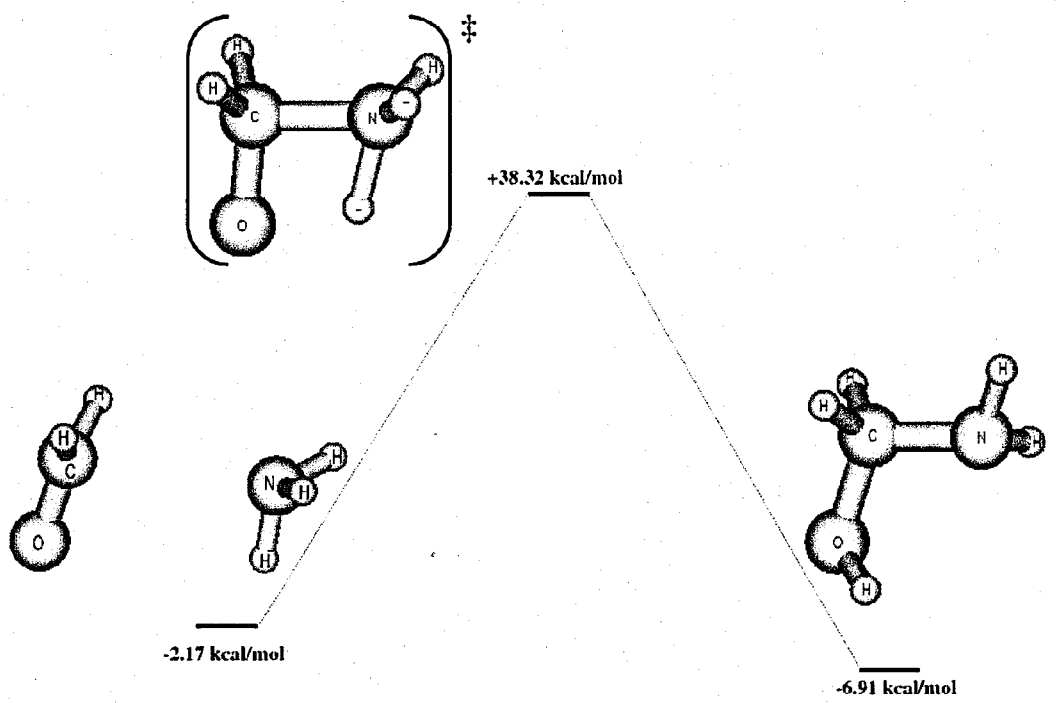

Figure 3-2 Energy profile for the reaction $NH_3 + H_2CO \rightarrow NH_2CH_2OH$ in the absence of water at the CCSD(T)/6-311+G**//MP2/6-311+G** level (zero-point corrected energies, in kcal/mol, relative to the isolated molecules are reported).

In the presence of a single water molecule (Figure 3-3), the proton is no longer directly transferred from the nitrogen atom in NH_3 to the oxygen atom in H_2CO. Rather, there is a concerted pair of proton transfers from NH_3 to H_2O and from said H_2O to H_2CO. This mechanism has a much lower activation energy than that seen in the absence of water. It is now 19.0 kcal/mol at the CCSD(T)/6-311+G**//MP2/6-311+G** level. On the B3LYP potential energy surface, it is 18.4 kcal/mol. Woon found a ZPE-corrected barrier of 16.0 kcal/mol (15.0 without the ZPE correction) at the MP2/6-31+G** level, the highest level of theory used in this work for this complex.

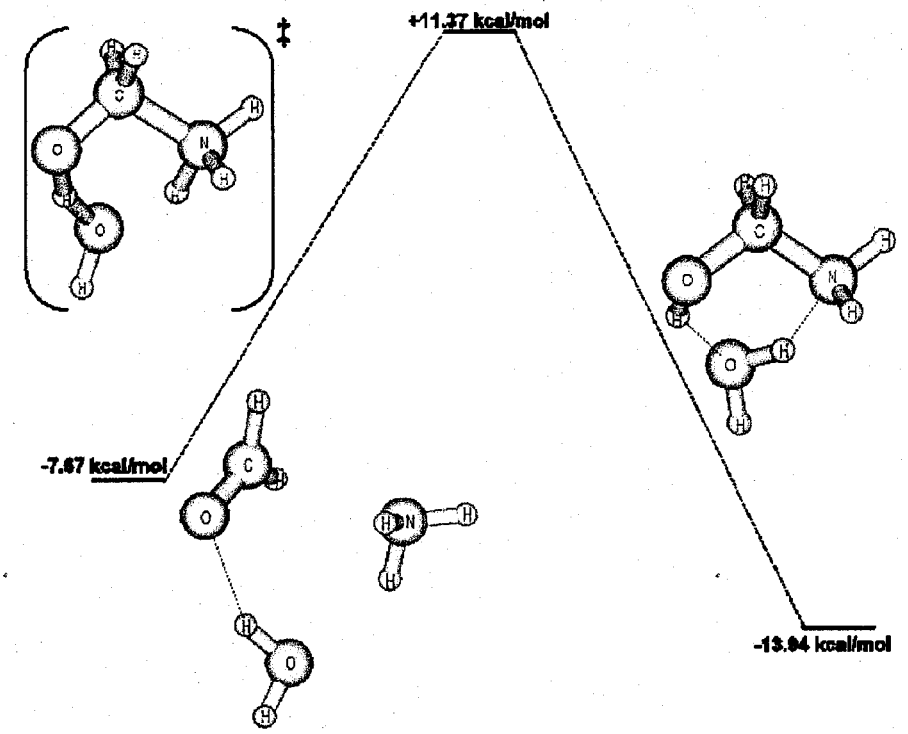

Figure 3-3 Energy profile for the reaction $NH_3 + H_2CO \rightarrow NH_2CH_2OH$ catalyzed by a single water molecule at the CCSD(T)/6-311+G**//MP2/6-311+G** level (zero-point corrected energies, in kcal/mol, relative to the isolated molecules are reported).

When a second water molecule is present (Figure 3-4), the mechanism becomes a concerted trio of proton transfers via the water molecules. The CCSD(T)/6-311+G**//MP2/6-311+G** activation energy for this reaction drops to 14.4 kcal/mol. On the B3LYP potential energy surface, the CCSD(T) result is slightly lower, at 13.3 kcal/mol. Woon found a lower activation energy, 9.3 kcal/mol, at the MP2/6-31+G** level. No ZPE correction was reported, but as the results in Table 3-3 indicate, the ZPE correction for the dihydrated complex is smaller than one kcal/mol.

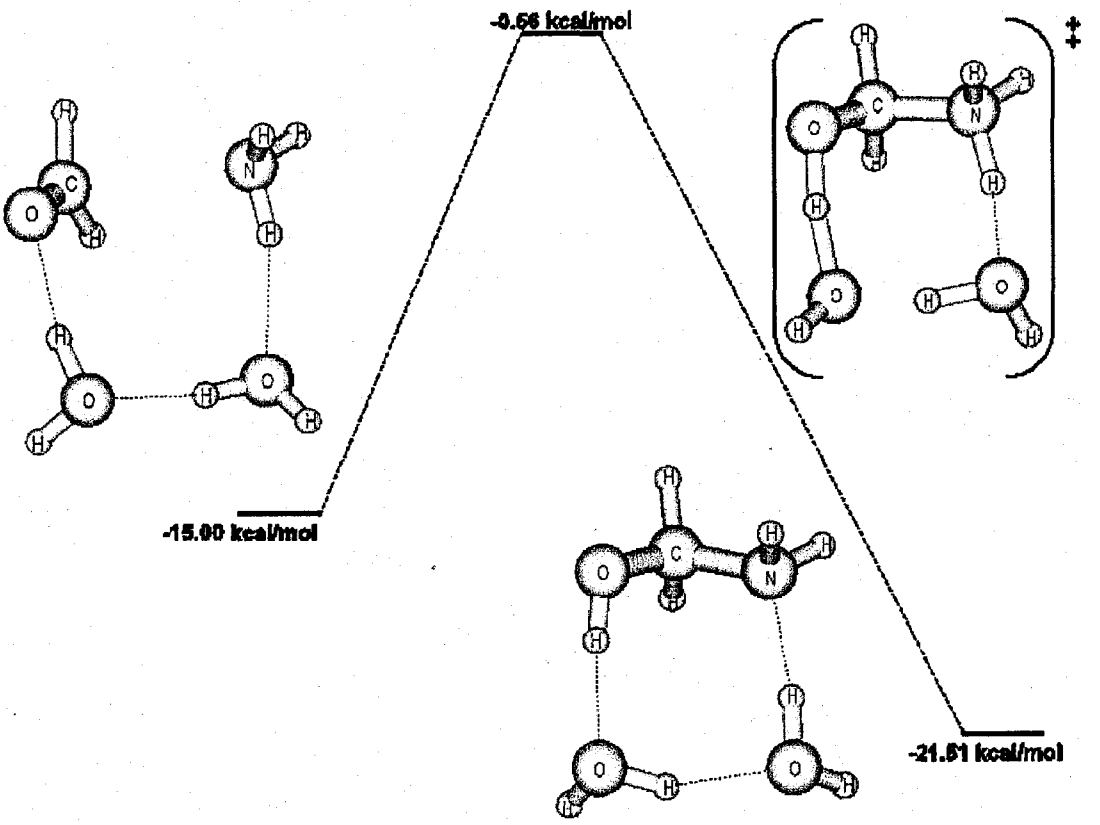

Figure 3-4 Energy profile for the reaction $NH_3 + H_2CO \rightarrow NH_2CH_2OH$ catalyzed by two water molecules at the CCSD(T)/6-311+G**//MP2/6-311+G** level (zero-point corrected energies, in kcal/mol, relative to the isolated molecules are reported).

In all three instances, the reaction is exothermic. Though the CCSD(T) single point calculations on the MP2 and B3LYP potential energy surfaces do not agree as well for the reaction energies as they do for the activation energies, both suggest that the reaction becomes more exothermic as one water molecule is added. This same trend occurs when a second water molecule is added. In all three cases, the ZPE corrections are taken into account. For the three systems in question, the ZPE-corrected CCSD(T) results on the B3LYP potential energy surface are roughly 2 kcal/mol lower than those on the MP2 potential energy surface.

Table 3-1 Selected bond lengths in Å at the various stationary points for the formation of NH_2CH_2OH, as calculated by MP2 and B3LYP using a 6-311+G** basis. The bonds are ordered in the opposite direction of the proton transfer, commencing with the hydrogen bond involving the carbon-bound oxygen atom.

	Reactive Complex		*Transition State*		*Product*	
	MP2	B3LYP	MP2	B3LYP	MP2	B3LYP
Non-Hydrated						
O···H	3.105	3.209	1.439	1.415	0.963	0.965
H-N	1.015	1.016	1.165	1.190	2.364	2.401
N-C	2.896	2.871	1.574	1.583	1.451	1.451
Mono-hydrated						
O···H	1.962	1.941	1.233	1.217	0.969	0.972
H-O	0.968	0.972	1.187	1.217	1.997	2.016
O···H	2.209	2.208	1.479	1.475	0.976	0.981
H-N	1.018	1.019	1.102	1.116	1.941	1.943
N-C	2.790	2.718	1.568	1.595	1.471	1.475
Di-hydrated						
O···H	1.844	1.812	1.129	1.134	0.975	0.979
H-O	0.973	0.980	1.286	1.298	1.800	1.816
O···H	1.834	1.810	1.358	1.334	0.975	0.978
H-O	0.972	0.979	1.082	1.109	1.817	1.806
O···H	2.073	2.035	1.502	1.501	0.986	0.992
H-N	1.020	1.023	1.091	1.101	1.827	1.828
N-C	2.732	2.601	1.550	1.573	1.479	1.485
Tri-hydrated						
O···H	1.811	1.774	1.064	1.080	0.973	0.977
H-O	0.975	0.983	1.387	1.375	1.810	1.810
O···H	1.777	1.756	1.223	1.224	0.977	0.983
H-O	0.976	0.983	1.174	1.187	1.765	1.754
O···H	1.808	1.786	1.389	1.382	0.980	0.986
H-O	0.974	0.981	1.064	1.078	1.740	1.736
O···H	2.044	2.003	1.491	1.507	0.987	0.994
H-N	1.021	1.024	1.094	1.098	1.824	1.825
N-C	2.715	2.565	1.532	1.558	1.476	1.482

Table 3-2 Total energies (in hartrees) of the reactive complex and zero-point energies (in kcal/mol) for all stationary points for each of the four systems studied at the various levels of theory employed in this work (a 6-311+G** basis is used in all instances).

	MP2 geometries		*B3LYP geometries*	
	MP2	CCSD(T)	B3LYP	CCSD(T)
Non-hydrated				
E, reactive complex	-170.662562	-170.706746	-171.129209	-170.700779
ZPE, isolated molecules	37.78		37.37	
ZPE, reactive complex	39.11		38.82	
ZPE, transition state	39.69		39.09	
ZPE, product	43.40		42.69	
Mono-hydrated				
E, reactive complex	-246.950303	-247.006012	-247.599676	-246.998060
ZPE, isolated molecules	51.04		50.47	
ZPE, reactive complex	54.96		54.63	
ZPE, transition state	56.27		55.27	
ZPE, product	59.40		58.57	
Di-hydrated				
E, reactive complex	-323.241408	-323.308529	-324.075242	-323.297920
ZPE, isolated molecules	64.31		63.57	
ZPE, reactive complex	71.00		70.58	
ZPE, transition state	71.63		70.34	
ZPE, product	75.15		73.93	
Tri-hydrated				
E, reactive complex	-399.531351	-399.609900	-400.549210	-399.608789
ZPE, isolated molecules	77.57		76.66	
ZPE, reactive complex	86.64		86.06	
ZPE, transition state	86.58		85.12	
ZPE, product	90.72		89.51	

Table 3-3 Activation energies in kcal/mol for the formation of CH_2NH_2OH as calculated by various levels of theory using a 6-311+G** basis (zero point energy corrected values in parentheses).

# of water molecules	*MP2 geometries*		*B3LYP geometries*	
	MP2	CCSD(T)	B3LYP	CCSD(T)
0	34.38 **(34.96)**	36.21 **(36.79)**	33.92 **(34.19)**	36.16 **(36.43)**
1	15.15 **(16.47)**	17.72 **(19.03)**	14.28 **(14.92)**	17.75 **(18.39)**
2	10.94 **(11.57)**	13.81 **(14.44)**	10.45 **(10.21)**	13.48 **(13.25)**
3	11.86 **(11.80)**	15.12 **(15.06)**	11.49 **(10.54)**	14.93 **(13.98)**

Table 3-4 Reaction energies in kcal/mol for the formation of CH_2NH_2OH as calculated by various levels of theory using a 6-311+G** basis (zero point energy corrected values in parentheses).

# of water molecules	*MP2 geometries*		*B3LYP geometries*	
	MP2	CCSD(T)	B3LYP	CCSD(T)
0	-9.71 **(-5.43)**	-9.03 **(-4.74)**	-8.38 **(-4.51)**	-10.12 **(-6.26)**
1	-11.46 **(-7.02)**	-10.72 **(-6.28)**	-9.88 **(-5.95)**	-11.92 **(-7.99)**
2	-11.42 **(-7.27)**	-10.65 **(-6.51)**	-9.50 **(-6.15)**	-12.16 **(-8.81)**
3	-12.77 **(-8.69)**	-11.97 **(-7.90)**	-10.11 **(-6.65)**	-12.31 **(-8.86)**

3.3.2 Trihydrated complex

As seen in section 3.3.1, a nearly 5 kcal/mol reduction in the activation energy is observed when a second water molecule is added. A third water molecule is added in order to determine if the activation energy is further altered when the concerted proton transfers occur via a longer chain. The CCSD(T)/6-311+G**//B3LYP/6-311+G** and CCSD(T)/6-311+G**//MP2/6-311+G** results are presented in Figures 3-5 and 3-6, respectively. For the smaller systems, the MP2 and B3LYP geometries and activation energies are similar. However, for this larger system, the B3LYP and MP2 potential energy surfaces are fundamentally different. The MP2 potential energy surface contains two additional stationary points along the reaction pathway, whereas the B3LYP potential energy surface does not. These points arise from an apparent intermediate that corresponds to a shortening of the C-N distance by roughly one Å to a distance of 1.65 Å. A concerted proton transfer and a further shortening of the C-N distance to its final value of 1.48 Å leads to the final product. This new stationary point does not correspond to a stable intermediate since addition of the ZPE corrections to the MP2/6-311+G** energies place this intermediate 0.7 kcal/mol higher in energy relative to the first transition state. Without the ZPE correction, the intermediate was 0.2 kcal/mol lower in energy than the first transition state. When the CCSD(T) single point calculations are performed at the MP2 optimized geometries, this stationary point is in fact higher in energy, whether or not ZPE corrections are added. On a final note, when the MP2 calculations are performed with a smaller 6-31G* basis, this stationary point on the MP2 potential energy surface vanishes and the structure relaxes to the initial reactive complex.

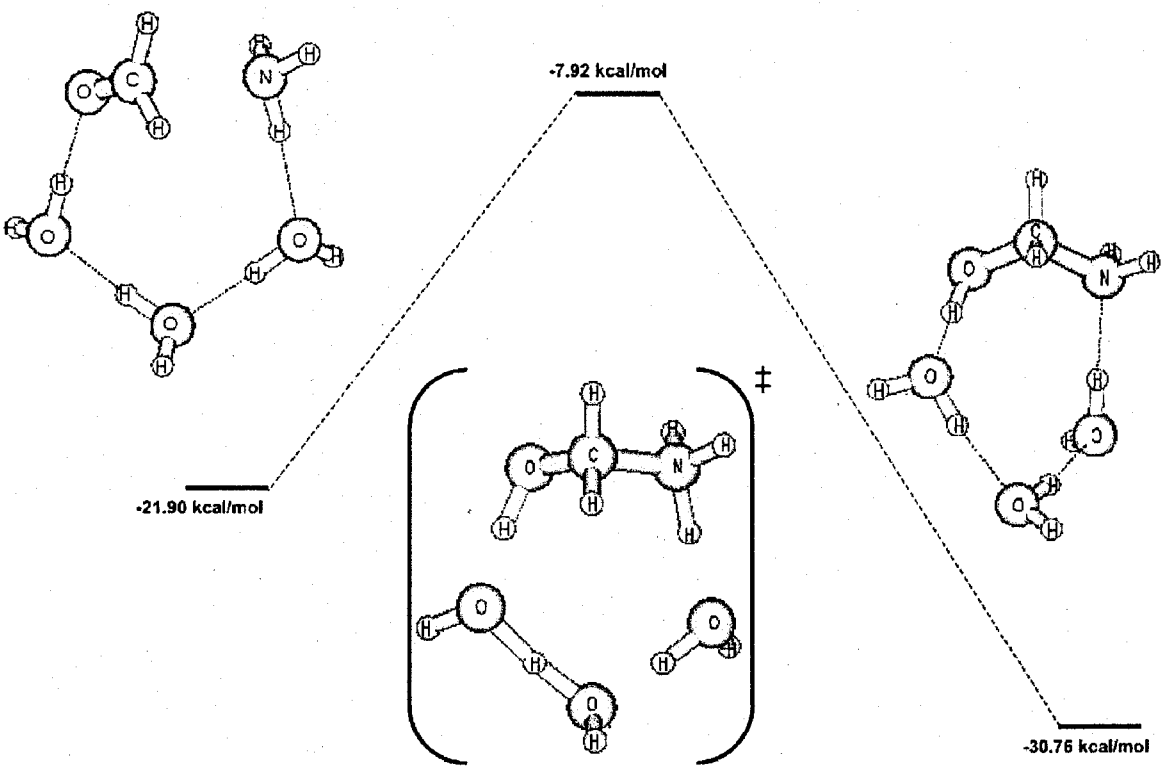

Figure 3-5 Energy profile for the reaction $NH_3 + H_2CO \rightarrow NH_2CH_2OH$ catalyzed by three water molecules at the CCSD(T)/6-311+G**//B3LYP/6-311+G** level (zero-point corrected energies, in kcal/mol, relative to the isolated molecules are reported).

Ignoring the above stationary point on the MP2/6-311+G** potential energy surface, the B3LYP and MP2 results are similar, as for the smaller systems. The energy difference between the reactive complex and the transition state is on the order of 14 kcal/mol and the overall reaction is exothermic by roughly 9 kcal/mol. The CCSD(T) calculations at the B3LYP geometries yield values of 14.0 and 8.9 kcal/mol, respectively. With the MP2 geometries, the results are 15.1 and 7.9 kcal/mol. Therefore, the addition of the third water molecule does not further decrease the activation energy. Rather, it slightly raises it by one kcal/mol.

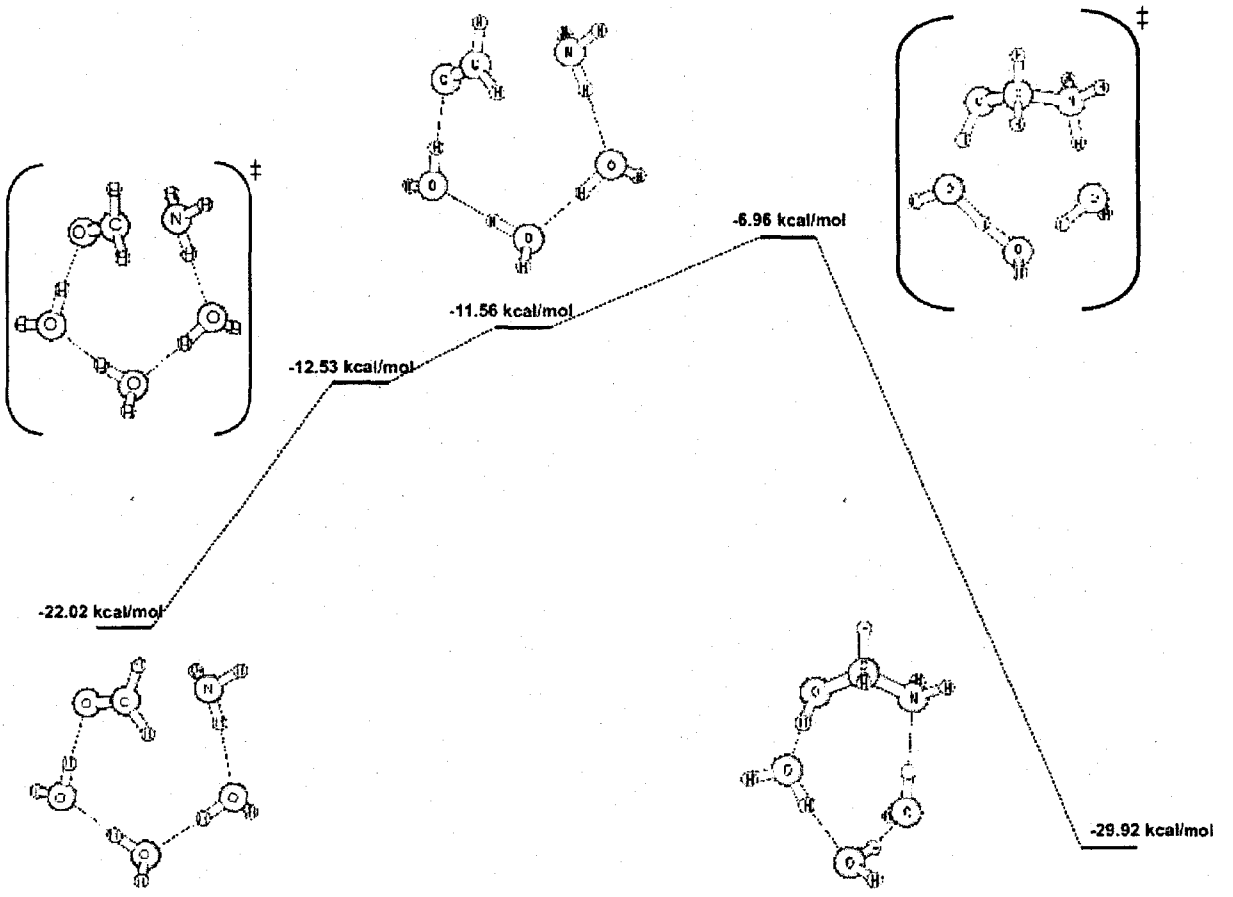

Figure 3-6 Energy profile for the reaction $NH_3 + H_2CO \rightarrow NH_2CH_2OH$ catalyzed by three water molecules at the CCSD(T)/6-311+G**//MP2/6-311+G** level (zero-point corrected energies, in kcal/mol, relative to the isolated molecules are reported).

Figure 3-7 places all of the preceding CCSD(T)//B3LYP energy profiles onto a single graph in order to give a better picture of the trends that arise upon the addition of water molecules.

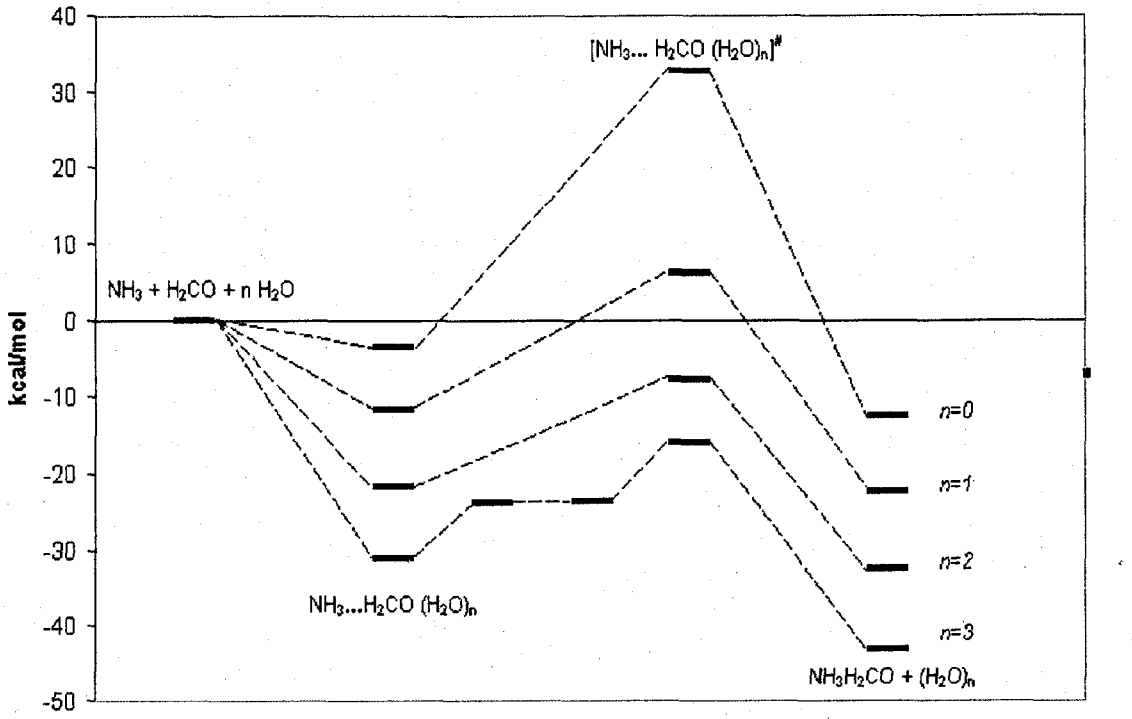

Figure 3-7 CCSD(T)/6-311+G**//MP2/6-311+G** energy profiles for NH_3 + H_2CO → NH_2CH_2OH in the absence and presence of one, two, and three water molecules (n=0-3) (zero-point corrected energies, in kcal/mol, relative to the isolated molecules are reported).

3.3.3 Structures

Table 3-1 lists the principal covalent and hydrogen bond lengths in each of the reactive complexes, transition states, and final structures. The final entry for each structure is the C-N bond length. It is important to note that all hydrogen and covalent bonds that are involved in the proton transfer chains discussed above appear in Table 3-1. The order in which these bond lengths are listed is the same as that found in the chain, starting with the hydrogen bond involving the carbonyl oxygen of formaldehyde, and ending with the N-H bond that is broken in ammonia. Generally, for the transition states, the covalent bonds become longer

and the hydrogen bonds get shorter as we follow the chain from the ammonia molecule to the formaldehyde molecule. Also, as the number of water molecules is increased from zero to three, the distance between the carbonyl oxygen and the hydrogen atom with which it hydrogen bonds in the reactive complex systematically drops, in the transition state, from 1.44 Å, to 1.23 Å, to 1.13 Å, and finally to 1.06 Å as water molecules are added to the proton transfer chain. The preceding are the MP2 results, but very similar results are obtained on the B3LYP potential energy surface.

3.3.4 Formation of the reactive complex

It is important to note that for all these reactions, ammonia is the proton donor. Previous studies [62, 115-118] indicate that when ammonia forms a single hydrogen bond to a water molecule or the water dimer, it prefers to be the proton acceptor. Therefore, it is important to account for the energetic cost that may arise when ammonia must reorient itself to form the reactive complexes shown in Figure 3-2 to 3-5. The present study indicates that when an ammonia molecule is in the presence of the water dimer, no stable structure exists in which the ammonia molecule is a proton donor. Stationary points are located but they are found to be transition states. The intrinsic reaction coordinate inevitably leads to the breaking of the hydrogen bond in which ammonia is the proton donor.

Therefore, the presence of formaldehyde must be essential to the ability of the ammonia molecule to serve as a proton donor within the present model systems. The formaldehyde molecule is already in place when the ammonia molecule reaches the reactive site. If the formaldehyde is absent, the ammonia molecule reorients itself to hydrogen bond to the dangling hydrogen atom that is otherwise blocked if a formaldehyde molecule is in place. It is important to note that on the surface of ice, the water molecules have a tendency to reconstruct to minimize the number of dangling hydrogen bonds.

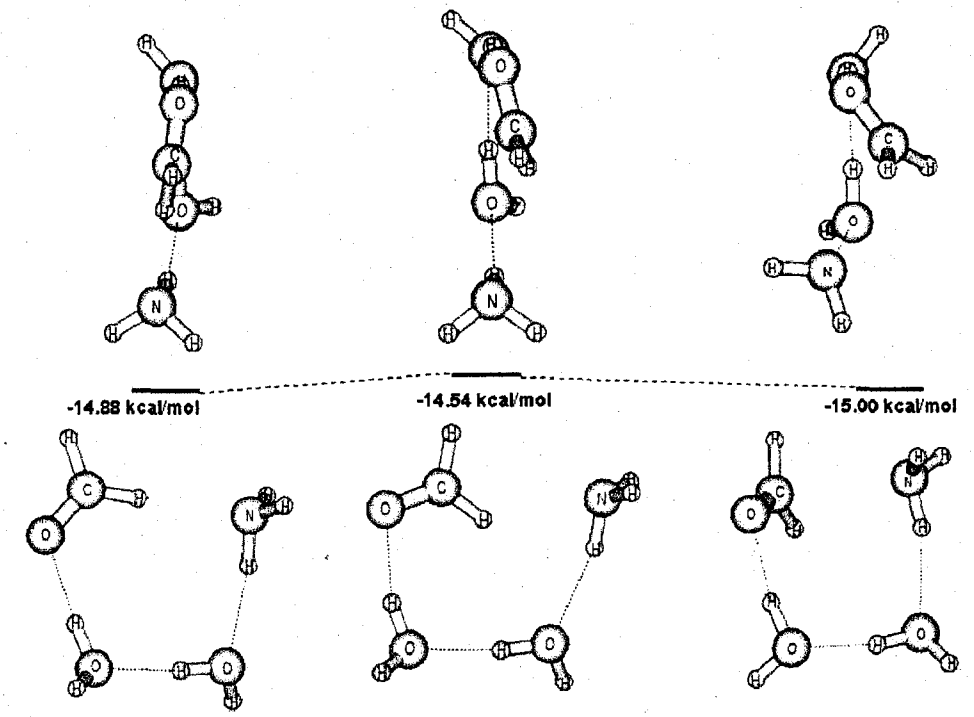

Figure 3-8 CCSD(T)/6-311+G**//B3LYP/6-311+G** energy profiles (top and side views) for the reorganization of the $H_2CO/(H_2O)_2$ complex upon approach of an NH_3 molecule to form the reactive complex of Figure 3-4 (zero-point corrected energies, in kcal/mol, relative to the isolated molecules are reported).

Figure 3-8 shows the process by which ammonia reacts with the formaldehyde / water dimer complex. When the ammonia arrives, it forms a single hydrogen bond to the water molecule not directly bound to the formaldehyde. The arrival of the ammonia molecule lowers the energy of the system by 4.7 kcal/mol. In this orientation, the lone pair on the nitrogen cannot readily attack the carbon atom. Therefore, the complex must undergo reorganization. As seen in Figure 3-8, the formaldehyde molecule pivots, thus exposing its carbon atom while the ammonia molecule slightly approaches the carbon atom. The activation energy for this process is very low. At the CCSD(T)/6-311+G**//MP2/6-311+G** level, the activation energy is only 0.34 kcal/mol. The reaction depicted in Figure 3-8 is slightly exothermic, with the final structure being 0.12 kcal/mol lower in energy than

the initial complex. Note that this final structure is the initial structure of the reaction depicted in Figure 3-4.

3.3.5 Conclusion

The addition of a water molecule to the ammonia/formaldehyde complex reduces the activation energy by a factor of two, from roughly 36 kcal/mol to 18 kcal/mol. Analogous results are found for the CCSD(T) calculations at both the B3LYP and MP2 optimized geometries. Adding the second water molecule reduces the activation energy further from roughly 18 kcal/mol to 13 kcal/mol. Again, use of the MP2 geometries yields similar findings. The addition of a third water molecule has little effect on the activation energy. In fact, the activation energy rises slightly, by roughly one kcal/mol.

The formation of NH_2CH_2OH is facilitated by a proton transfer from the nitrogen atom of ammonia to the oxygen atom of formaldehyde. This is accomplished either directly or indirectly via the chain of water molecules. Therefore, in the reactive complexes of the hydrated systems, the ammonia molecule must serve as proton donor while the water molecule serves as proton acceptor. Studies involving nucleophilic attack by ammonia indicate this is not often the case. However, in these systems, this situation arises if a gas phase ammonia molecule is brought into contact with an already hydrated formaldehyde molecule.

Such reactions can explain the formation of amino alcohols which have been detected spectroscopically in cometary media, albeit in trace quantities. It is hoped that, in contrast to periodic studies, cluster studies such as the one presented here provide a better depiction of the chemical processes occurring in the tail of a comet. Further studies could consider the life expectancy of the different complexes presented here in the cometary media. The broad variation of temperatures observed depending on the distance between the comet and a star makes this further study a very wide field of investigation.

Chapter 4
Cooperative effects in ice structures

4.1 Introduction

In theory, the existence of a hydrogen bond can be derived from geometrical considerations like the O-H···O angle (roughly 180°), H···O hydrogen bond lengths (typical values in water range between 1.8 and 2.3 Å) and hydroxyl bond lengths. In comparison to a free hydroxyl, the O-H bond length in water is larger by 0.01 Å. These effects can be explained by considering the cooperativity that occurs in small clusters of water molecules. As one increases the number of water molecules in a cluster from monomer to dimer, and further to larger oligomers, one sees non-negligible changes in binding energy and hydroxyl bond lengths [118].

It is important to get a better knowledge of cooperative effects if we are to properly model systems with molecular mechanical approaches. In these force fields, parameters are often derived from experiments or very reliable calculations on small systems where cooperativity may not have been considered. Typically this occurs when additivity rules are used to describe interactions via addition of contributions from smaller fragments. In such a case, effects from orbital or non-bonded interactions are neglected, leading to a poor description of hydrogen bonding. Cooperative effects have to be better understood and quantified if we are to use force fields where parameterized fragments are employed [119].

Electrostatic contributions to cooperativity have been shown to be crucial to the description of biological systems. For example, the interaction of an anion with the hydrogen bond network in a peptide displays considerable cooperativity, which can largely

be described by electrostatic interactions. The increase in cooperativity between the anion and the peptide has a profound effect on the catalysis. Interactions of this nature have been shown to occur frequently in enzyme-catalyzed reactions, and are often the driving force for the reaction. However, these cooperative effects cannot be properly described by the sum of pair-wise interactions between the anion and the individual peptide units. This phenomenon arises from non-additive many-body effects [120, 121] that can be defined by the following decomposition scheme

$$\Delta E_{N>2} = BE_{system} - \sum_{\substack{i=1 \\ j>i}}^{N} \Delta E_{i,j} \qquad 4\text{-}1$$

where BE_{system} is the total binding energy and $\Delta E_{i,j}$ is the interaction energy of each dimer subunit.

Ab initio studies have shown that cooperative effects strongly affect the properties of water clusters by enhancing the hydrogen bond network [122-124]. They can have a significant influence on the energy and structure of a metal-water interface by favouring the growth of a water bi-layer on the metal surface. A detailed analysis concluded that this cooperativity is dominated by effects originating from directly connected water trimers. However, as the number of directional hydrogen bonds in the bi-layer is small, these three-center energies cannot force the bi-layer into a geometry which is similar to that observed at the surface of bulk ice [125].

Cooperativity in many-particle systems becomes important when the effective intensity of interactions between particles depends on the number of particles. Cooperativity is defined as an enhancement of the first hydrogen bond between a donor and an acceptor as a result of a second hydrogen bond being formed between one (or both) of these species and a third partner. It has been shown that water trimers and tetramers are strongly stabilized by

cooperative effects when each water molecule is simultaneously a hydrogen bond donor and acceptor (resulting in a cyclic topology) [126, 127].

Natural bond orbital analysis attributes cooperativity to non-additive charge-transfer interactions among local bond orbitals [128]. Charge transfer from the hydrogen donor lone pairs to the hydrogen acceptor antibonding O-H orbital slightly destabilizes the hydrogen acceptor lone pairs. In the case where the hydrogen acceptor also acts as a donor in another hydrogen bond, the destabilization will reinforce the interaction between the lone pairs and anti-bonding O–H orbital of the new acceptor. As a result, a new hydrogen bond is formed. Both electrostatic interactions and charge transfer seems to play a role in the cooperative effects present in hydrogen-bonded systems. A recent study quantified the influence of each, indicating that the hydrogen bond involves donation and back-donation of charge between the oxygen lone pair and the O-H antibonding orbitals on neighboring molecules. Together with internal s-p re-hybridization, this minimizes the repulsive charge overlap of the connecting oxygen and hydrogen atoms, which is essential for a strong attractive electrostatic interaction [129].

As an alternative to *ab initio* calculations, the B3LYP and BLYP DFT functionals seem the best at accounting for non-pairwise effects. It has been previously shown that these functionals provide a good description of hydrogen-bonded systems [130-132]. However, more recent work has indicated that these methods may not be the best for a proper description of hydrogen bonding [133-136]. A preferred method is one which includes very flexible basis sets and a proper account of electron correlation. However, it has also been shown that the electronic redistribution that plays a large part in the cooperative effect is accurately described at the Hartree-Fock level. The basis set superposition error also seems to play a role, but we will not consider it here, accounting for a cancellation in the subtraction calculation of the cooperative effects [137]. The BSSE for the n+1 water molecules structure will be close to the BSSE for the n water molecules structure.

The main objectives of this work are to determine the extent of the cooperative effects in water ice structures and determine the minimum size a cluster can have such that it can be used to mimic the cooperativity in bulk ice. In order to achieve this, two models are used. The first model considered is one that is taken from the structure of ice XI, where the length of the chains are considerably longer than those used in previous studies. In a second step, a periodic model is also employed.

4.2 Models

To study cooperative effects, we choose to study both clusters and periodic systems. For the clusters, we wish to have simple and well-defined systems. One of the simplest possibilities is a linear chain of water molecules. However, a geometry optimization of a linear chain will result in cyclic or compact structures. This occurs because the water molecules try to minimize their energy and in a vacuum this is done through increased interactions with one another. As a result, full geometry optimizations will yield a structure that is not desired. Simple models wherein the hydrogen bonds are forced to remain along a straight line were studied. However, this constraint does not allow for the proper overlap of orbitals between adjacent water molecules. Due to the importance of orbital interactions in cooperativity [138] (i.e., the orbital interpretation of hydrogen bonding in terms of charge transfer from donor lone pairs to acceptor antibonding σ^*_{OH}), this failure to properly account for it leads to dramatically reduced cooperative effects. Clearly, an alternative model must be considered. The structure of ice XI [66, 75] is used as a starting point because this particular phase is the low-temperature form of ordinary ice, ice Ih, and is therefore proton-ordered [67, 68]. To construct the linear chains, we take one edge of the hexagon that one would see as you look down upon the 100 surface of ice XI (Figure 4-1). In all subsequent calculations, the water molecules are frozen. The only geometric parameters that are optimized are those

associated with the ions interacting with the water chains. For the periodic ice systems, the structure of a polar cubic ice [139] is taken.

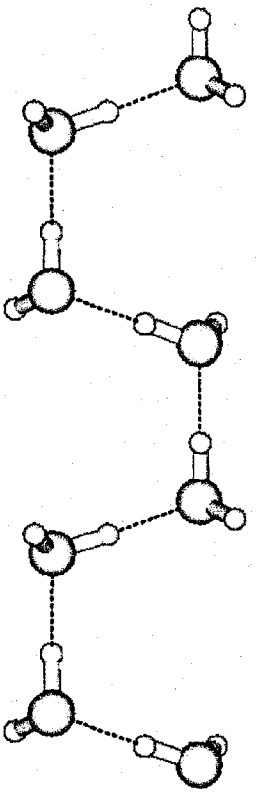

Figure 4-1 Water chain structure.

As stated above, any geometry optimization involving a cluster of water molecules would lead to the formation of cyclic or compact structures. However, when studying the interaction between the water chain and the Na^+ and Cl^- ions, the position of the ions are fully optimized. Since the purpose of this work is to better understand the reactivity at the ice surface, only structures where ions are adjacent to a terminal water molecule are of interest. Even with these constraints in place, multiple minima are found. In the case of the chloride ion, four possible starting structures are considered. Three of these structures are shown in Figure 4-2, and are labelled structures 2A, 2B, and 2C. A fourth structure (3D, not

shown), in which the Cl^- ion is initially placed on the axis that bisects the terminal water molecule at the top of the chain, is not stable and will generate either structure 2A or 2B upon optimization. For the sodium ion, four possible structures are proposed. These structures differ in the identity of both the oxygen atom and lone pair upon which it is oriented. All four yield a stable structure upon optimization but they converge to either of the two geometries illustrated in Figure 4-3. Geometry optimizations are carried out at the B3LYP/6-31G** level. Subsequent single-point calculations with more sophisticated methods and basis sets are limited to the lowest energy structures (Tables 4-6 & 4-7).

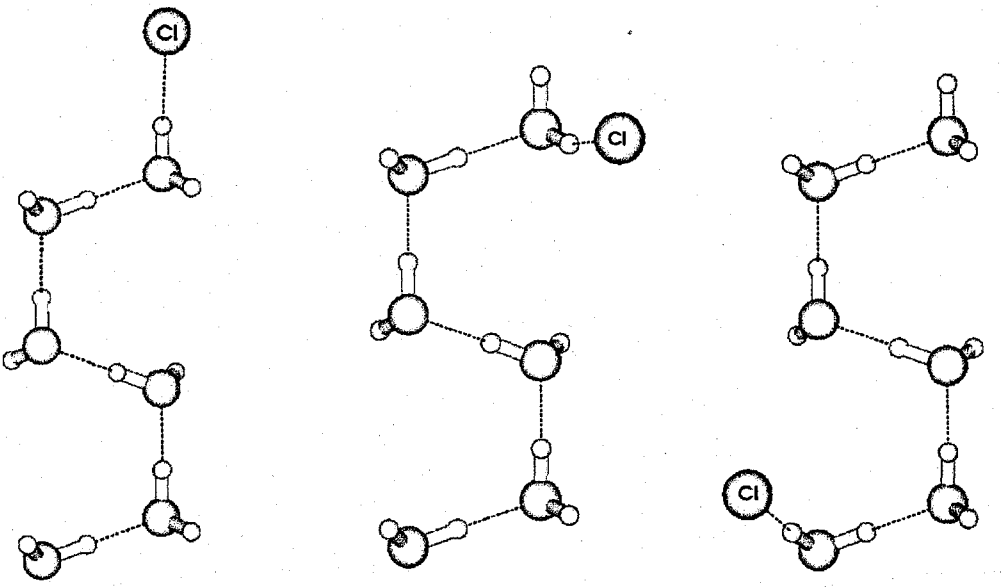

Figure 4-2 Water chain with chloride anion structures.

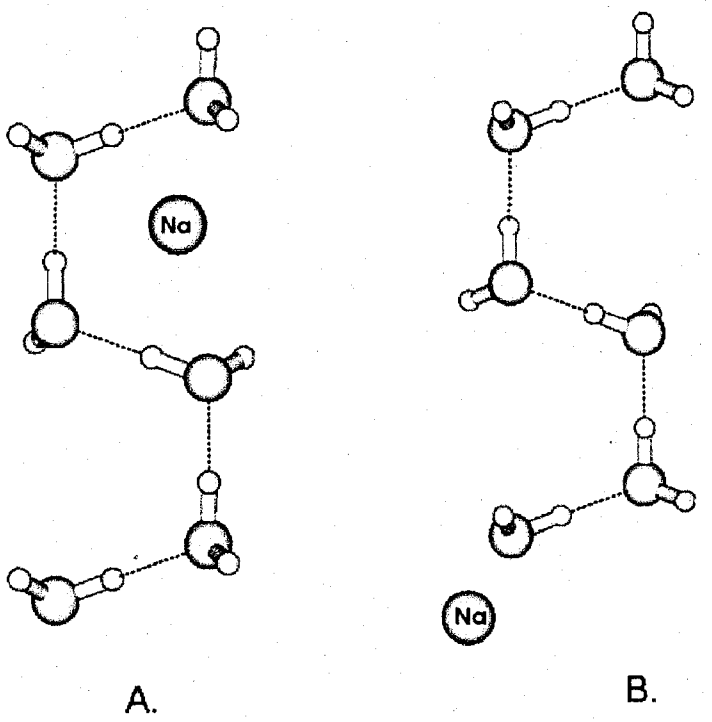

Figure 4-3 Water chain with the sodium cation structures.

For the periodic calculations on the slabs of ice, one side of the system has hydrogen atoms protruding at angles of roughly 90° while the other side has oxygen atoms at the surface. For the studies with the chloride ion, geometry optimizations are performed with the ion positioned directly above the protruding hydrogens. For the calculations with the sodium ions, the ions are initially positioned on the opposite side of the slab, in a bridging position between two oxygen atoms (Figure 4-4).

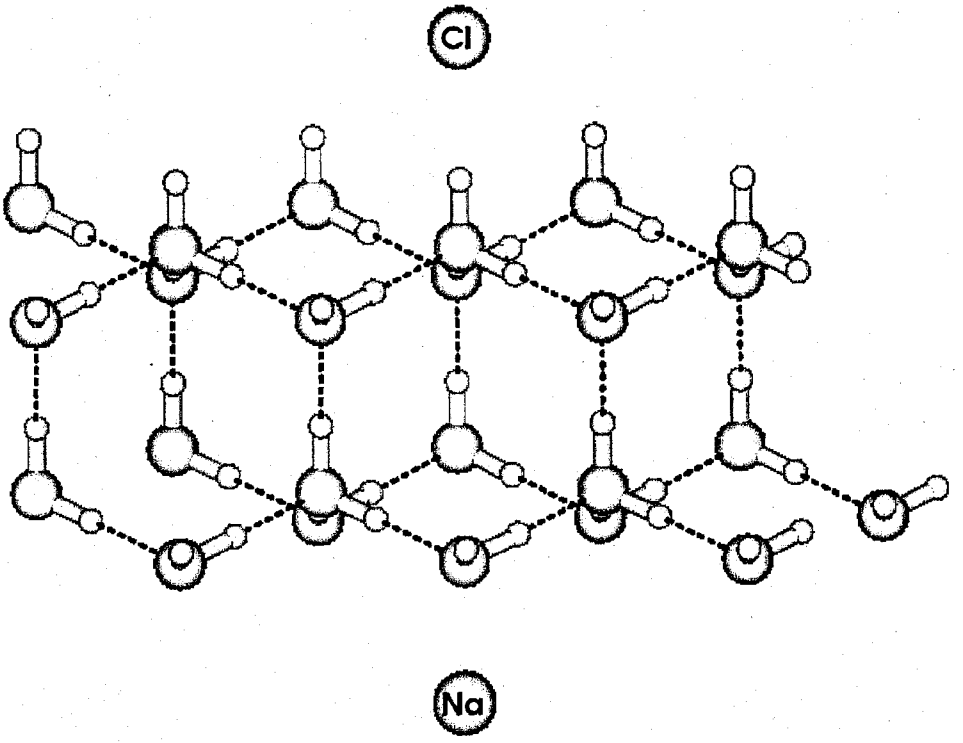

Figure 4-4 Periodic structure (2 bi-layered slab) showing the positions of the chloride anion and sodium cation adsorbed at the ice surface.

4.3 Computational Methods

All calculations on the clusters were performed using Gaussian 98 [112]. The density functionals (B3LYP and PW91) and ab initio (MP2 and CCSD(T)) methods were employed. For each of these levels of theory, a 6-31G** basis set was used. In order to monitor the effect of basis set quality on our computed results, calculations employing the 6-311+G** basis set and B3LYP level of theory were performed.

All calculations on the periodic systems were performed using VASP [140], where the PW91 functional [141] was employed. Core electrons were described by ultra-soft pseudo-potentials [142] and a plane wave basis set with an energy cutoff of 515 eV was used to describe the valence electrons. The integrations in the Brillouin zone are performed on a grid of 5x5x1 using the Monkhorst-Pack method [143]. Unlike the clusters, full geometry optimizations were performed on the periodic systems using the conjugate gradient method.

4.4 Cooperative Effects

The strength of the interaction between any molecule (be it an ion, or a polar or non-polar molecule) and a collection of water molecules will not only depend on the positions and number of water molecules in direct contact with it. The remaining molecules in the hydrogen-bond network of water will also influence the strength of this interaction. In order to quantify this co-operative effect present in such a system, we have studied two very simple models. The first was a cluster-type model that represents a "linear" chain of water molecules, which was previously described in the above section of this chapter. Such a simple model will allow us to feasibly and directly monitor the importance of distant water molecules on local interactions. Moreover, the fact that the system was constrained to a "linear" chain meant that the issue of the multiple minima problem was avoided altogether. The second was a model of a slab of ice satisfying periodic boundary conditions. This model would clearly provide a far more realistic picture of the interaction between ice and an adsorbate. By comparing the results of the calculations on the clusters with those of the slabs, one can estimate the importance of lateral interactions at the ice surface.

For the linear chains of water molecules, three distinct cases were studied. The first model was built by the addition of a new water molecule to the end of the chain. The second and third models were built by the addition of a Cl^- anion or a Na^+ cation to the end of these chains, respectively. For each of these cases, the strengths of the co-operative

effects were monitored. For the "linear" chain of water molecules, the importance of cooperativity was quantified by using the following expression

$$E_{coop} = \left(E_{nH_2O} - E_{(n-1)H_2O} - E_{H_2O}\right) - \left(E_{2H_2O} - 2E_{H_2O}\right) \qquad 4\text{-}2$$

To calculate the energy due to cooperative effects, total energies were required from ab initio or density functional calculations on four separate systems - the water chain with *n* water molecules, the water chain with *n-1* water molecules, the water dimer, and the water molecule itself. The equation above isolates the influence of cooperativity as the energy arising from the first set of parentheses is the strength of the hydrogen bond between the chain of *n-1* water molecules and a newly added water molecule while the energy arising from the second set of parentheses gives the same for the water dimer. If we state that, by definition, no cooperativity can exist within the water dimer, then the difference between these two values in parentheses can be defined as the component of the overall hydrogen bond strength directly attributable to cooperative effects (i.e., the presence of the other water molecules not directly involved in the formation of the new hydrogen bond).

Also monitored for the chains of water molecules was the mean hydrogen bond energy, defined as

$$E_{mean\ HB} = \left(E_{nH_2O} - nE_{H_2O}\right) \Big/ n-1 \qquad 4\text{-}3$$

Its value provided information about the extent of stabilization within the system as the length of the chain is altered.

Similarly, the effect of cooperativity on the binding of the Cl^- and Na^+ ions is given by

$$E_{coop} = \left(E_{nH_2O \bullet ion} - E_{nH_2O} - E_{ion}\right) - \left(E_{H_2O \bullet ion} - E_{H_2O} - E_{ion}\right) \qquad 4\text{-}4$$

In this instance, the interaction between a single water molecule and the ion is defined as that which is devoid of any cooperative effects.

For periodic systems, the formula must be modified to account for the formation of multiple hydrogen bonds when an extra bi-layer is added to the system. For our particular unit cell, six new inter bi-layer hydrogen bonds were formed each time a bi-layer was added. It was important to note that numerous hydrogen bonds existed within each bi-layer, but their number was unaffected by the number of bi-layers in the unit cell. Thus, there was no unique value for the strength of a single hydrogen bond, as we have with the water dimer for the water clusters. Cooperativity within bare ice can thus be defined as

$$E_{coop} = (E_{n\ bilayer} - E_{(n-1)\ bilayer} - E_{1\ bilayer})/6 \qquad 4\text{-}5$$

Analogous to the expression for chain models, the cooperativity for a periodic system can alternatively be expressed as

$$E_{coop}^{BIS} = (E_{n\ bilayer} - E_{(n-1)\ bilayer} - E_{1\ bilayer}) - (E_{2\ bilayers} - 2E_{1\ bilayer}) \qquad 4\text{-}6$$

Our results showed that these two formulae provided different, but similar, results. Cooperativity for the case of an ion adsorbed to the surface of a slab of ice is defined as

$$E_{coop} = (E_{n\ bilayer \bullet ion} - E_{(n-1)\ bilayer} - E_{1\ bilayer \bullet ion})/6 \qquad 4\text{-}7$$

4.5 Results and Discussion

The cooperative effects for the water chain, calculated at various levels of theory, are listed in Table 4-1. Table 4-2 lists the mean hydrogen bond energies. When analyzing the geometries of the water chain, a shortening of approximately 0.08 Å is observed within the

terminal hydrogen bond. Table 4-1 shows that as the length of the water chain increases, the strength of the hydrogen bond also increases.

Table 4-1 Cooperative effects (in kcal/mol) using various methods and basis sets for chains of water molecules taken from the Ice XI crystallographic structure.

	Cooperative effect				
	B3LYP/6-31G**	B3LYP/6-311+G**	PW91/6-31G**	MP2/6-31G**	*CCSDT/6-31G***
$2H_2O$	0	0	0	0	0
$3H_2O$	-4.40	-3.64	-4.46	-4.36	-4.31
$4H_2O$	-4.85	-4.11	-5.00	-4.79	-4.73
$5H_2O$	-4.92	-3.96	-5.03	-4.83	-4.78
$6H_2O$	-5.11	-4.24	-5.29	-5.04	-4.97
$7H_2O$	-5.46	-4.42	-5.59	-5.34	-5.28
$8H_2O$	-5.41	-4.50	-5.59	-5.32	-5.25
$9H_2O$	-5.58	-4.52	-5.72	-5.45	
$10H_2O$	-5.45	-4.54	-5.64	-5.36	
$11H_2O$	-5.67	-4.60	-5.82	-5.54	
$12H_2O$	-5.52	-4.60	-5.71	-5.42	
$13H_2O$	-5.71	-4.63	-5.85	-5.57	
$14H_2O$	-5.53	-4.61	-5.72	-5.44	
$15H_2O$	-5.74	-4.66	-5.88	-5.60	
$16H_2O$	-5.55	-4.63	-5.74	-5.46	
$17H_2O$	-5.75	-4.67	-5.90	-5.61	
$18H_2O$	-5.56	-4.64	-5.75	-5.46	
$19H_2O$	-5.77	-4.68	-5.91	-5.63	
$20H_2O$	-5.57	-4.64	-5.76	-5.47	
$21H_2O$	-5.77				
$22H_2O$	-5.57				
$23H_2O$	-5.78				
$24H_2O$	-5.58				
$25H_2O$	-5.78				
$26H_2O$	-5.58				
$27H_2O$	-5.79				

Table 4-2 Mean hydrogen bond energies (in kcal/mol) using various methods and basis sets for chains of water molecules taken from the Ice XI crystallographic structure.

	mean H-bond energy				
	B3LYP/6-31G**	B3LYP/6-311+G**	PW91/6-31G**	MP2/6-31G**	CCSD(T)/6-31G**
2 H_2O	-5.92	-4.28	-7.30	-5.28	-4.74
3 H_2O	-8.12	-6.10	-9.52	-7.46	-6.90
4 H_2O	-9.00	-6.86	-10.45	-8.33	-7.76
5 H_2O	-9.46	-7.21	-10.92	-8.78	-8.20
6 H_2O	-9.77	-7.47	-11.25	-9.09	-8.50
7 H_2O	-10.04	-7.68	-11.52	-9.34	-8.76
8 H_2O	-10.22	-7.83	-11.72	-9.52	-8.93
9 H_2O	-10.38	-7.96	-11.88	-9.67	
10 H_2O	-10.49	-8.05	-12.00	-9.78	
11 H_2O	-10.60	-8.14	-12.11	-9.89	
12 H_2O	-10.68	-8.20	-12.19	-9.96	
13 H_2O	-10.76	-8.26	-12.27	-10.03	
14 H_2O	-10.81	-8.31	-12.33	-10.09	
15 H_2O	-10.87	-8.36	-12.39	-10.14	
16 H_2O	-10.91	-8.39	-12.43	-10.18	
17 H_2O	-10.96	-8.43	-12.48	-10.23	
18 H_2O	-10.99	-8.46	-12.51	-10.26	
19 H_2O	-11.03	-8.48	-12.55	-10.29	
20 H_2O	-11.05	-8.51	-12.58	-10.32	
21 H_2O	-11.08				
22 H_2O	-11.10				
23 H_2O	-11.13				
24 H_2O	-11.15				
25 H_2O	-11.17				
26 H_2O	-11.18				

Table 4-3 Cooperative effects (in kcal/mol) for chains of water molecules taken from the ice XI structure with Cl^-.

	Cooperative effect					terminal bond length
	B3LYP/6-31G**	B3LYP/6-311+G**	PW91/6-31G**	MP2/6-31G**	CCSD(T)/6-31G**	B3LYP/6-31G**
$Cl^- \cdot H_2O$	0	0	0	0	0	2.160
$Cl^- \cdot 2H_2O$	-9.69	-8.25	-10.21	-9.23	-9.13	2.058
$Cl^- \cdot 3H_2O$	-13.92	-12.06	-14.62	-13.27	-13.13	2.027
$Cl^- \cdot 4H_2O$	-15.73	-13.54	-16.59	-14.97	-14.45	2.015
$Cl^- \cdot 5H_2O$	-18.27	-16.01	-19.16	-17.45	-16.88	2.005
$Cl^- \cdot 6H_2O$	-19.46	-16.96	-20.46	-18.53	-17.94	2.002
$Cl^- \cdot 7H_2O$	-20,69	-18.26	-21.66	-19.75		1.998
$Cl^- \cdot 8H_2O$	-21.16	-18.56	-22.23	-20.16		1.996
$Cl^- \cdot 9H_2O$	-22.01	-19.52	-23.02	-21.02		1.995
$Cl^- \cdot 10H_2O$	-22.34	-19.68	-23.44	-21.29		1.994
$Cl^- \cdot 11H_2O$	-22.91	-20.38	-23.95	-21.89		1.993
$Cl^- \cdot 12H_2O$	-23.06	-20.37	-24.19	-21.99		1.993
$Cl^- \cdot 13H_2O$	-23.51	-20.96	-24.57	-22.48		1.992
$Cl^- \cdot 14H_2O$	-23.62	-20.90	-24.76	-22.53		1.992
$Cl^- \cdot 15H_2O$	-23.97	-21.40	-25.04	-22.92		1.992
$Cl^- \cdot 16H_2O$	-24.01	-21.28	-25.16	-22.91		1.992
$Cl^- \cdot 17H_2O$	-24.31	-21.73	-25.39	-23.26		1.991
$Cl^- \cdot 18H_2O$	-24.33	-21.59	-25.49	-23.22		1.991
$Cl^- \cdot 19H_2O$	-24.59	-22.00	-25.67	-23.53		1.991
$Cl^- \cdot 20H_2O$	-24.58	-21.83	-25.74	-23.46		1.991

Table 4-4 Cooperative effects (in kcal/mol) for chains of water molecules taken from the ice XI structure with Na^+.

	Cooperative effect					terminal bond length
	B3LYP/6-31G**	B3LYP/6-311+G**	PW91/6-31G**	MP2/6-31G**	CCSD(T)/6-31G**	B3LYP/6-31G**
$Na^+ \cdot H_2O$	0	0	0	0	0	2.186
$Na^+ \cdot 2H_2O$	-13.73	-11.53	-14.04	-13.09	-12.98	2.139
$Na^+ \cdot 3H_2O$	-17.85	-14.72	-18.47	-16.85	-16.70	2.127
$Na^+ \cdot 4H_2O$	-19.95	-16.26	-20.73	-18.79	-18.62	2.126
$Na^+ \cdot 5H_2O$	-22.94	-19.01	-23.78	-21.67	*	2.117
$Na^+ \cdot 6H_2O$	-24.67	-20.63	-25.53	-23.34	*	2.113
$Na^+ \cdot 7H_2O$	-25.88	-21.75	-26.81	-24.49		2.111
$Na^+ . 8H_2O$	-26.55	-22.36	-27.49	-25.12		2.110
$Na^+ . 9H_2O$	-27.41	-23.17	-28.38	-25.95		2.109
$Na^+ \cdot 10H_2O$	-27.96	-23.70	-28.93	-26.48		2.109
$Na^+ \cdot 11H_2O$	-28.44	-24.16	-29.44	-26.95		2.108
$Na^+ \cdot 12H_2O$	-28.74	-24.44	-29.74	-27.23		2.108
$Na^+ \cdot 13H_2O$	-29.12	-24.81	-30.14	-27.60		2.107
$Na^+ \cdot 14H_2O$	-29.38	-25.06	-30.40	-27.86		2.107
$Na^+ \cdot 15H_2O$	-29.63	-25.30	-30.67	-28.10		2.107
$Na^+ \cdot 16H_2O$	-29.80	-25.45	-30.83	-28.26		2.107
$Na^+ \cdot 17H_2O$	-30.01	-25.66	-31.05	-28.47		2.107
$Na^+ \cdot 18H_2O$	-30.16	-25.80	-31.20	-28.61		2.107
$Na^+ \cdot 19H_2O$	-30.31	-25.95	-31.36	-28.76		2.106
$Na^+ \cdot 20H_2O$	-30.42	*	-31.46	*		2.106

The resulting value of approximately 6 kcal/mol is roughly the value of the hydrogen bond itself between the two units of the water dimer. Once the chain length reaches 20 water molecules, the value of the cooperative effect is essentially constant, except for a steady alternation between even and odd numbered systems. A change in the cooperativity of only 0.01 kcal/mol is seen when the length of the water chain is increased from 20 to 26 molecules. This is less than 0.2% of the total effect for the even number of water molecules in the chain. For an odd number of water molecules in the chain, the same trend is observed, with a change of less than 0.4% of the total effect seen for more than 21 molecules in the chain.

Further examination of the 6-31G** results shows that the cooperative effect consistently increases as one goes from CCSD(T) to MP2 to B3LYP and finally to PW91. However, in the case of an $8H_2O$ system (the largest system feasible with CCSD(T)), this difference spans only 0.34 kcal/mol upon going from CCSD(T) to PW91. However, increasing the quality of the basis set from 6-31G** to 6-311+G**, the value of the cooperative effect falls by roughly 1 kcal/mol at the B3LYP level. Thus, the extent of cooperativity is significantly affected by the quality of the basis set. However, the discrepancy between the values is relatively unaffected by the length of the chain. In order to confirm that these values will not change significantly when a more flexible basis set is used, B3LYP calculations were performed on these systems up to the pentamer with a very large 6-311++g(3df,2dp) basis. The results from these calculations show that the numerical results move to less negative values (i.e. a decrease in cooperativity) and do not change by more than 0.3 kcal/mol compared to the 6-311+G** basis. However, the oscillating behaviour in the cooperative effect seen with the 6-311+G** basis between the trimer, tetramer and pentamer, which is absent with the smaller basis set, is again seen with the very large basis set. For longer chains of water molecules, the cooperative effect is clearly converging, despite the fact that it is oscillating. This oscillation between odd and even-numbered chains arises from the positioning of the newly added water molecule. The odd-numbered water molecules are oriented such that the total dipole moment of the chain increases while the even-numbered water molecules are oriented such that it does not.

Mulliken population analysis is clearly not the best way to study charge transfer. Nonetheless it can provide a qualitative picture of the charge redistribution within the cluster. The charge on the terminal oxygen atom of the water chains goes from -0.618006 for the monomer to -0.697422 for the chain with 20 water molecules. This increase in the charge, which can explain the increase in the reactivity, comes for the most part from the formation of the first three hydrogen bonds. In fact, 81% of the charge transfer arises from the formation of the dimer. Another 9% is gained upon the addition of a third molecule and another 7% of the total charge transfer arises from the formation of the tetramer. Therefore, the tetramer accounts for 97% of the charge transfer to the first water molecule that is seen in the chain with 20 water molecules. This would suggest that the cooperative effect arising from charge transfer is terminated primarily upon the formation of the tetramer.. The increase in the chain's dipole moment accounts for the increase in cooperativity once the chains become significantly longer.

Despite the quick convergence of the charge transfer with chain length, the mean hydrogen bond energies converge slowly as system size is increased. The creation of a new hydrogen bond stabilizes the entire hydrogen bond network, and this stabilization is fairly constant across the various theoretical models employed. Though the results are converging, they are not as converged as one would think at first glance since the impact of the newly formed hydrogen bond, regardless of its strength, diminishes as the total number of hydrogen bonds in the chain increases and attenuates the effect of this new hydrogen bond. For the largest systems in our table, the mean hydrogen bond strength is roughly twice the value of the lone hydrogen bond in the water dimer. A significant fraction of this increase in the mean hydrogen bond strength is gained upon the addition of the first few water molecules to the chain.

Table 4-5 B3LYP/6-31G** energies for the different positions for Cl^- (in kcal/mol).

	Position A	Position B	Position C
$Cl^- \cdot 2H_2O$	N/A	N/A	N/A
$Cl^- \cdot 3H_2O$	0.00	+2.03	+3.05
$Cl^- \cdot 4H_2O$	0.00	+4.40	+27.57
$Cl^- \cdot 5H_2O$	0.00	+3.18	+33.21
$Cl^- \cdot 6H_2O$	0.00	+2.28	+36.18
$Cl^- \cdot 7H_2O$	0.00	+2.08	+39.04
$Cl^- \cdot 8H_2O$	0.00	+2.12	+40.46
$Cl^- \cdot 9H_2O$	0.00	+1.82	+42.22
$Cl^- \cdot 10H_2O$	0.00	+1.61	+43.12
$Cl^- \cdot 11H_2O$	0.00	+1.52	+44.31
$Cl^- \cdot 12H_2O$	0.00	+1.51	+44.84
$Cl^- \cdot 13H_2O$	0.00	+1.41	+45.70
$Cl^- \cdot 14H_2O$	0.00	+1.33	+46.07
$Cl^- \cdot 15H_2O$	0.00	+1.29	+46.74
$Cl^- \cdot 16H_2O$	0.00	+1.28	+46.97
$Cl^- \cdot 17H_2O$	0.00	+1.24	+47.50
$Cl^- \cdot 18H_2O$	0.00	+1.20	+47.67
$Cl^- \cdot 19H_2O$	0.00	+1.18	+48.12
$Cl^- \cdot 20H_2O$	0.00	+1.18	+48.22

As previously stated, structures in which the chloride ion is started along the axis bisecting the water molecule (structure 2D) will inevitably optimize to either structure 2A or 2B. For all chains with three or more water molecules, structure 2A is the lowest in energy (Table 4-5). This structure results from the chloride ion being favourably oriented along the dipole of the chain. Though bound to the same water molecule, the chloride ion in structure 2B is positioned perpendicular to the chain's dipole. The energy difference between structures 2A and 2B decreases steadily (beyond the trimer) because the difference in positioning becomes less of a factor as the chain lengthens and the dipole increases. This

trend does not necessarily hold for the trimer since the dipole is oriented somewhat in between positions 2A and 2B. Beyond the trimer, position 2A is clearly more aligned along the chain's dipole. Meanwhile, in structure 2C, the chloride ion is bound to the opposite end of the chain and is thus unfavourably positioned along the chain's dipole. Consequently, structure 2C is always the highest in energy for these chains involving three or more water molecules, and its relative energy rises steadily as the chain lengthens and its dipole increases. As was just described, this trend does not hold for the trimer. As one can see, our model for the water chain repeats every four units, so the trimer is unique, as expected. For the water dimer, positions 2A and 2B yield slightly different results. However, this is purely an artefact of our model and our constrained geometry optimizations. Positions 2A and 2B would become identical were we to fully optimize the geometries. In our model, the two bonds in any water molecule, taken from reference [66], are not strictly identical. When starting the partial optimization of structure 2C, the chloride ion migrates to the other water molecule, yielding either structure 2A or 2B.

The cooperative effects for the chloride ion bound to the water chain, calculated at various levels of theory, are listed in Table 4-3. For the given geometries, it can be seen that the cooperative effects lead to a significant shortening of approximately 0.17 Å of the distance between the water chain and the chloride anion. This shortening of the bond becomes more or less constant once one attains a chain of ten or more water molecules. These calculations also show that the cooperative effect in these systems can easily approach values of 20 to 25 kcal/mol. This is a significant amount given that the interaction energy between a single water molecule and a chloride anion is on the order of 17 kcal/mol. Even with chains of up to 20 water molecules, convergence in the cooperative effect has not been achieved.

The B3LYP/6-311+G** and CCSD(T)/6-31G** calculations are perhaps the most informative. First limiting ourselves to the 6-31G** calculations with the various methodologies, we can see that the cooperative effect consistently increases upon going from

CCSD(T) to MP2, B3LYP and finally to PW91. For the largest system for which CCSD(T) calculations were feasible, the difference between the CCSD(T) and the PW91 results is on the order of 2.5 kcal/mol. However, it seems that this discrepancy between the CCSD(T) and PW91 methods converges quickly to this value. For this particular system, which contains an anion, the presence of diffuse functions is clearly important. Upon going from the 6-31G** basis to the 6-311+G** basis, the value of the cooperative effect diminishes by roughly 2.5 kcal/mol at the B3LYP level. It would be safe to assume that a similar reduction would exist amongst the other methodologies. Upon going to the even more flexible 6-311++G(3df,2dp) basis set, B3LYP calculations up to the pentamer confirm that the same trend is observed with a change of no more than 0.6 kcal/mol compared to calculations employing the 6-311+G** basis. In all instances, the numerical results become more negative (i.e., they move back towards the values obtained with the 6-31G** basis).

For the longer chains, little change is seen in the cooperative effect if one adds a single water molecule to a water chain with an odd number of water molecules. This result is deceiving because in such instances the water chain's dipole moment increases by very little. However, for chain lengths of 18 and 20 water molecules, we see a surprisingly consistent increase of roughly 0.25 kcal/mol across all of the theoretical methods employed. The value of the cooperative effect is indeed converging since increases of 0.30 and 0.40 kcal/mol are seen amongst the even-numbered chains two and four units shorter, respectively. However, convergence is clearly slow. The Mulliken population analysis is not very informative in this case because the negative charge on the chlorine diminishes constantly and convergence is never really achieved.

The two initial structures in which the sodium ion is initially positioned along a lone pair of the oxygen atom at the upper extremity of the chain in Figure 4-3 will optimize to structure 3A. One of these two initial positions being already occupied by a hydrogen of the neighbouring molecule forming a hydrogen bond, the position of the sodium cation is more like between the lone pairs. The two initial structures in which the sodium ion is initially

positioned along a lone pair of the oxygen atom at the lower extremity of the chain (as shown in Figure 4-3) will optimize to structure 3B. For all chains with three or more water molecules, structure 3A has the lowest energy as shown in Table 4-6. Structure 3A is the lowest energy structure since the sodium cation is closer to the chain interacting with several hydrogen atoms. In this position, it is favourably positioned along the chain's dipole. The energy difference between structures 3A and 3B increases steadily because the difference in positioning becomes more of a factor as the chain lengthens and the dipole increases.

Table 4-6 B3LYP/6-31G** energies for the different positions for Na^+ (in kcal/mol).

	Position A	Position B
$Na^+ \cdot 2H_2O$	0.00	0.00
$Na^+ \cdot 3H_2O$	0.00	+2.39
$Na^+ \cdot 4H_2O$	0.00	+17.82
$Na^+ \cdot 5H_2O$	0.00	+30.21
$Na^+ \cdot 6H_2O$	0.00	+34.95
$Na^+ \cdot 7H_2O$	0.00	+38.91
$Na^+ \cdot 8H_2O$	0.00	+41.02
$Na^+ \cdot 9H_2O$	0.00	+43.16
$Na^+ \cdot 10H_2O$	0.00	+44.51
$Na^+ \cdot 11H_2O$	0.00	+45.72
$Na^+ \cdot 12H_2O$	0.00	+46.56
$Na^+ \cdot 13H_2O$	0.00	+47.37
$Na^+ \cdot 14H_2O$	0.00	+48.02
$Na^+ \cdot 15H_2O$	0.00	+48.55
$Na^+ \cdot 16H_2O$	0.00	+49.03
$Na^+ \cdot 17H_2O$	0.00	+49.41
$Na^+ \cdot 18H_2O$	0.00	+49.82
$Na^+ \cdot 19H_2O$	0.00	+50.09
$Na^+ \cdot 20H_2O$	0.00	+50.42

For the lowest energy structure, the cooperative effect for the sodium ion bound to the water chain, calculated at various levels of theory, is listed in Table 4-4. For the geometries of structure 3A, it can be seen that the cooperative effects lead to a shortening of roughly 0.08 Å between the water chain and the sodium cation. This shortening of the bond converges to a constant value at chain lengths of ten or more water molecules. These calculations show that the cooperative effect in these systems can easily reach a value of 30 kcal/mol. This amount is of the same order as the interaction energy between a single water molecule and a sodium cation (31 kcal/mol). Even with chains of up to 20 water molecules, the energetic value of the cooperative effect has not fully converged.

Calculations employing the 6-31G** basis set with the various methodologies show that the cooperative effect consistently increases upon going from CCSD(T) to MP2, B3LYP and finally to PW91. For the largest system for which CCSD(T) calculations were feasible, the difference between the CCSD(T) results and the PW91 results is on the order of 2.1 kcal/mol. It is assumed that this discrepancy between the CCSD(T) and PW91 methods is quickly converging to a value of this order, as is the case for the chloride anion. Upon going from the 6-31G** to the 6-311+G** basis, the value of the cooperative effect diminishes by more than 4 kcal/mol for the longest chain at the B3LYP level. Upon going to the increasingly flexible basis set 6-311++g(3df,2dp), B3LYP calculations up to the pentamer confirm the same trend, and the results do not change by more than 0.8 kcal/mol compared to the 6-311+G** basis. Analogous to the observations made for the chains with the chlorine ion, the numerical results become more negative (i.e., they change in the direction of values obtained with the 6-31G** basis).

For the longer chains, the increase in the cooperativity upon the addition of a water molecule to the chain seems to slowly converge to a value of 0.15 kcal/mol across all of the theoretical methods employed. Similar to the results of the chloride anion, the Mulliken population analysis does not provide interesting information. The positive charge on the sodium decreases constantly and is not converged for the longest chain studied.

For the bare ice periodic calculations, systems comprised of one, two, and three bi-layers were studied. Larger structures could not be studied due to a large computational burden. Limited to these three systems, a strong cooperative effect can be demonstrated, but convergence is far from being reached. The values obtained are roughly twice those found for the chains of water molecules. However, as there is an inherent difference in the orbital bases in the cluster and periodic calculations, lateral interactions in the slabs within a bi-layer, and multiple new hydrogen bonds created once two bi-layers come into contact, results that are of the same range are perhaps as good as we could expect.

As the first formula for the estimate of the cooperativity is normalized by the number of new hydrogen bonds created upon the addition of a new bi-layer, one can perhaps compare such a value with the mean hydrogen bond energy in the chains of water molecules. The PW91 values in Table 4-2 are very close to the values listed in Table 4-7 for the periodic systems. The second estimated value for the cooperativity, E_{coop}^{BIS} (the bold value in Table 4-7) which uses the formula that is as close as possible to the one used for the clusters, still provides a value comparable to E_{coop}. Even if the cooperative effects are more difficult to clearly quantify unambiguously for periodic structures, the range of values is the same.

Table 4-7 Cooperative effects (in kcal/mol) for slabs of bare ice and ice with adsorbed ions (Cl^- or Na^+).

	Cooperative effect in PW91/plane waves			*terminal bond length*	
	Ice	**Ice with Cl-**	**Ice with Na+**	*O-H···Cl*	*Na···O*
1 bilayer	0	0	0	1.93	2.43
2 bilayers	-7.31	-2.60	-8.18	1.73	2.16
3 bilayers	-9.06	-3.68	-8.39	1.76	2.13
	-10.49				

Though the periodic structures are a far more realistic model than are the chains of water molecules, there are still some issues to be solved before these calculations become comparable to what is observed. In reality, this model structure would undergo a

reconstruction so as to avoid dangling bonds. This will create more of a "molten" structure where the hydrogen bond network will not be perfect. This would lead to a smaller cooperative effect due to a poorer orbital overlap and a diminished dipole moment.

The structure with the chloride anion adsorbed onto the top of slab displays a much smaller cooperative effect. This may be the result of the chosen ice structure where a strong dipole moment exits oriented towards the chloride ion normal to the surface. A decrease in the distance between the anion and the slab is observed and convergence appears rapidly.

The structure with the sodium cation adsorbed at the bottom of the slab displays a strong cooperative effect that is similar in magnitude to the one found for the pure slabs of ice. A significant shortening of the Na···O distance is observed, analogous to the ice structure with the adsorbed chloride anion. Again, even for our limited number of bi-layers, convergence seems to be occurring rapidly. The smaller radius cation can approach the slab more than a larger anion and therefore has a stronger interaction with the slab.

4.6 Conclusion

This study shows the importance of cooperative effects in modelling ice structures. Cooperativity has a major influence on the stability of these structures, particularly when they involve ions. Charge transfer and electrostatic effects are responsible for cooperativity and may be the reason why, in some cases, convergence could not be achieved. Through the calculations on the small clusters, it was shown that a small cluster cannot be used to mimic an ice structure. This is a direct result of the missing cooperativity in such a model. A cluster embedded in a Madelung potential is a reasonable improvement in more accurately accounting for the cooperative effects. This approach will be discussed further in the following chapter.

Chapter 5

X-ray absorption spectroscopy of water ice structures

5.1 Theoretical Background

Several techniques have been developed to study the unoccupied electronic states of molecules and solids, such as electron energy loss spectroscopy (EELS), X-ray absorption spectroscopy (XAS), and X-ray Raman scattering (XRS). XAS, also called *near edge X-ray absorption fine structure* (NEXAFS) or *X-ray absorption near edge structure* (XANES), has proven to become a powerful method to probe unoccupied states. Therefore it is a very useful technique for gaining information about the structure and properties of materials [144].

Since the core energy levels depend not only on the element but also on their chemical environment, XAS provides an element specific probe of the local neighborhood of a given atom, facilitated by the spatial confinement of the core hole. The X-ray absorption process being faster than a femto-second (much faster than the vibrational and translational motions), XAS will picture the molecular orbital structure in a frozen geometry around the probed molecules, the spectrum being a sum of snapshots from individual atoms or molecules in their instantaneous environments [144].

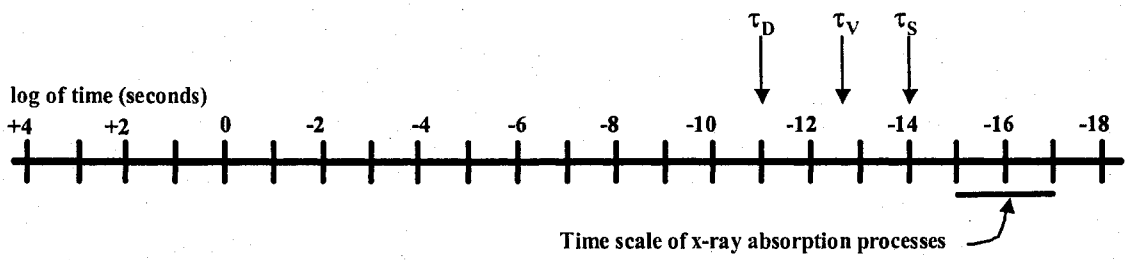

Figure 5-1 Time scale of molecular processes in water compared with the time scale of X-ray absorption processes. The vertical arrows indicate the periods associated with different molecular processes (molecular displacement τ_D, molecular vibrations τ_V, OH stretching vibration τ_S). [145]

When a beam of monochromatic X-rays goes through a material, the photons interact with the atoms. X-ray absorption spectroscopy measures the absorption of the incoming X-rays as a function of their energy. The absorption coefficient, which is determined from the decay in intensity with distance, generally decreases with increasing energy. However, at particular energies, sharp peaks, call edges, arise. Those energy positions are unique to the given type of atom that absorbs and reflect the excitation energy of inner-shell electrons. The region close to an edge is often dominated by strong scattering processes as well as local atomic resonances and is referred to as XANES or NEXAFS. This will be the region of the spectrum we will be concerned with in this thesis. Above the edges, one gets a series of oscillatory structure that modulate the absorption (EXAFS). This fine structure contains precise information about the local atomic structure around the atom that absorbed the x-ray [146].

The photon ionization energy (E_0) is the threshold energy the electron needs to have to escape into the continuum and E_C is the critical energy value for EXAFS in Figure 5-2.

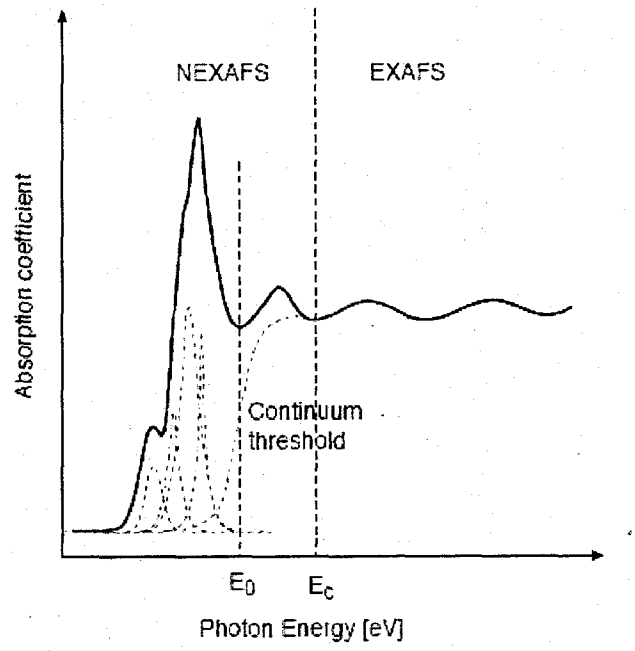

Figure 5-2 An x-ray absorption edge is the superposition of discrete transitions from the core electron to discrete bound state valence levels (dotted lines) [145].

Three types of excited electrons can be found. The first type does not have enough energy to leave the absorbing atom and will do a transition to one of the unoccupied valence states. These transitions will give the so-called pre-edge peaks, that is the peaks located before the ionization threshold E_0. The second and third types of excited electrons have energies above E_0 and therefore can escape into the continuum. However, for the second type of excited electrons, the kinetic energy is low and therefore the electron can be trapped in continuum states before leaving the system. For the third type of excited electron, the energy of the incoming photons is above the critical energy value E_C, and the electron will be weakly backscattered by neighboring atoms. The interference between the outgoing electron wave from the probed atom and the backscattered electron waves from its nearest neighbors creates sinusoidal variations of the absorption coefficient [144].

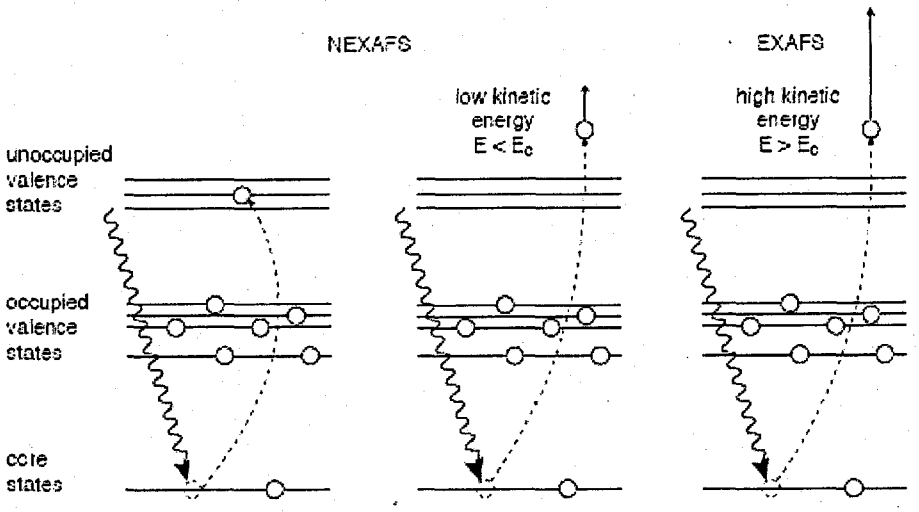

Figure 5-3 The three types of excited electrons [145].

5.2 X-ray absorption spectrum calculation

The calculation of an X-ray absorption spectrum will be discussed within the framework of the density functional theory [144, 147-149]. The absorption cross section σ_x of an atom or molecule, previously introduced, is defined as the number of electrons excited per unit of time divided by the number of incident photons per unit of time per unit of area and can be calculated from Fermi's Golden Rule:

$$\sigma(\omega) = 4\pi^2\alpha\hbar\omega\sum_f \left|\langle\Psi_f|\Theta|\Psi_i\rangle^2\right|\delta(E_f - E_i - \hbar\omega) \qquad 5\text{-}1$$

where α is the fine structure constant, $\hbar\omega$ is the energy of the incoming photon, Θ is a transition operator coupling the initial state Ψ_i of energy E_i with the final states Ψ_f of energies E_f. Ψ_i and Ψ_f are Kohn-Sham orbitals, solutions to equation 1-47.

The calculation of Ψ_i, a core orbital, is straightforward but the difficulty lies in the calculation of the final states Ψ_f. The absorption cross section can also be related to the transition probability per unit time P_{if} from the initial state to the final states driven by a harmonic time-dependent perturbation $V(t) = \bar{V} e^{-i\omega t}$ due to the electric field of the radiation

$$P_{if} = \frac{2\pi}{\hbar}\langle \Psi_f | \bar{V} | \Psi_i \rangle^2 \rho_f(E) \qquad 5\text{-}2$$

where $\rho_f(E)$ is the energy density of the final states.

The excitation of the core electron into the unoccupied valence states obeys the dipole selection rule, which, for an atom, states that only the transition between states whose angular momentum differs by one unit will have a non-zero probability: $(\Delta l) = \pm 1$.

K-shell transitions (from the 1s shell) will be our sole concern in the present work. The spatial localization of the 1s orbital involved in the excitation results in the spectrum being dominated by transitions to molecular orbitals with a local p-orbital contribution, although the overall symmetry is not atomic-like.

The Born-Oppenheimer approximation can be applied here as the vibrational motions of the nuclei are slow compared to the total lifetime of the electronic final state. Therefore, it allows the separation of the electronic and nuclear degrees of freedom and the ground state equilibrium geometry can be used. The Frank-Condon principle, also referred to as the sudden approximation, which states that the internuclear distance can be assumed to be constant during the fast electronic excitation process, can also be employed. The effects of nuclear vibrations can, however, be included through the wavefunctions of the initial and final states by writing them as a product of the electronic and vibrational functions. In X-ray

absorption, only the resonances arising from bound state transitions are narrow enough to have a reasonable resolution of the vibrational splittings. The wavefunctions Ψ_i and Ψ_i determine the transition intensities via the dipole matrix element and the energy differences give the transition energies.

In the case of *K*-shell spectra, the 1s ionization potential is the minimum energy necessary to promote a 1s electron to the continuum states. In order to obtain the transition energies, one has to calculate the energy difference between the ground state (initial state) and the final excited states. In the Hartree-Fock approximatiom, Koopmans' theorem links the ionization potentials (or binding energies) to the orbital energies by stating that the binding energy of an electron is equal to the negative of its orbital energy. It assumes that, upon excitation, the other orbitals will remain frozen.
Calculating a spectrum will imply multiple calculations to determine the final states and is computationally infeasible with today's resources. Approximations will therefore be employed to yield sufficiently accurate results in a single calculation.

The shape of a spectrum comes from the eigenstates of the final states which include the core hole but the transition intensities are given by the number of unoccupied levels in the initial state, i.e. the ground state.

Kohn-Sham density functional theory has only been proven for the ground state. Nevertheless it has been used to calculate some excitation energies. Within the density functional theory, Slater introduced a concept called the "transition state method" (or transition operator or half-core hole) for the Xα method [39, 150]. It allows one to include the relaxation effects due to the creation of the core hole by second order perturbation theory. Janak extended Slater's theorem to density functional theory [151]. However, it has been proven that in order for the density functional theory to be variational, the occupation numbers should be chosen such as all the orbitals below the Fermi level are completely occupied and the orbitals above the Fermi level are empty with possible fractional

occupations at the Fermi level [152]. This means that Janak's theorem does not theoretically apply within the current framework of density-functional calculations, but it is nevertheless used and provides reasonable results [153]. This method brings a balance between the effects of the initial and final states in the calculation of a spectrum. Hence, the binding energy, which does not take relaxation into account, is usually given by

$$E_b(l) = -E_l = \overline{E}_0(n_l = 0) - \overline{E}_0(n_l = 1) = -\frac{\partial \overline{E}_0(n_l)}{\partial n_l} \qquad 5\text{-}3$$

where n_l gives the occupation numbers for the spin orbital. Within the Slater transition state method, the binding energy becomes

$$E_b(l) = \overline{E}_0^R(n_l = 0) - \overline{E}_0^R(n_l = 1) = -\left.\frac{\partial \overline{E}_0(n_l)}{\partial n_l}\right|_{n_l = 1/2} \qquad 5\text{-}4$$

Equation 5-3 can be further simplified by using the dipole approximation and the X-ray absorption cross section and the spectral intensity can be rewritten as

$$\sigma = \frac{4\pi^2\hbar^2}{m^2}\frac{e^2}{\hbar c}\frac{1}{\hbar\omega}\sum_f \left|\langle \Psi_f | \bar{e}\cdot\bar{p} | \Psi_i \rangle^2\right| \rho_f(E)$$

$$\sigma = \frac{4\pi^2\hbar e^2}{m^2 c}\frac{\rho_f(E)}{\hbar\omega}\frac{1}{3}\left\{\left|\langle \Psi_f | \bar{p}_x | \Psi_i \rangle\right|^2 + \left|\langle \Psi_f | \bar{p}_y | \Psi_i \rangle\right|^2 + \left|\langle \Psi_f | \bar{p}_z | \Psi_i \rangle\right|^2\right\} \qquad 5\text{-}5$$

$$\sigma = \frac{4\pi^2\hbar e^2}{m^2 c}\frac{\rho_f(E)}{\hbar\omega}\frac{1}{3}\left|\langle \Psi_f | \bar{p} | \Psi_i \rangle\right|^2$$

$$I_{if} = \frac{2}{m\hbar\omega}\langle \Psi_f | \bar{e}\cdot\bar{p} | \Psi_i \rangle^2$$

where $\bar{p}$ is the sum of the momentum operators of all the k electrons $\bar{p} = \sum_{k=1}^{N} \bar{p}_k$ and $\bar{e}$ gives the x-ray polarization direction.

Ultimately, the expression can be written using the dipole moment operator $\overline{\mu}$ instead of the momentum operator ("length" gauge):

$$I_{if} = \frac{2}{3}\omega_{if}\left\langle \Psi_f \left| \overline{\mu} \right| \Psi_i \right\rangle^2 \qquad 5\text{-}6$$

Using the relaxed wavefunction given by the Slater transition state method, a set of energy levels and their corresponding oscillator strengths can be determined in order to obtain the simulated spectrum [144, 147-149, 154].

5.3 Results

5.3.1 Ice IX

To simulate the Xray absorption spectra presented in this section, the core-valence and core-virtual transition energies and corresponding dipole transition probabilities were evaluated using the Slater transition method within the dipole approximation where both initial and final states are taken from the same wave function as explained in the previous section [155-157].

The methodology was tested on ice IX because the experimental XAS spectrum is known. The procedure being successful in reproducing this spectrum, it was then applied to the three other proton-ordered ice structures and with an appropriate sampling to the water and amorphous ices. The following results were obtained performing calculations within the DFT framework implemented in the program deMon-StoBe [158] with the gradient-corrected exchange and correlation functionals PBE developed by Becke, Perdew and Wang [159]. The calculation results in a discrete set of energy levels associated with an oscillator strength and a line broadening. The experimental broadening of a transition depends on instrumentation,

life-time and vibrational broadening that can be simulated by convoluting the obtained total oscillator strengths with gaussian functions. These gaussians are of constant width below the ionization potential (for the transitions below 540.1 eV, line widths of 0.3, 0.5, 0.7 and 0.9 eV were used to illustrate the influence of the experimental resolution on the observed line shape). They have linearly increasing full width at half maximum (fwhm) from the ionization potential up to a threshold (between 540.1 and 550.1 eV, the line width was interpolated linearly between the two limiting values) and are constant again after the said threshold (for the transitions above 550.1 eV, the absorption lines were broadened with the full width at half maximum of 4.5 eV). Larger lifetime broadening at higher energies motivates the choice of linearly increasing fwhm. The method has been shown to give a reliable description of X-ray absorption spectra.

The cluster models were generated from the ordered crystal structures described in Chapter 2. For each crystallographically distinct oxygen center, all water molecules within a chosen cut-off radius were explicitly included in the electronic calculation. The cutoff radius was selected such that the total TIP3P dipole moment (-0.834 charge on the oxygen atom and 0.417 charge on each hydrogen atom) [90] of the cluster is minimized as can be seen in Tables 5-1 to 5-4. For site 1, the quantum clusters studied have radii of 3.3, 4.8, 5.4, 6.7, and 7.3 Å when for site 2, the chosen radii are 3.6, 4.1, 5.8, 6.9, and 7.2 Å. The oxygen atom positioned at the center of the cluster is the excited atom.

In Chapter 4, it was shown that co-operative effects could extend over very long distances. However, the amount of charge transfer unto a single water molecule seemed to be, in most part, constant once the hydrogen bond chain extended beyond four. Beyond this, the co-operative effect appeared to be primarily electrostatic in nature. Therefore, it is likely that a computational approach in which a quantum mechanical region is embedded within a Madelung potential will work well. Within the quantum mechanical region positioned around a central water molecule, the effects of charge transfer unto this central molecule can be accounted for as the optimal electronic distribution will be obtained. Beyond this

quantum mechanical cluster, a Madelung potential will be able to replace the electrostatic effects that would have been generated by water molecules that would otherwise have been treated, at great cost, by a purely quantum mechanical treatment. Therefore, the influence of the long-range Madelung potential of the crystal [160, 161] on the electronic structure and XAS spectrum of the cluster will be estimated by surrounding each cluster with point charges placed at the hydrogen and oxygen periodic lattice positions [162]. The magnitude of the charges has been calculated by applying the following screening function to the TIP3P water charges:

$$\frac{1}{1+e^{\frac{(R-R_0)}{D}}} \qquad 5\text{-}7$$

Within the QM region, the electrostatic potential of this charge distribution is identical to the Madelung potential of the infinitely periodic structure.

The following basis set were employed as they have been proven by previous studies to perform well on the studied systems [163]:

- central oxygen atom

  all electron Huzinaga 11s 7p basis set contracted according to the 5111111/211111 scheme and augmented with two sets of d polarization functions, i.e. the IGLO III basis set (O (11s, 7p, 2d) → [7s, 6p, 2d]) [164-166], describes the initial electron density prior to excitation. For the calculation of dipole transition probabilities, the central oxygen basis set used the more diffuse (19*s*, 19*p*, 19*d*) basis set which describes the density in extended regions above the ionization potential and was augmented with 19 diffuse even tempered basis shells.

- remaining oxygen atoms (chemically inert core electrons)

  effective 1s core potential and 311/211 split-valence [167].

- hydrogen atoms
  polarized split valence 311/1.

For the ice IX structure, the values in Equation 5-7 were chosen to be R_o=15-40 and D=2-4. The spectra were calculated for each crystallographically non-equivalent oxygen and the average spectrum was calculated by averaging the transition intensities for each transition energy accounting for the 1:2 ratio between the number of oxygen sites 1 and 2 in ice IX

The calculated ionization potential for site 1 is 538.23 eV and 538.06 eV for site 2.

Cluster Radius (Å)	# water molecules	TIP3Pdipole moment (D)
2.5	1	2.36
2.6	1	2.36
2.7	1	2.36
2.8	4	4.35
2.9	5	5.83
3.0	5	5.83
3.0	5	5.83
3.1	5	5.83
3.2	5	5.83
3.3	5	5.83
3.4	6	7.24
3.5	6	7.24
3.6	8	6.87
3.7	9	7.84
3.8	9	7.84
3.9	9	7.84
4.0	11	4.97
4.0	11	4.97
4.1	11	4.97
4.2	14	4.40
4.3	14	4.40
4.4	15	5.13
4.5	17	4.50
4.6	19	3.05
4.7	19	3.05
4.8	19	3.05
4.9	21	7.71
5.0	23	6.86
5.0	23	6.86
5.1	23	6.86
5.2	24	4.73
5.3	25	2.83
5.4	25	2.83
5.5	29	6.57
5.6	29	6.57
5.7	30	8.45
5.8	30	8.45
5.9	34	13.71
6.0	34	13.71
6.0	34	13.71
6.1	34	13.71
6.2	36	10.17
6.3	39	11.88
6.4	40	10.84
6.5	40	10.84
6.6	43	11.51
6.7	53	5.56
6.8	58	5.75
6.9	62	7.06
7.0	65	8.06
7.0	65	8.06
7.1	65	8.06
7.2	65	8.06
7.3	68	3.03
7.4	70	3.45
7.5	72	3.05
7.6	74	6.97
7.7	74	6.97
7.8	81	11.93
7.9	85	14.38
8.0	86	13.09

Table 5-1 TIP3P dipole moments vs. the radius size of the clusters for the oxygen site 1 of the ice IX structure

Cluster Radius (Å)	# water molecules	TIP3P dipole moment (D)
2.5	1	2.29
2.6	1	2.29
2.7	1	2.29
2.8	3	2.27
2.9	5	6.55
3.0	5	6.55

Cluster Radius (Å)	# water molecules	TIP3P dipole moment (D)
3.0	5	6.55
3.1	5	6.55
3.2	5	6.55
3.3	5	6.55
3.4	5	6.55
3.5	5	6.55
3.6	5	6.55
3.7	7	6.56
3.8	7	6.56
3.9	7	6.56
4.0	11	1.97

Cluster Radius (Å)	# water molecules	TIP3P dipole moment (D)
4.0	11	1.97
4.1	11	1.97
4.2	21	6.56
4.3	21	6.56
4.4	21	6.56
4.5	21	6.56
4.6	21	6.56
4.7	21	6.56
4.8	21	6.56
4.9	21	6.56
5.0	21	6.56

Cluster Radius (Å)	# water molecules	TIP3P dipole moment (D)
5.0	21	6.56
5.1	21	6.56
5.2	23	2.29
5.3	23	2.29
5.4	25	1.98
5.5	25	1.98
5.6	25	1.98
5.7	25	1.98
5.8	25	1.98
5.9	29	6.56
6.0	29	6.56

Cluster Radius (Å)	# water molecules	TIP3P dipole moment (D)
6.0	29	6.56
6.1	29	6.56
6.2	33	6.56
6.3	35	6.55
6.4	45	15.69
6.5	45	15.69
6.6	47	15.67
6.7	59	10.78
6.8	63	1.93
6.9	63	1.93
7.0	65	1.94

Cluster Radius (Å)	# water molecules	TIP3P dipole moment (D)
7.0	65	1.94
7.1	65	1.94
7.2	65	1.94
7.3	69	1.97
7.4	69	1.97
7.5	69	1.97
7.6	73	2.00
7.7	73	2.00
7.8	83	2.25
7.9	87	6.30
8.0	89	2.02

Table 5-2 TIP3P dipole moments vs. the radius size of the clusters for the oxygen site 2 of the ice IX structure

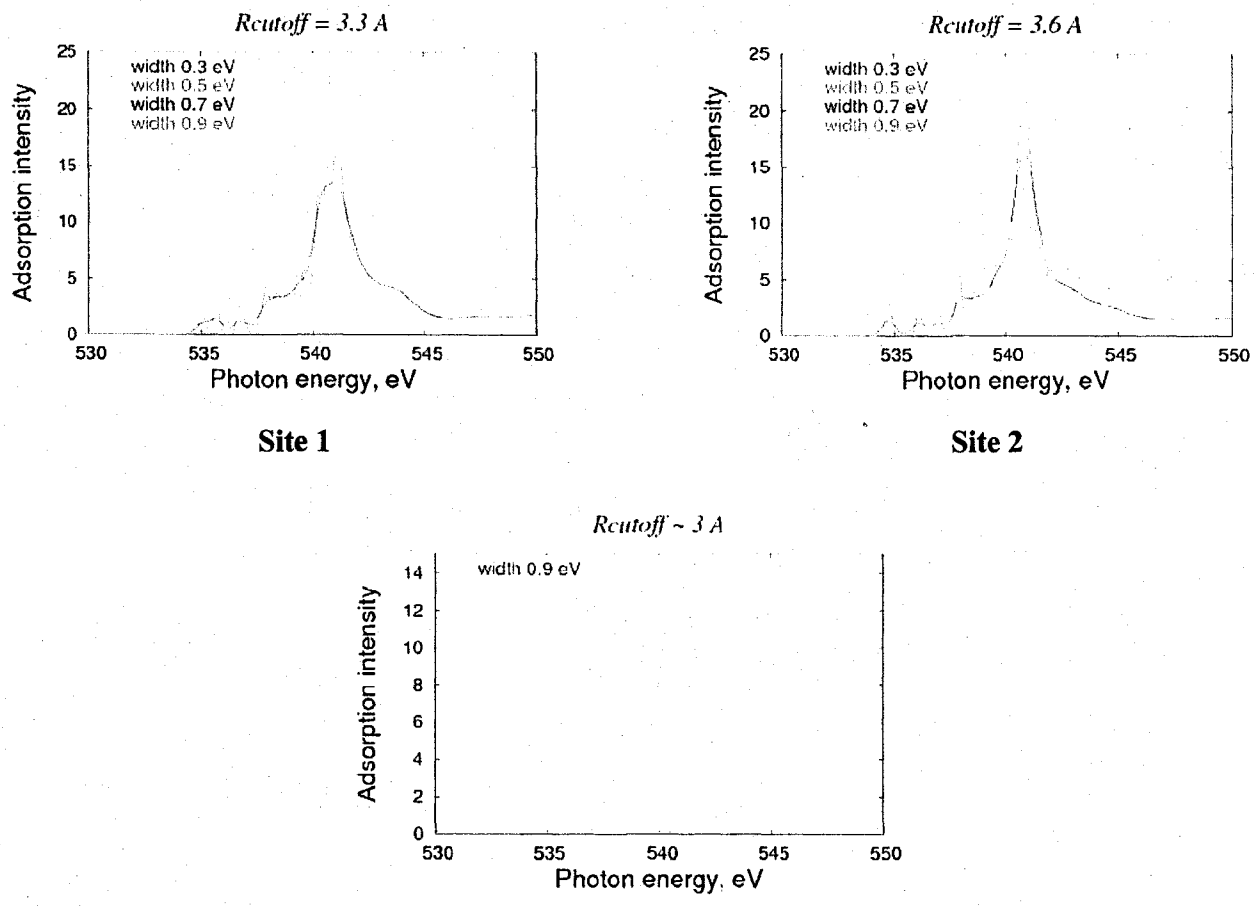

Figure 5-4 XAS of ice IX. Quantum cluster ~3 Å radius without point charges

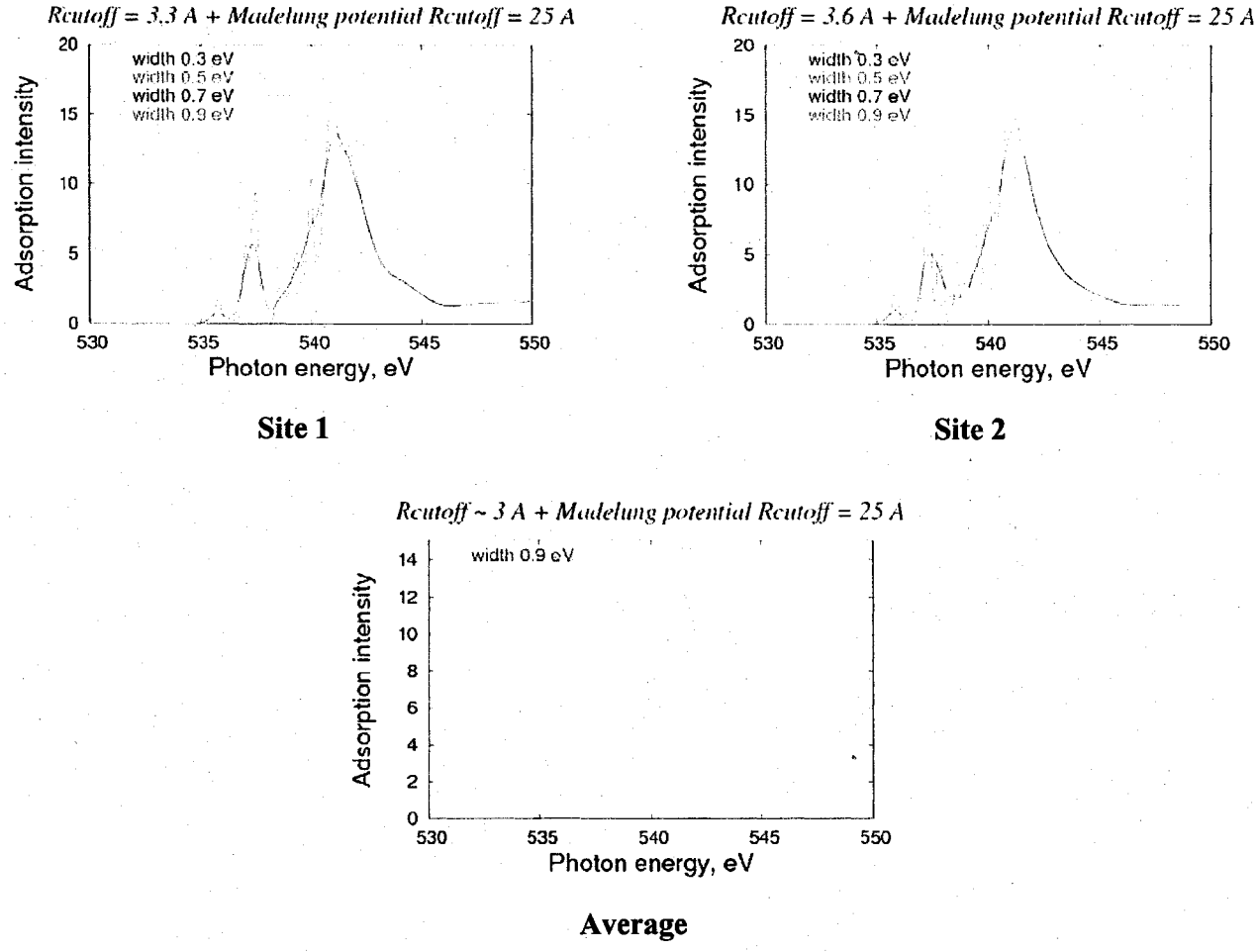

Figure 5-5 XAS of ice IX. Quantum cluster ~3 Å radius with point charges 25 Å radius

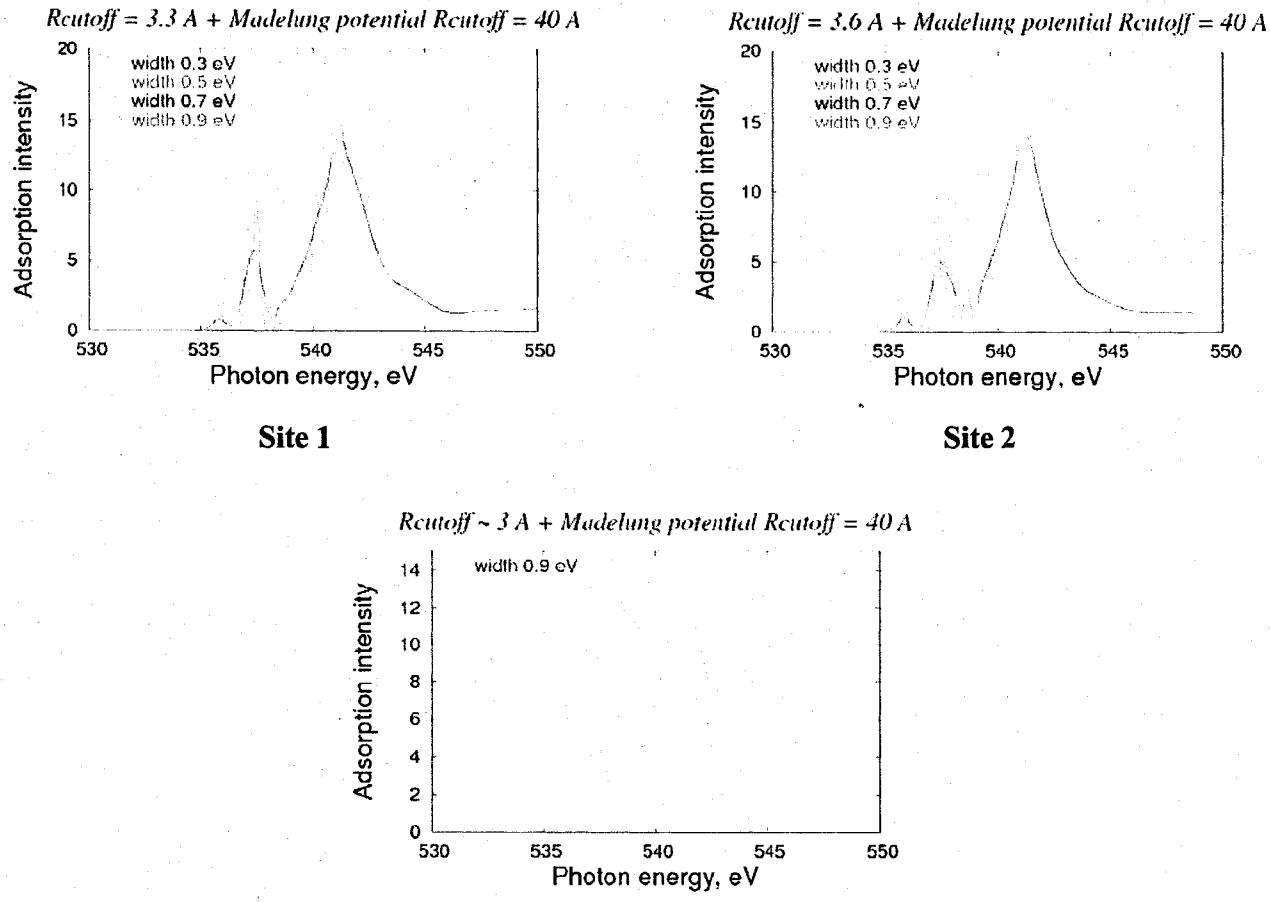

Figure 5-6 XAS of ice IX. Quantum cluster ~3 Å radius with point charges 40 Å radius

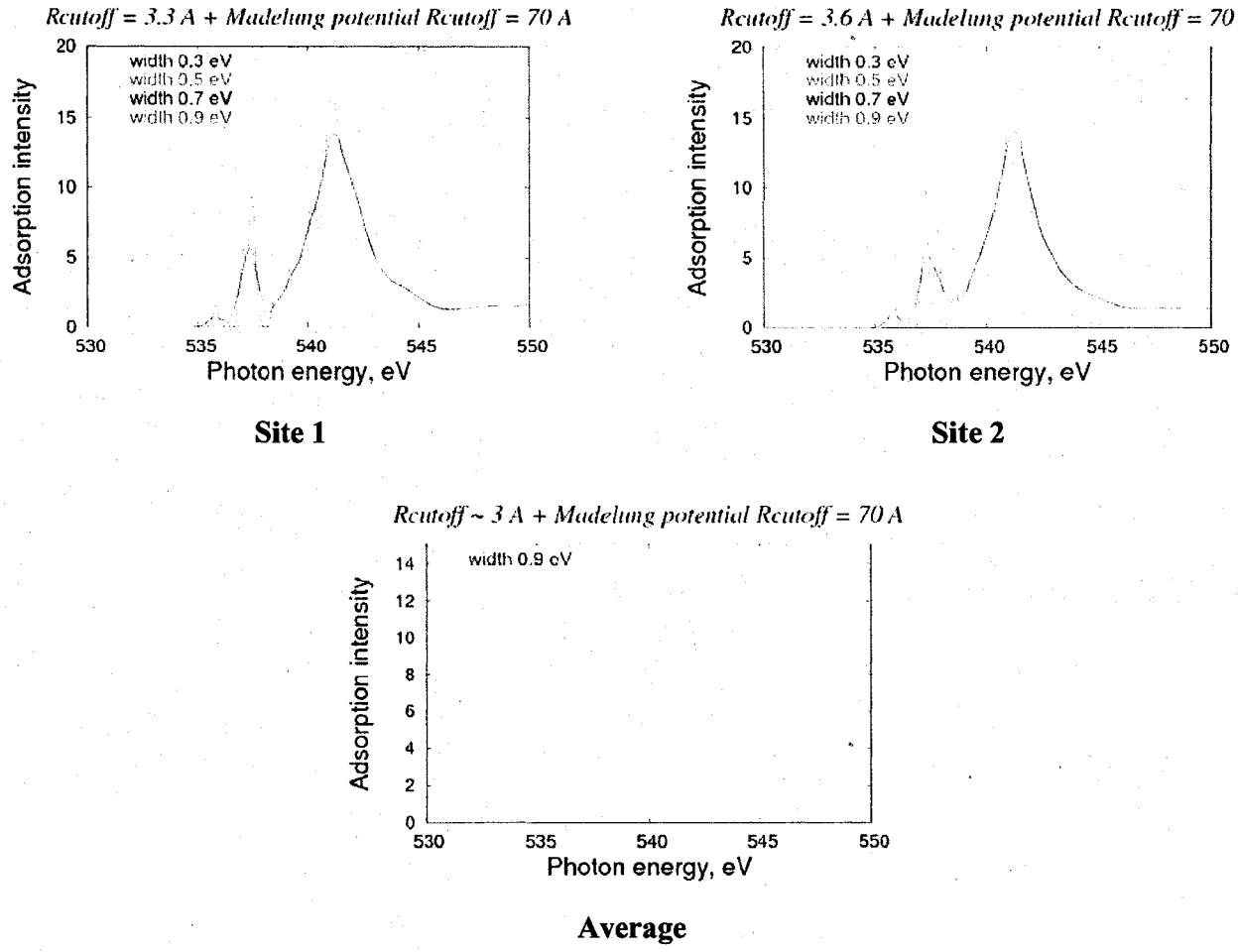

Figure 5-7 XAS of ice IX. Quantum cluster ~3 Å radius with point charges 70 Å radius

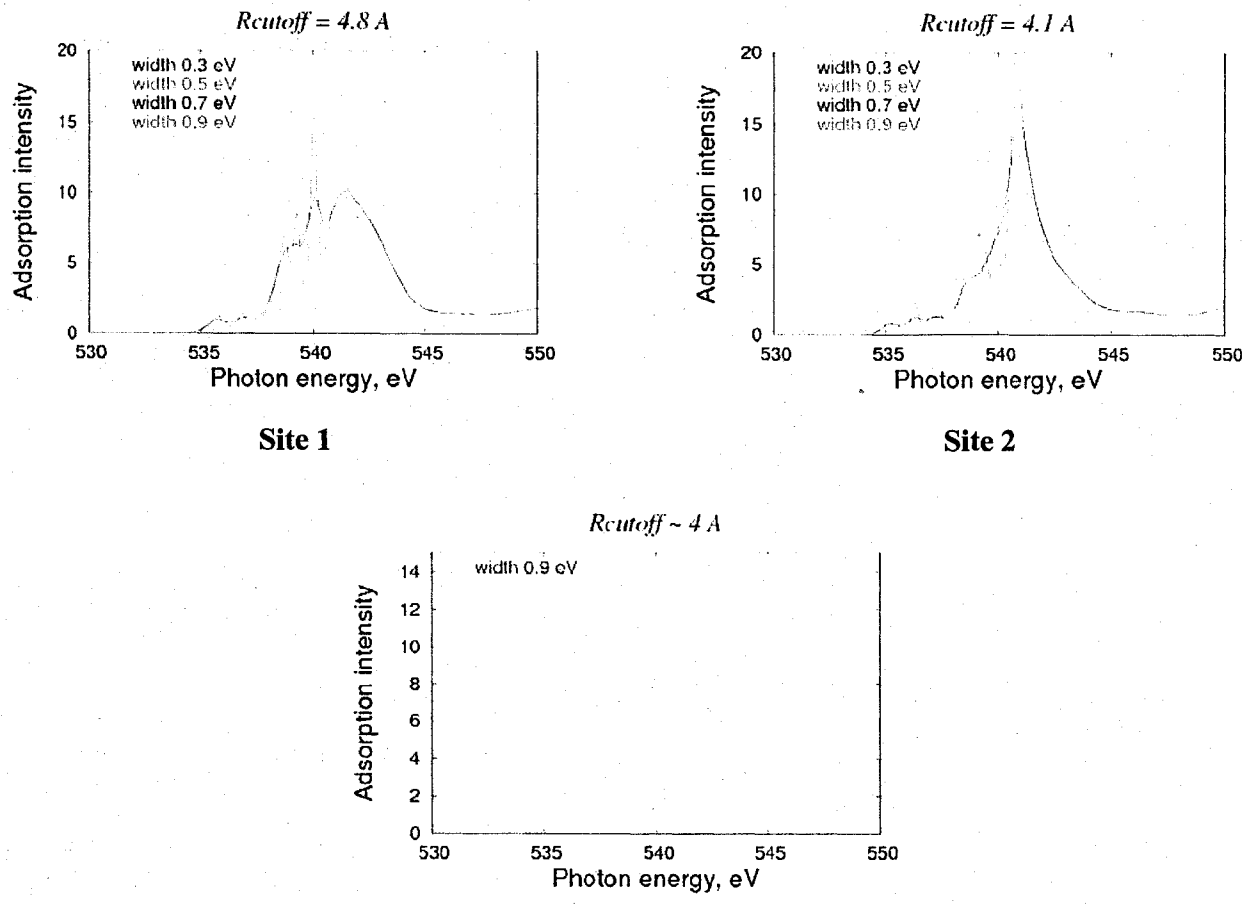

Figure 5-8 XAS of ice IX. Quantum cluster ~4 Å radius without point charges

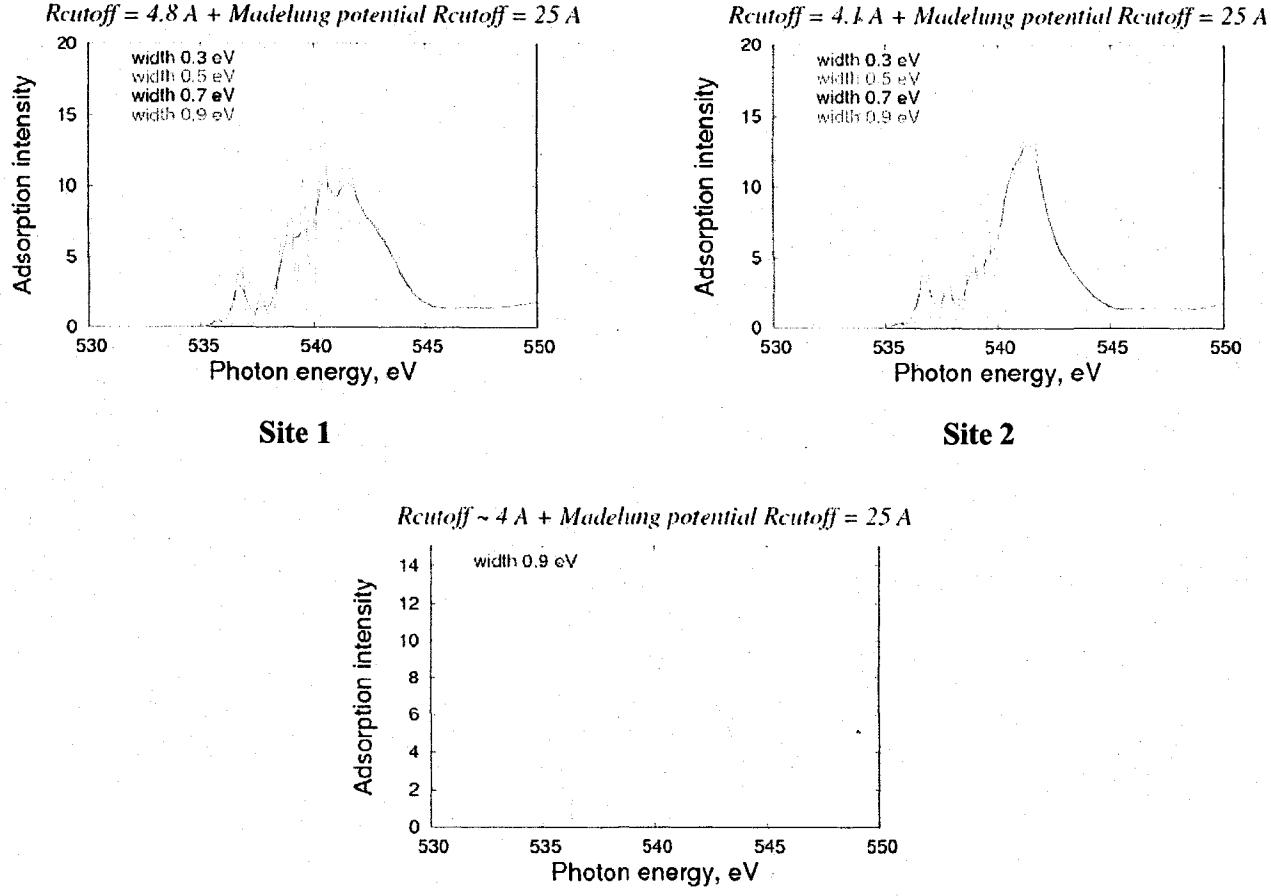

Figure 5-9 XAS of ice IX. Quantum cluster ~4 Å radius with point charges 25 Å radius

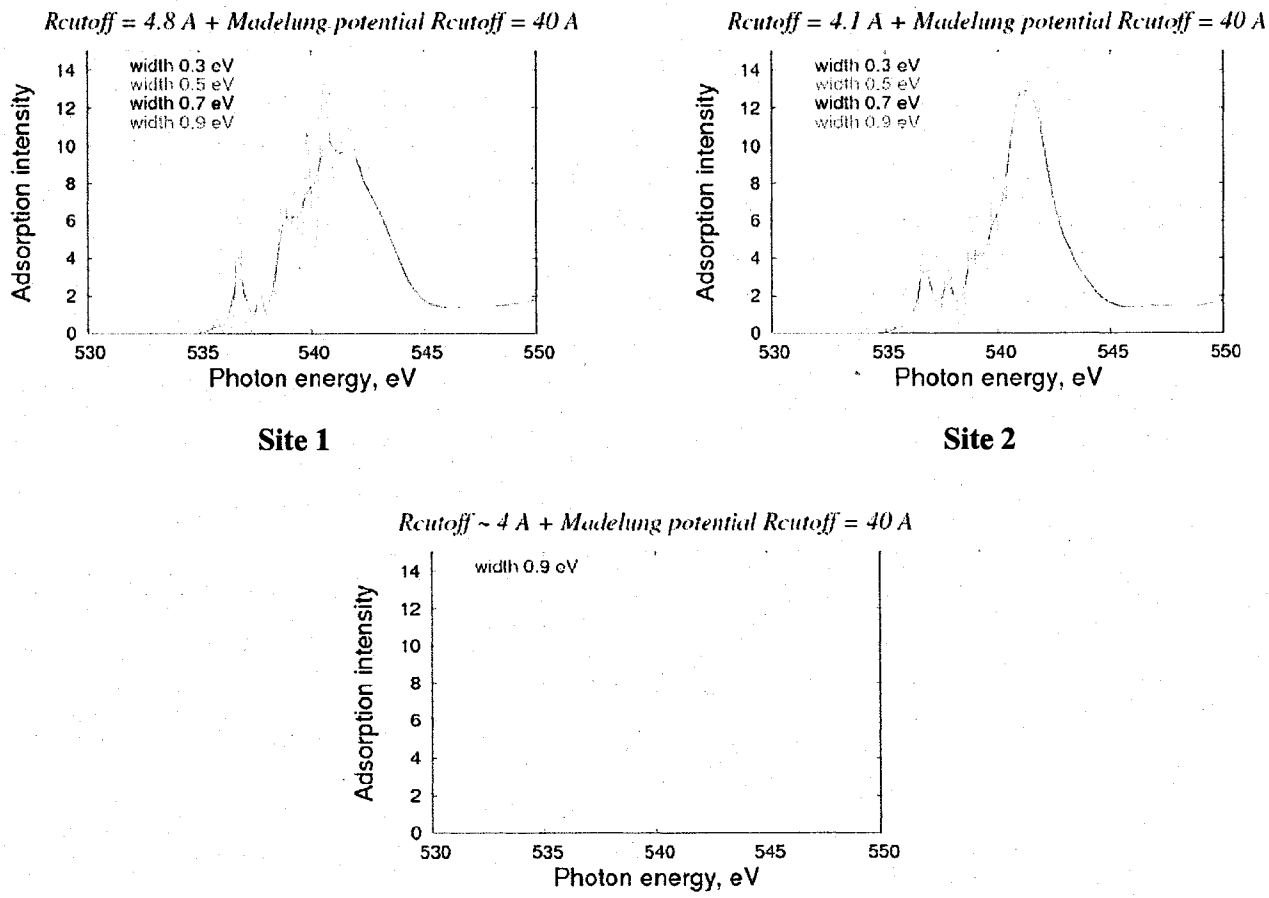

Figure 5-10 XAS of ice IX. Quantum cluster ~4 Å radius with point charges 40 Å radius

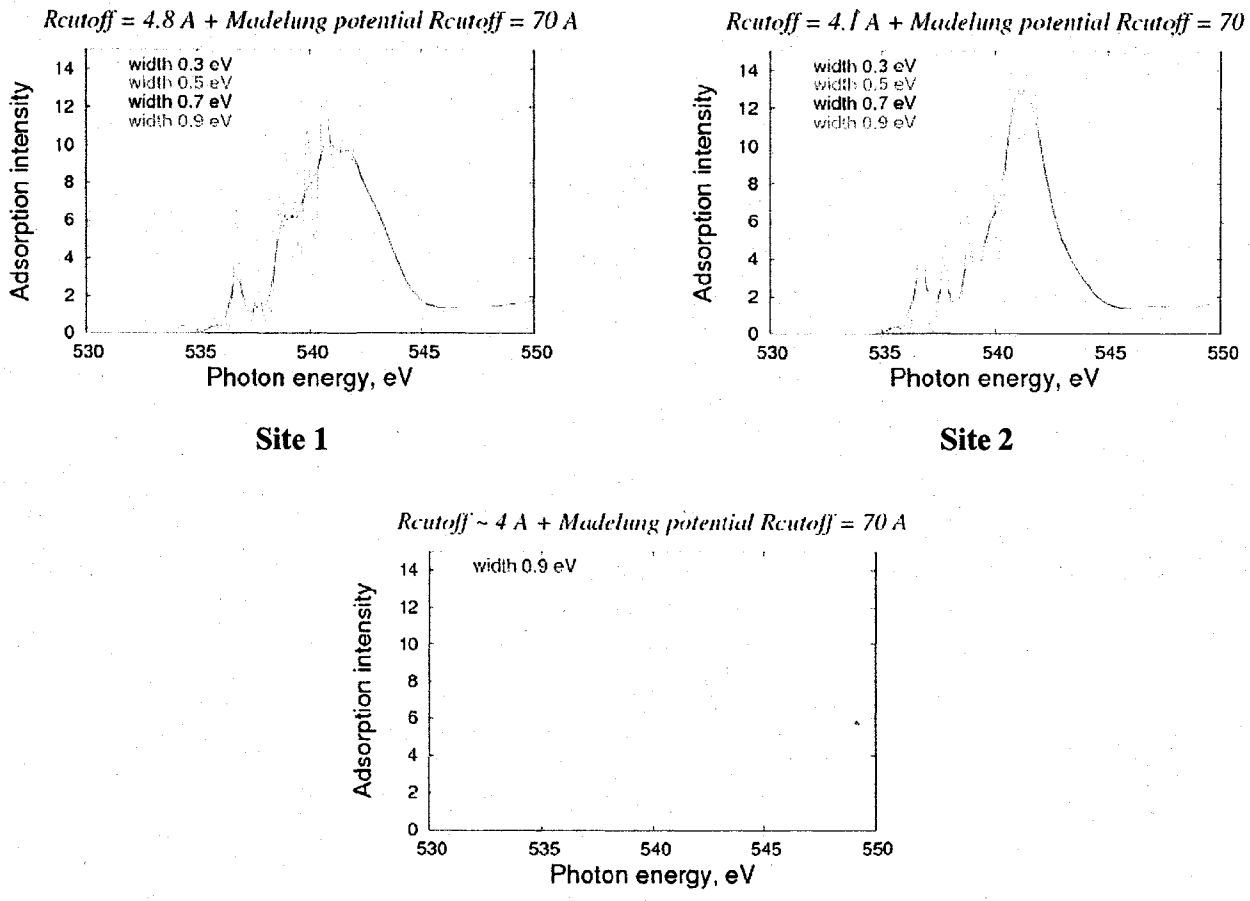

Figure 5-11 XAS of ice IX. Quantum cluster ~4 Å radius with point charges 70 Å radius

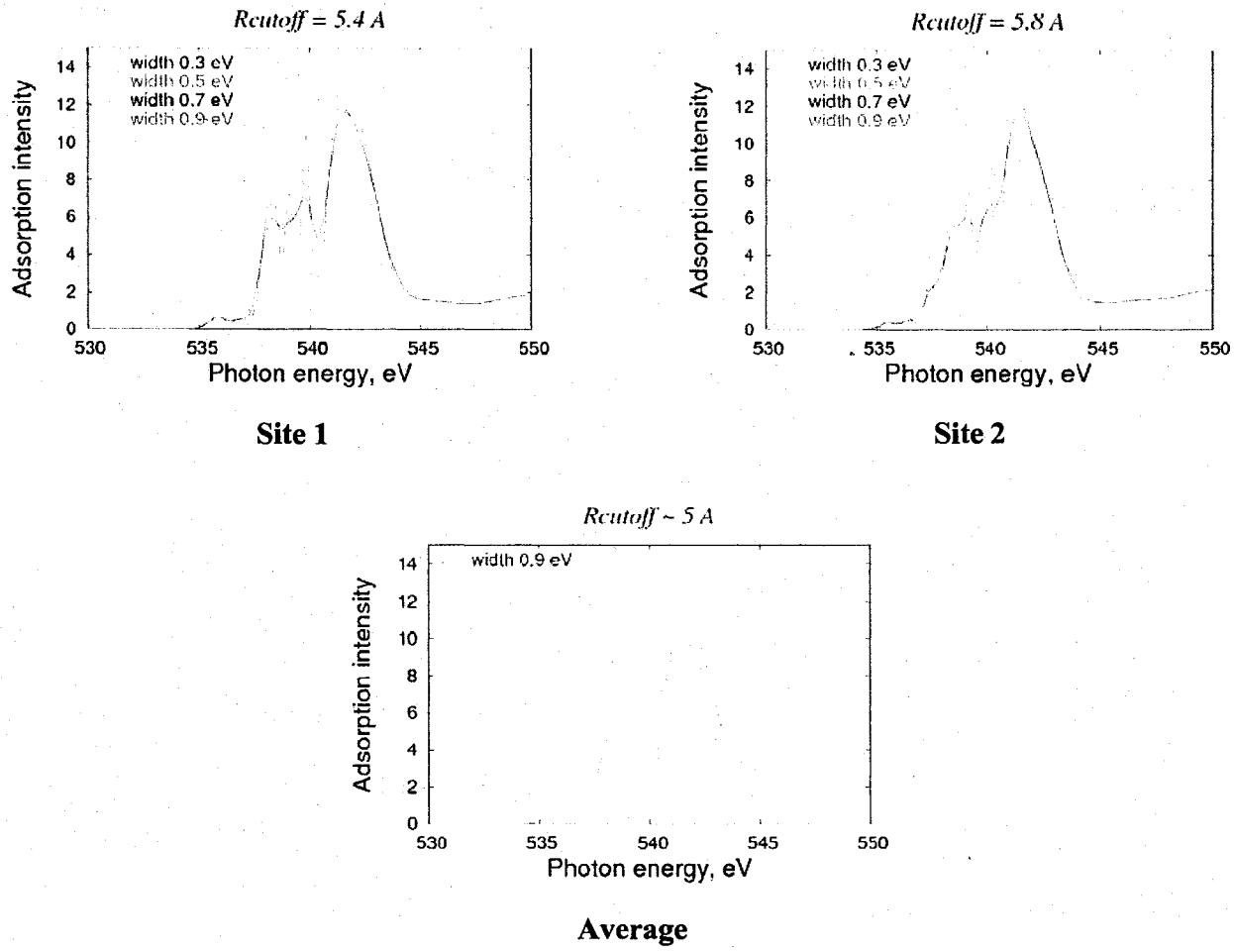

Figure 5-12 XAS of ice IX. Quantum cluster ~5 Å radius without point charges

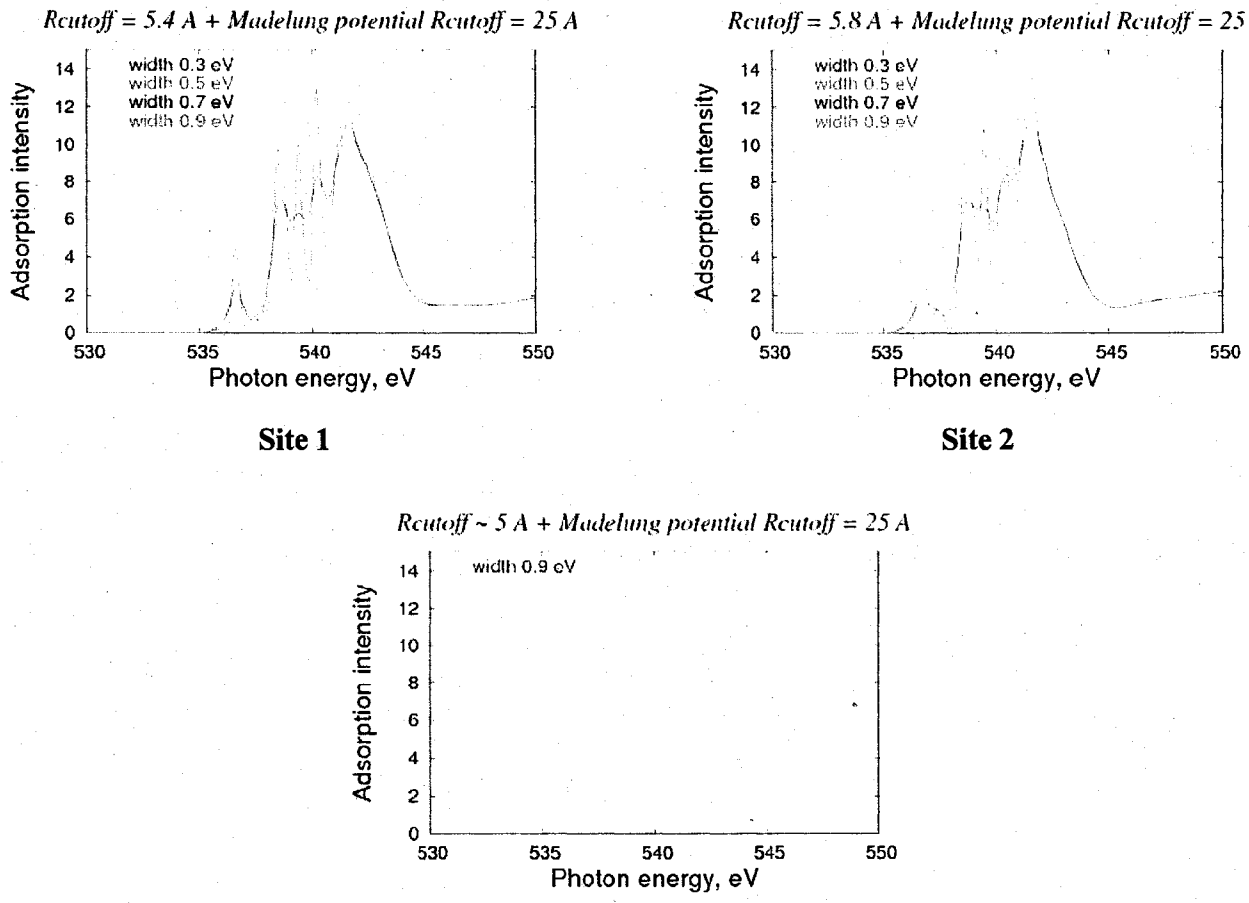

Figure 5-13 XAS of ice IX. Quantum cluster ~5 Å radius with point charges 25 Å radius

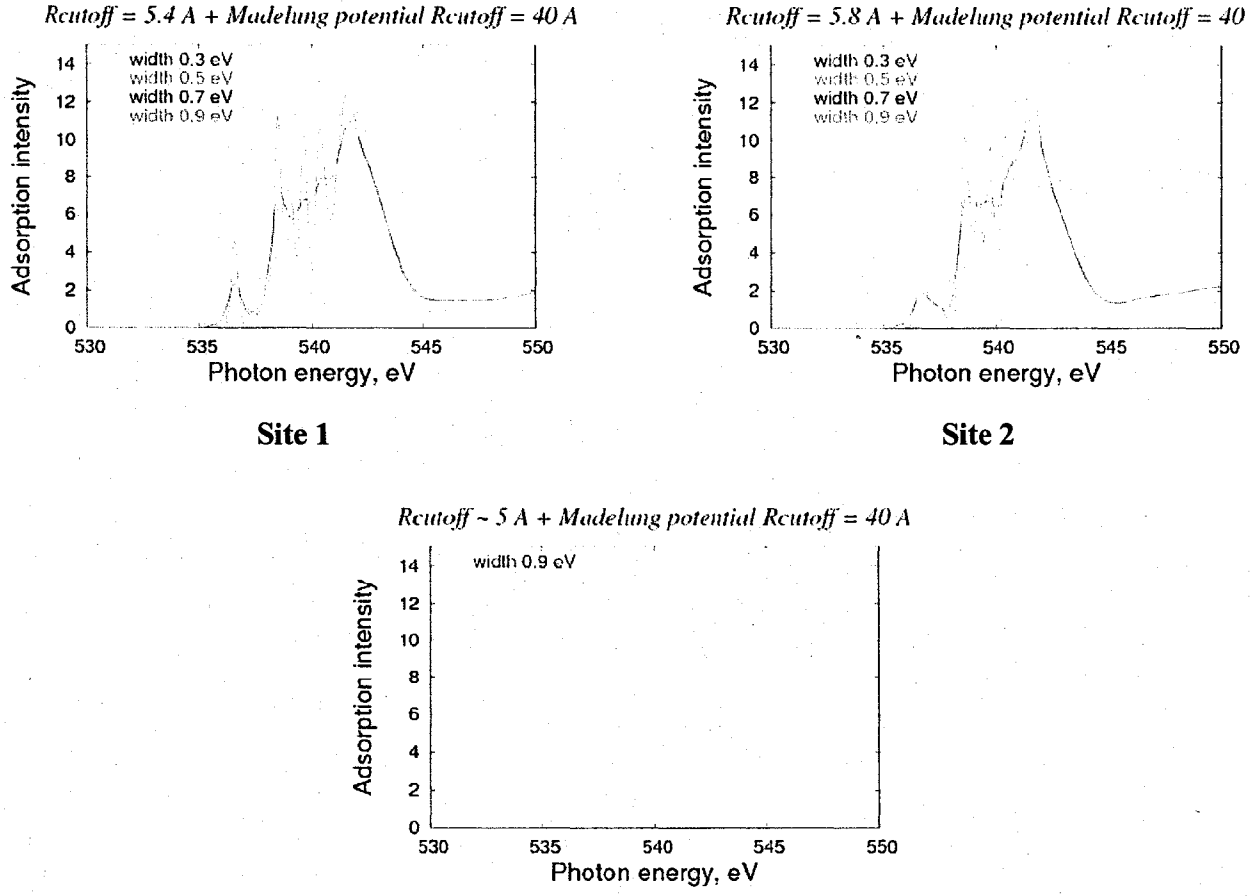

Figure 5-14 XAS of ice IX. Quantum cluster ~5 Å radius with point charges 40 Å radius

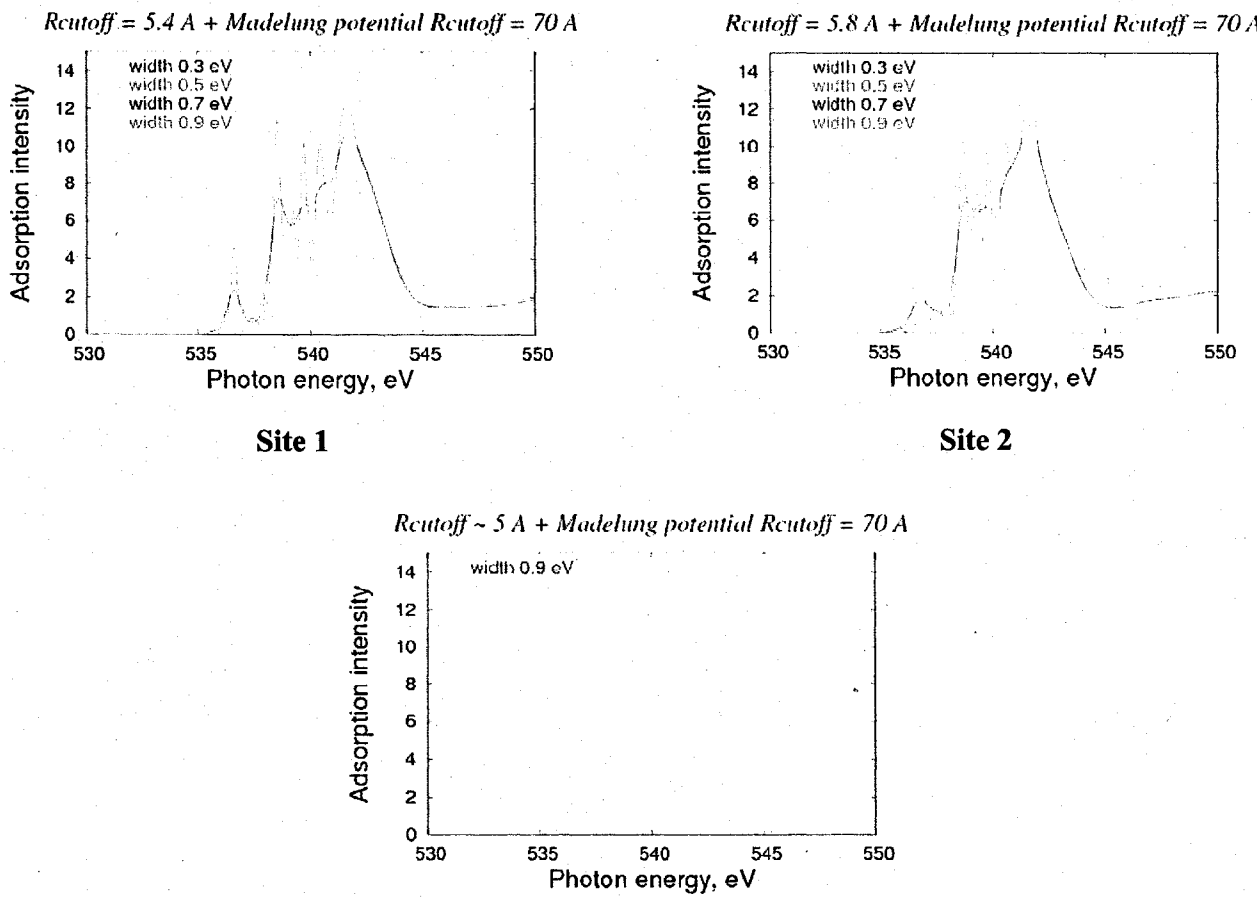

Figure 5-15 XAS of ice IX. Quantum cluster ~5 Å radius with point charges 70 Å radius

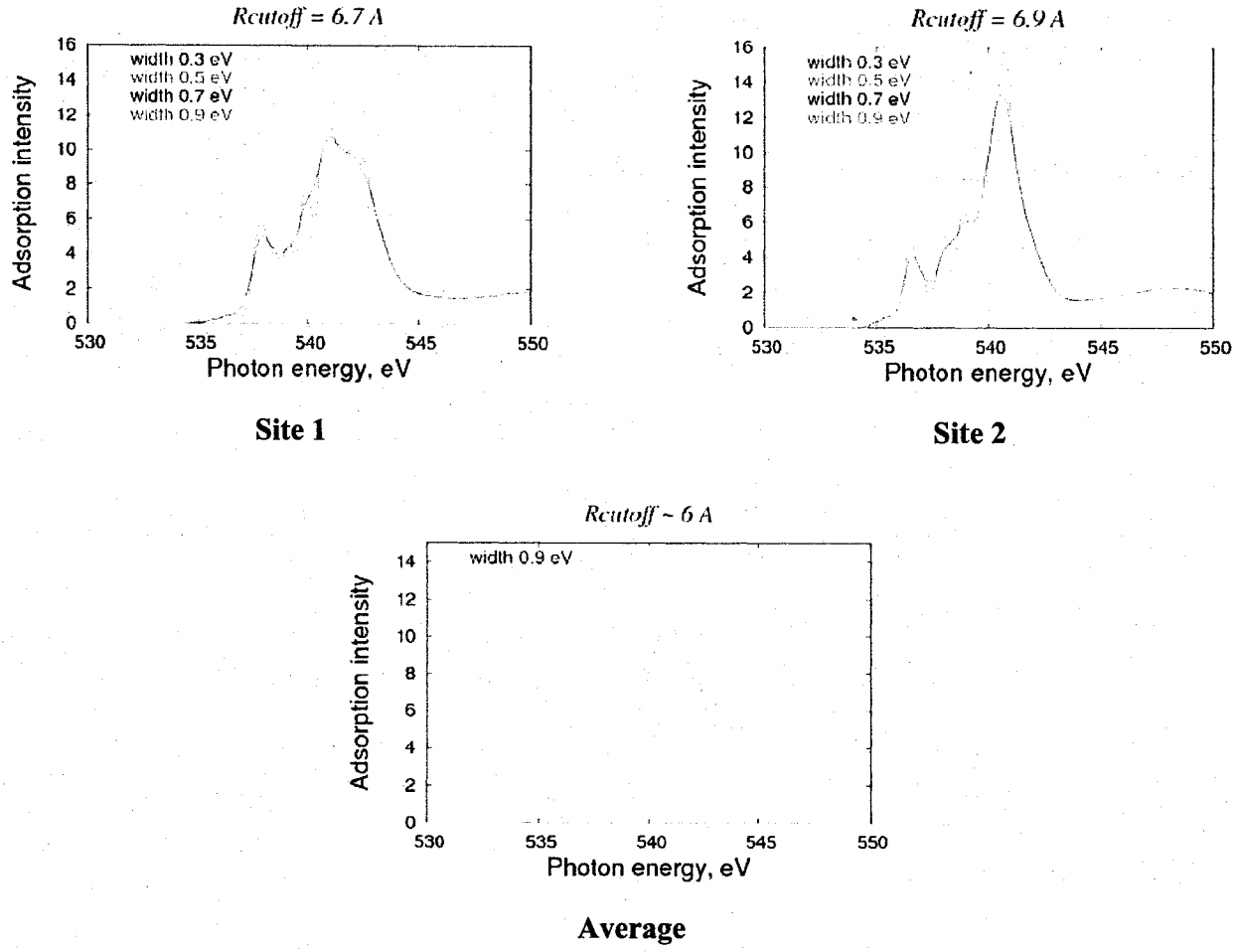

Figure 5-16 XAS of ice IX. Quantum cluster ~6 Å radius without point charges

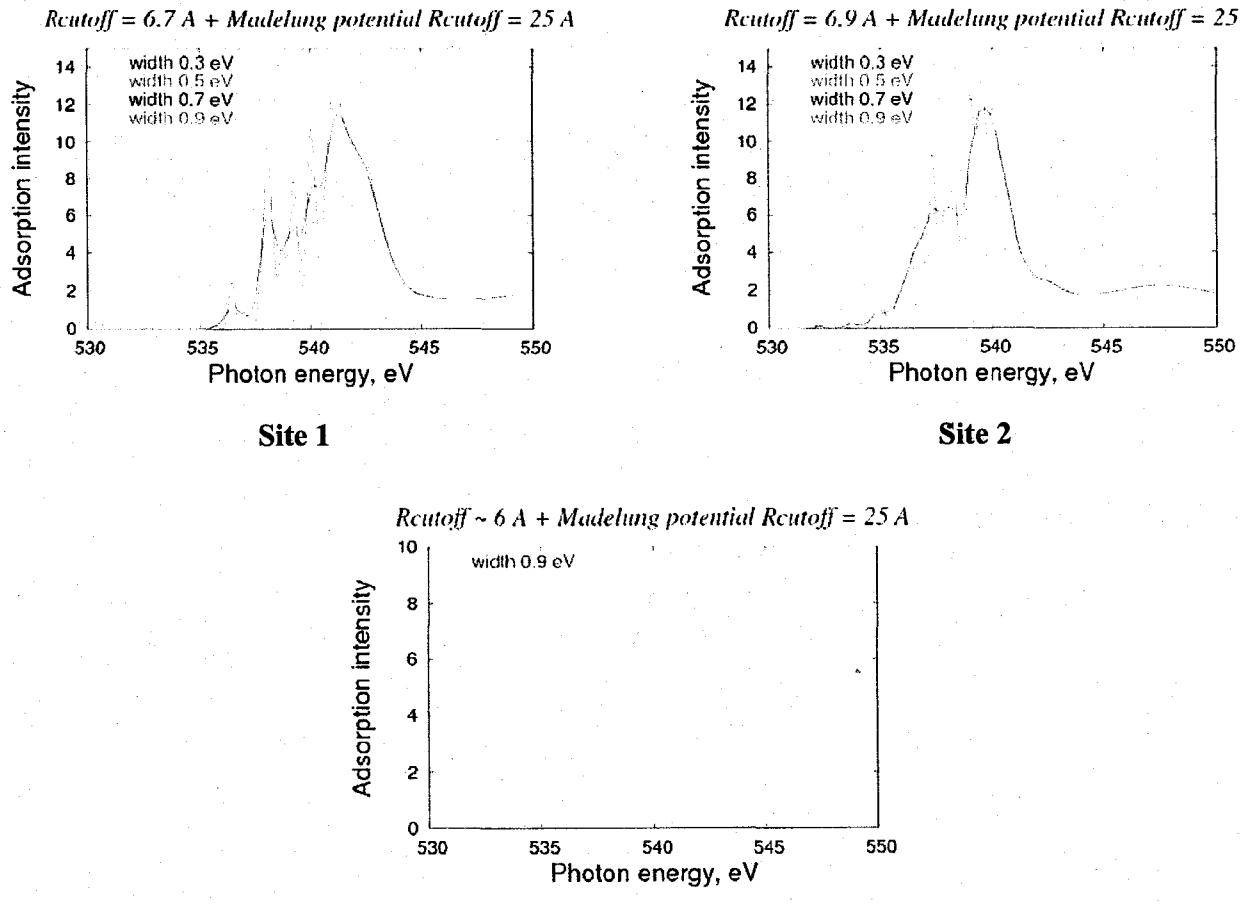

Figure 5-17 XAS of ice IX. Quantum cluster ~6 Å radius with point charges 25 Å radius

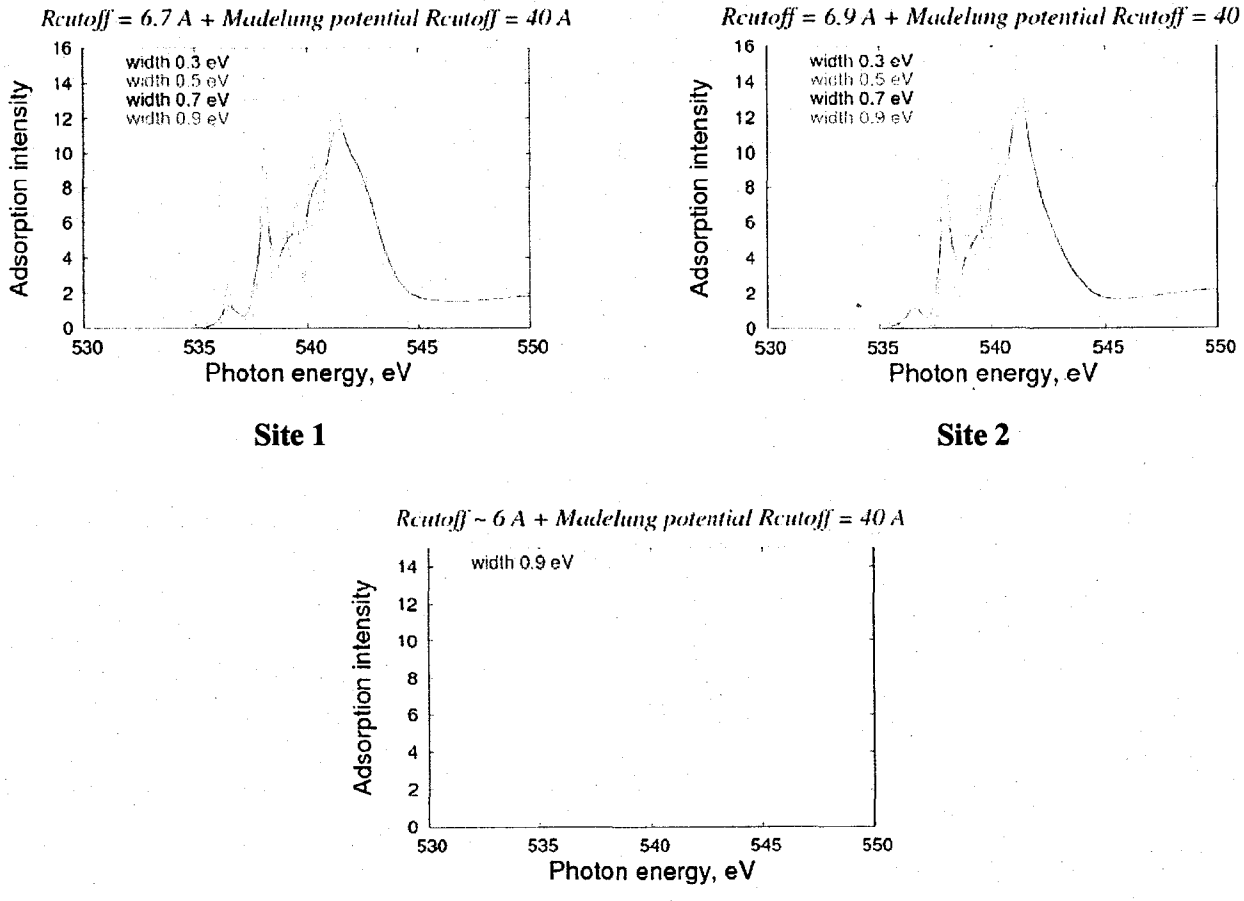

Figure 5-18 XAS of ice IX. Quantum cluster ~6 Å radius with point charges 40 Å radius

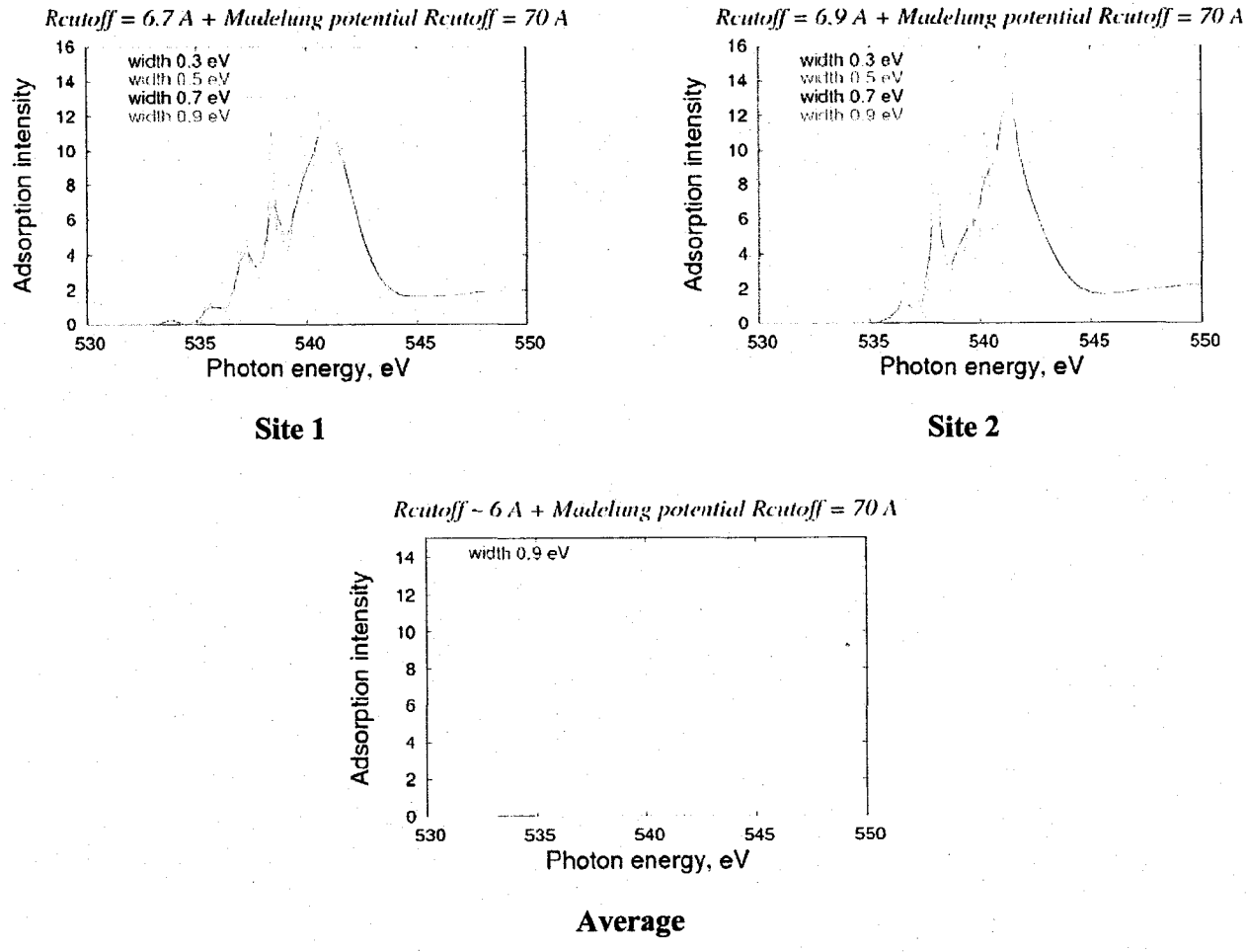

Figure 5-19 XAS of ice IX. Quantum cluster ~6 Å radius with point charges 70 Å radius

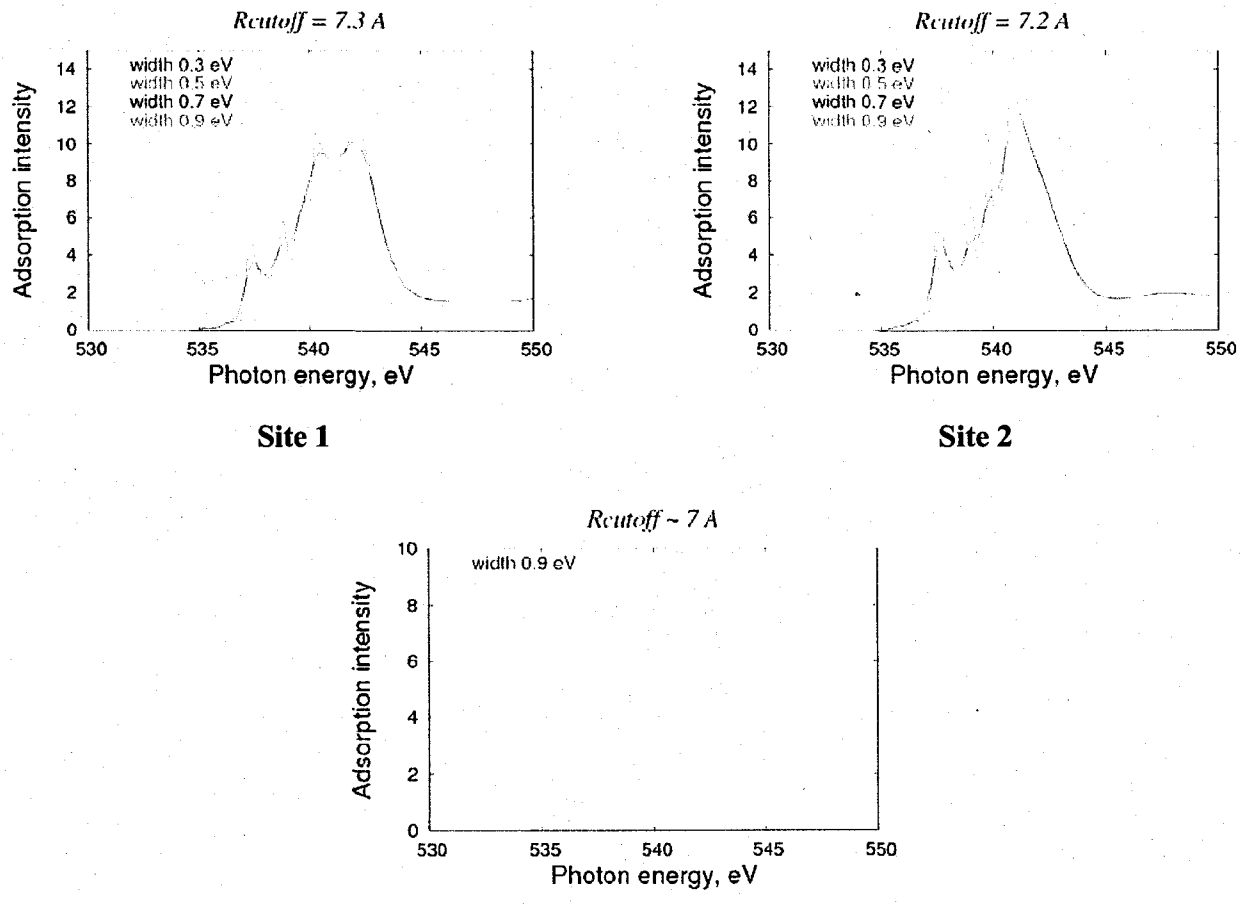

Figure 5-20 XAS of ice IX. Quantum cluster ~7 Å radius without point charges

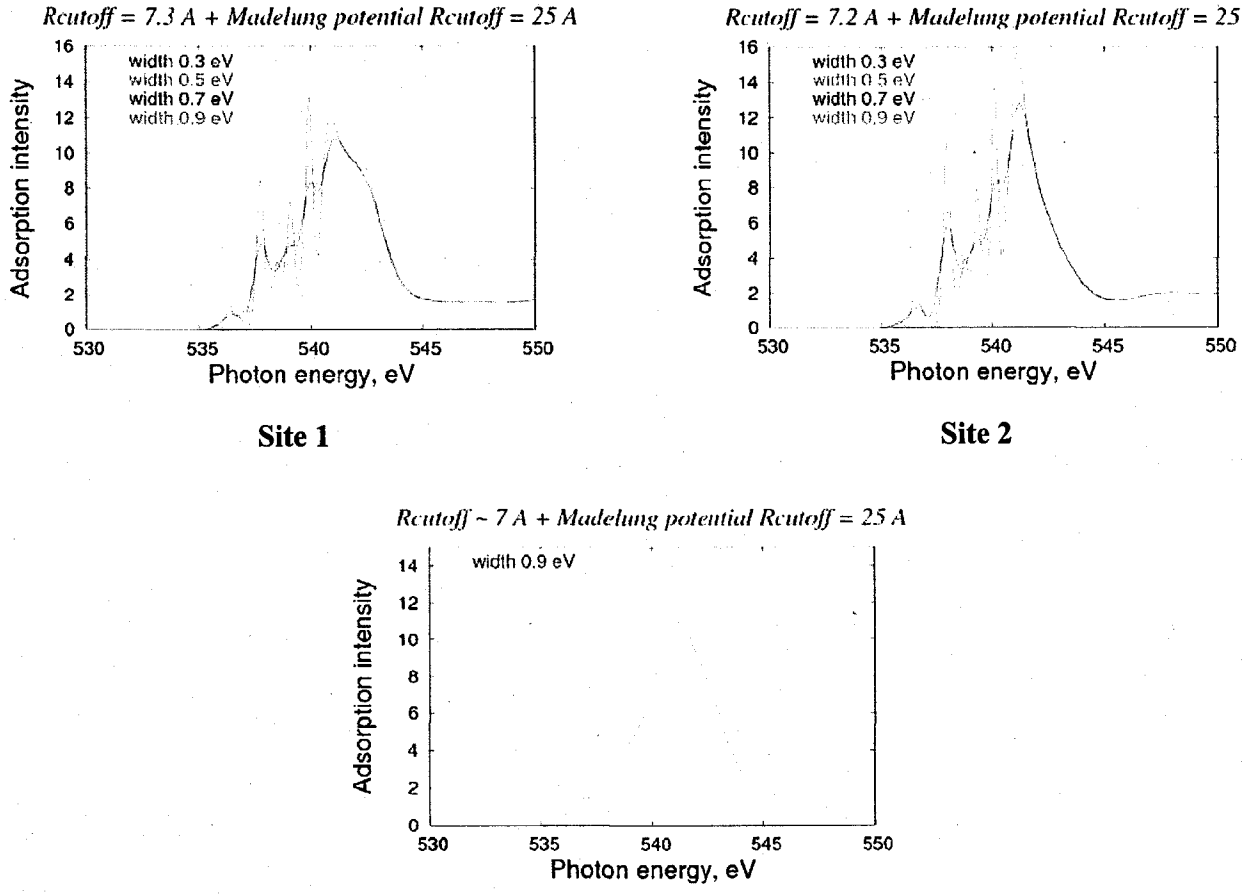

Figure 5-21 XAS of ice IX. Quantum cluster ~7 Å radius with point charges 25 Å radius

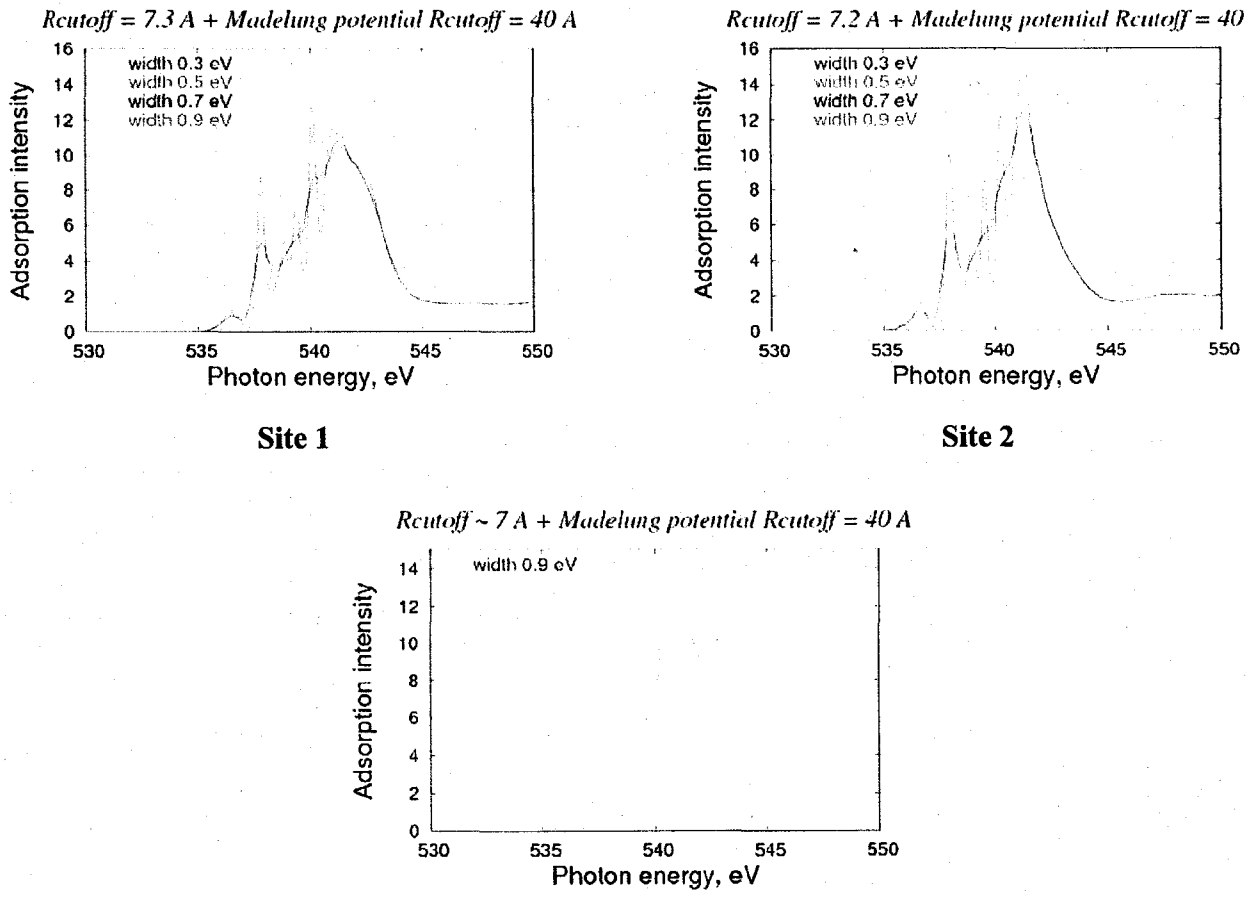

Figure 5-22 XAS of ice IX. Quantum cluster ~7 Å radius with point charges 40 Å radius

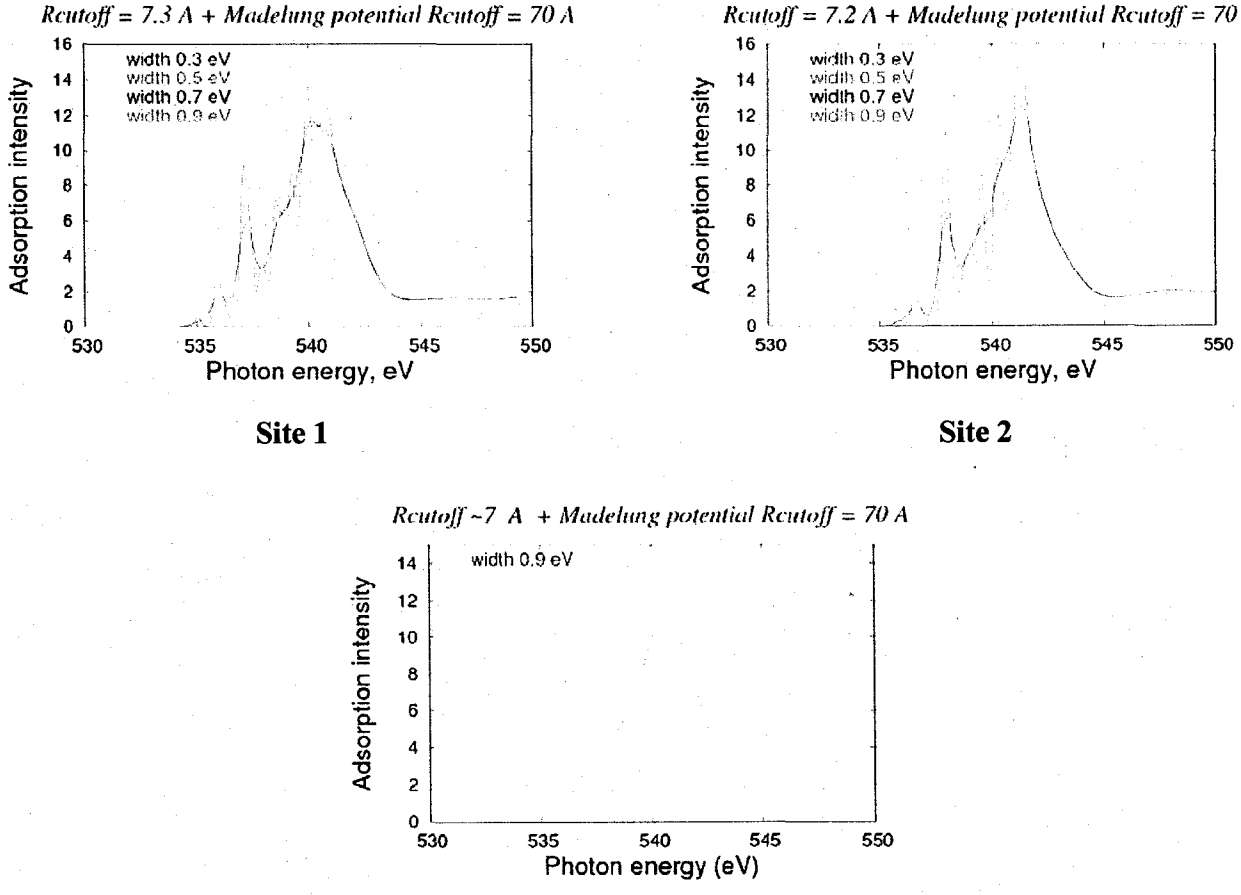

Figure 5-23 XAS of ice IX. Quantum cluster ~7 Å radius with point charges 70 Å radius

5.3.2 Ice VIII

For the ice VIII structure, the values in Equation 5-7 were chosen to be R_0=40 and D=4. The spectra were calculated from the only crystallographically unique oxygen in the structure. All the clusters should provide essentially the same spectrum. Therefore, in order to save CPU time, the results are only presented for the smallest cluster with the smallest dipole moment, i.e., a 7.11 A radius. Spectra were also calculated for the other two clusters of radii 7.25 and 7.32 Å with the small dipole moments, but with a smaller Madelung potential.

The calculated ionization potential is 537.80 eV.

Cluster Radius (Å)	*# water molecules*	*TIP3P dipole moment (D)*
7.0	65	11.72
7.1	65	11.72
7.11	69	2.36
7.19	75	7.03
7.2	75	7.03
7.25	77	2.36
7.28	85	21.26
7.3	89	11.72
7.32	93	2.36
7.37	101	16.41
7.4	101	16.41
7.45	105	25.79
7.5	105	25.79
7.52	109	35.17
7.6	109	35.17
7.7	109	35.17
7.76	113	44.55
7.8	113	44.55
7.9	113	44.55
8.0	113	44.55

Table 5-3 TIP3P dipole moments vs. the radius size of the clusters for the ice VIII structure

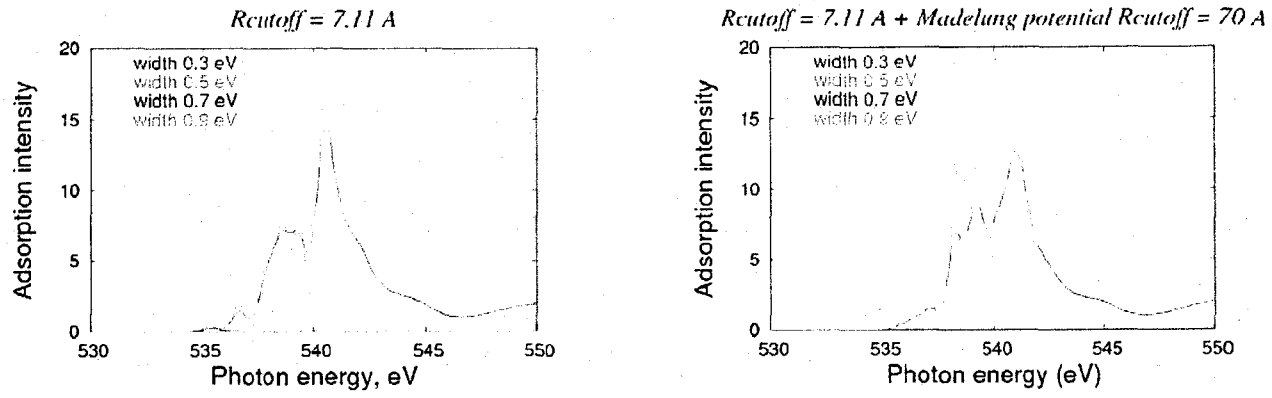

Figure 5-24 XAS of ice VIII. Quantum cluster 7.11 Å radius without point charges and with point charges 70 Å radius.

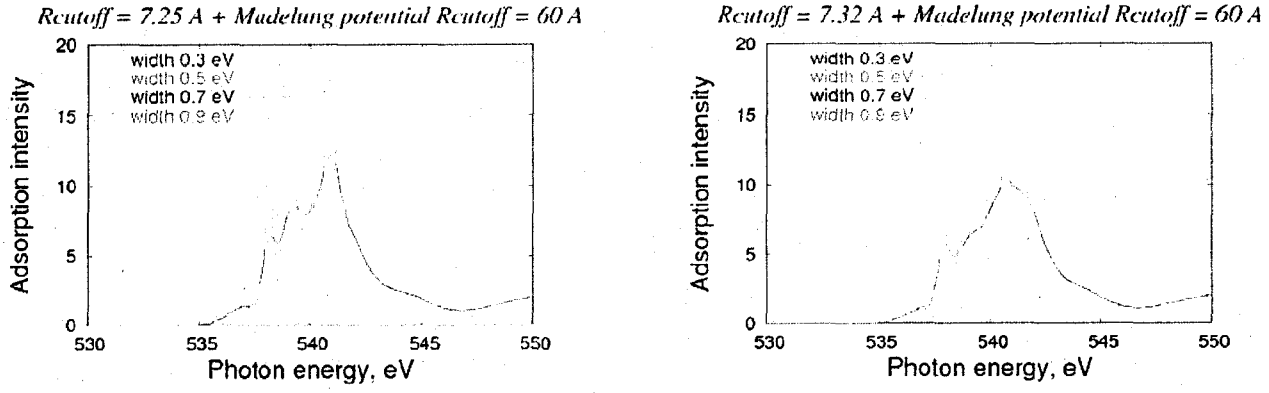

Figure 5-25 XAS of ice VIII. Quantum clusters 7.25 Å and 7.32 Å radius with point charges 60 Å radius.

5.3.3 Ice II

For the ice II structure, the values in Equation 5-7 were chosen to be R_0=40 and D=4. The spectra were calculated for each crystallographically non-equivalent oxygen and the average spectrum was calculated by averaging the transition intensities for each transition energy, considering that in the case of ice II, there are as many sites 1 as there are sites 2. The radius chosen for site 1 is 7.65 Å and the one for site 2 is 7.99 Å.

The calculated ionization potential for site 1 is 537.81 eV and 537.86 eV for site 2.

Cluster Radius (Å)	*# water molecules*	*TIP3P dipole moment (D)*
7.0	56	12.71
7.07	57	10.32
7.1	58	7.94
7.13	61	8.72
7.17	63	7.93
7.18	65	8.72
7.2	65	8.72
7.26	67	7.93
7.3	67	7.93
7.4	67	7.93
7.42	68	7.94
7.43	69	10.21
7.48	70	9.87
7.5	70	9.87
7.51	71	10.11
7.56	77	5.23
7.58	79	7.36
7.6	79	7.36
7.64	80	5.64
7.65	84	2.59
7.67	85	4.64
7.7	85	4.64
7.71	87	7.45
7.77	88	7.97
7.78	89	9.22
7.8	89	9.22
7.9	89	9.22
7.91	90	7.52
7.92	91	6.29
7.96	92	8.11
7.97	93	6.29
7.99	94	4.74
8.0	94	4.74

Cluster Radius (Å)	*# water molecules*	*TIP3P dipole moment (D)*
7.0	60	12.65
7.02	62	11.96
7.07	63	9.51
7.1	64	7.09
7.13	65	7.87
7.2	65	7.87
7.3	65	7.87
7.4	68	9.63
7.42	69	9.93
7.48	70	9.51
7.5	70	9.51
7.51	71	9.73
7.54	73	9.67
7.56	79	7.10
7.6	79	7.10
7.67	80	9.13
7.69	84	6.67
7.7	84	6.67
7.71	86	9.44
7.77	87	9.69
7.78	88	10.68
7.8	88	10.68
7.9	88	10.68
7.91	89	8.58
7.92	90	6.76
7.93	91	6.33
7.96	92	8.21
7.97	93	6.33
7.99	94	4.70
8.0	94	4.70

Table 5-4 TIP3P dipole moments vs. the radius size of the clusters for the oxygen site 1 (left) and site 2 (right) of the ice II structure

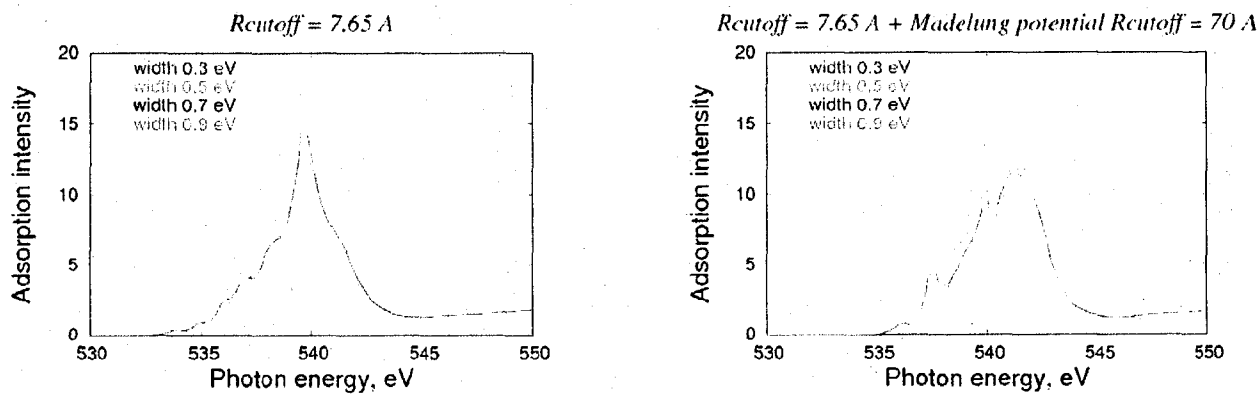

Figure 5-26 XAS of the site 1 of ice II. Quantum cluster 7.65 Å radius without point charges and with point charges 70 Å radius

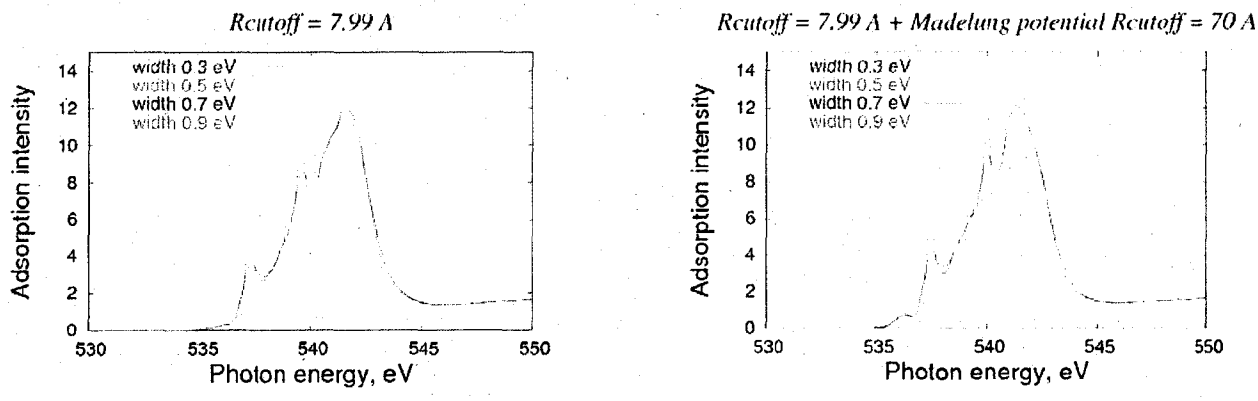

Figure 5-27 XAS of the site 2 of ice II. Quantum cluster 7.99 Å radius without point charges and with point charges 70 Å radius

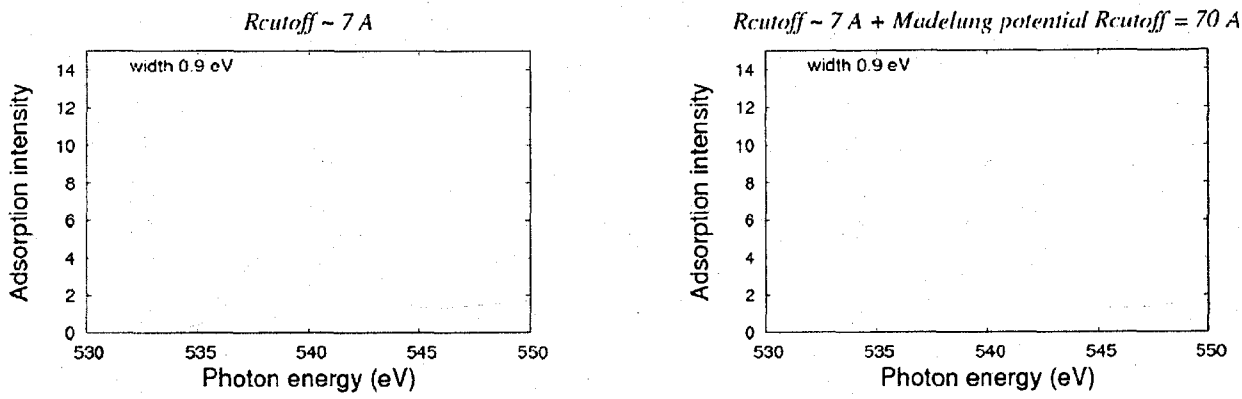

Figure 5-28 Average XAS spectrum of ice II. Quantum cluster ~7 Å radius without point charges and with point charges 70 Å radius

5.3.4 Ice XI

For the ice XI structure, the values in the equation 5-7 were chosen to be R_o=40 and D=4. The spectra were calculated for each crystallographically non-equivalent oxygen and the average spectrum was calculated by averaging the transition intensities for each transition energy according to the respective site multiplicity. In the case of ice XI, in view of the large dipole moment existing in this ferroelectric structure, the TIP3P dipole moment on the range between 7 and 8 Å is always large and generally increases with the radius and therefore a cluster of 7.00 Å was chosen (the smallest radius within the usual range) and embedded in a large 80 Å radius Madelung potential.

The calculated ionization potential for site 1 is 538.31 eV and 538.16 eV for site 2.

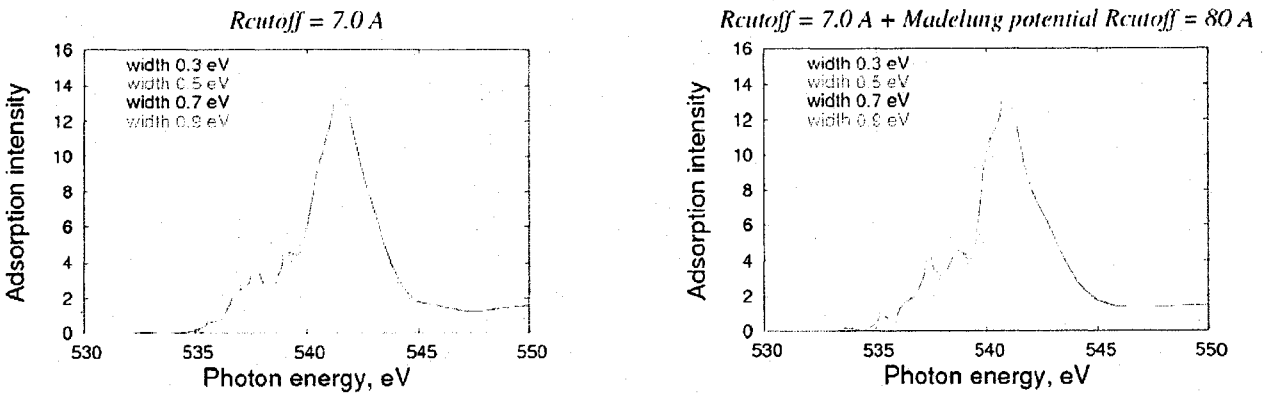

Figure 5-29 XAS of site 1 of ice XI. Quantum cluster 7.00 Å radius without point charges and with point charges 80 Å radius.

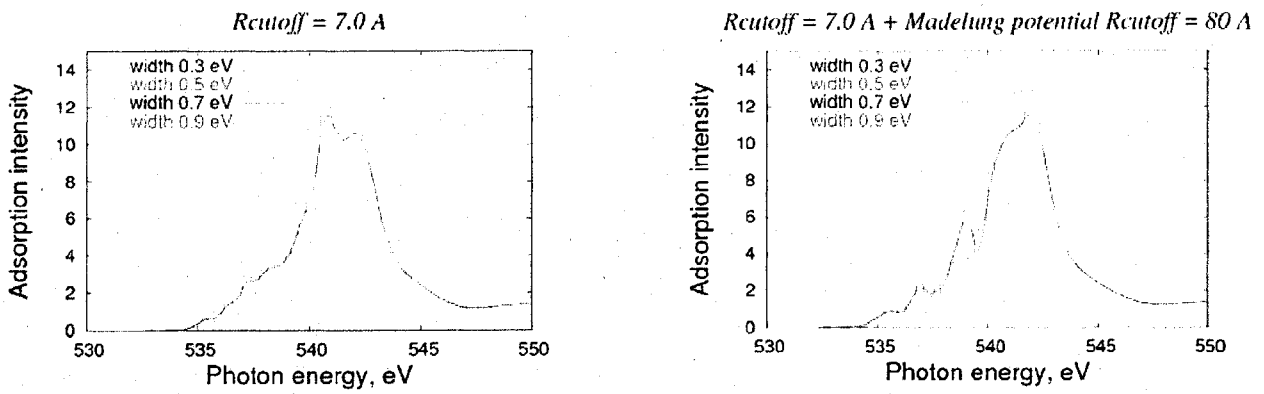

Figure 5-30 XAS of site 2 of ice XI. Quantum cluster 7.00 Å radius without point charges and with point charges 80 Å radius

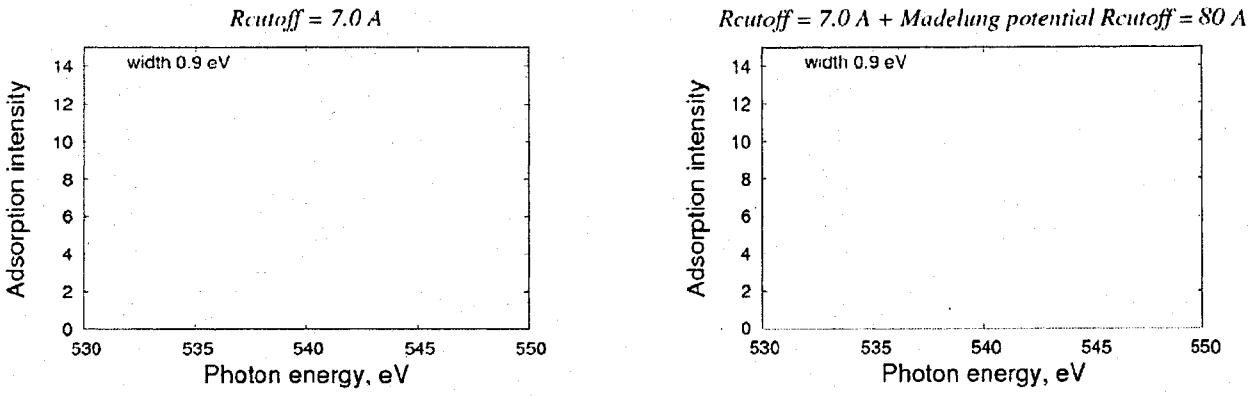

Figure 5-31 Average XAS spectrum of ice XI. Quantum cluster 7.00 Å radius without point charges and with point charges 80 Å radius

5.3.5 Liquid water

In the case of an amorphous structure, such as water, a single calculation cannot represent the average environment of the oxygen atoms observed in an XAS spectrum. Thus, the same procedure as used in the case of the crystalline ices was applied to calculate multiple spectra with central oxygen atoms randomly sampled in the water structure introduced in Chapter 2. Model clusters were chosen between 7 and 8 Å radius to have the smallest TIP3P dipole moment and embedded in a 70 Å radius Madelung potential. Afterwards, those spectra were averaged to produce the final spectra presented here. The averaged spectra were calculated from up to 50 spectra used to generate the average. For the water clusters, the values in the Equation 5-7 were chosen to be R_o=30 and D=8. The convergence was checked by plotting the standard deviation (goes to a constant) and the average variance (goes to zero). The convergence is already reached with 20 different spectra of central oxygen atoms.

The spectra used to generate the averages spectra of water are presented in Appendix 1.

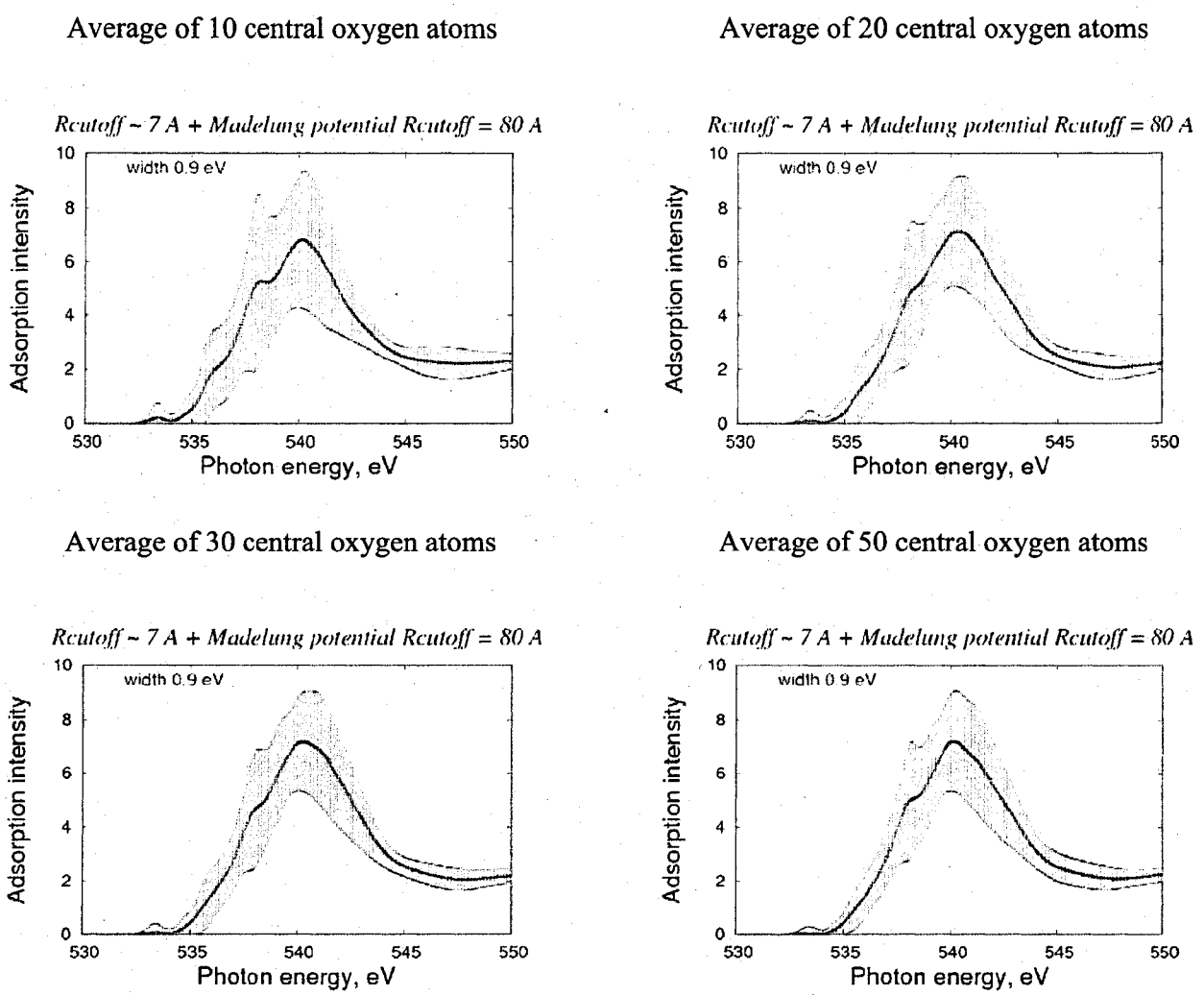

Figure 5-32 Average XAS spectra of water with standard deviation. Quantum cluster 7.00 Å radius with point charges 80 Å radius

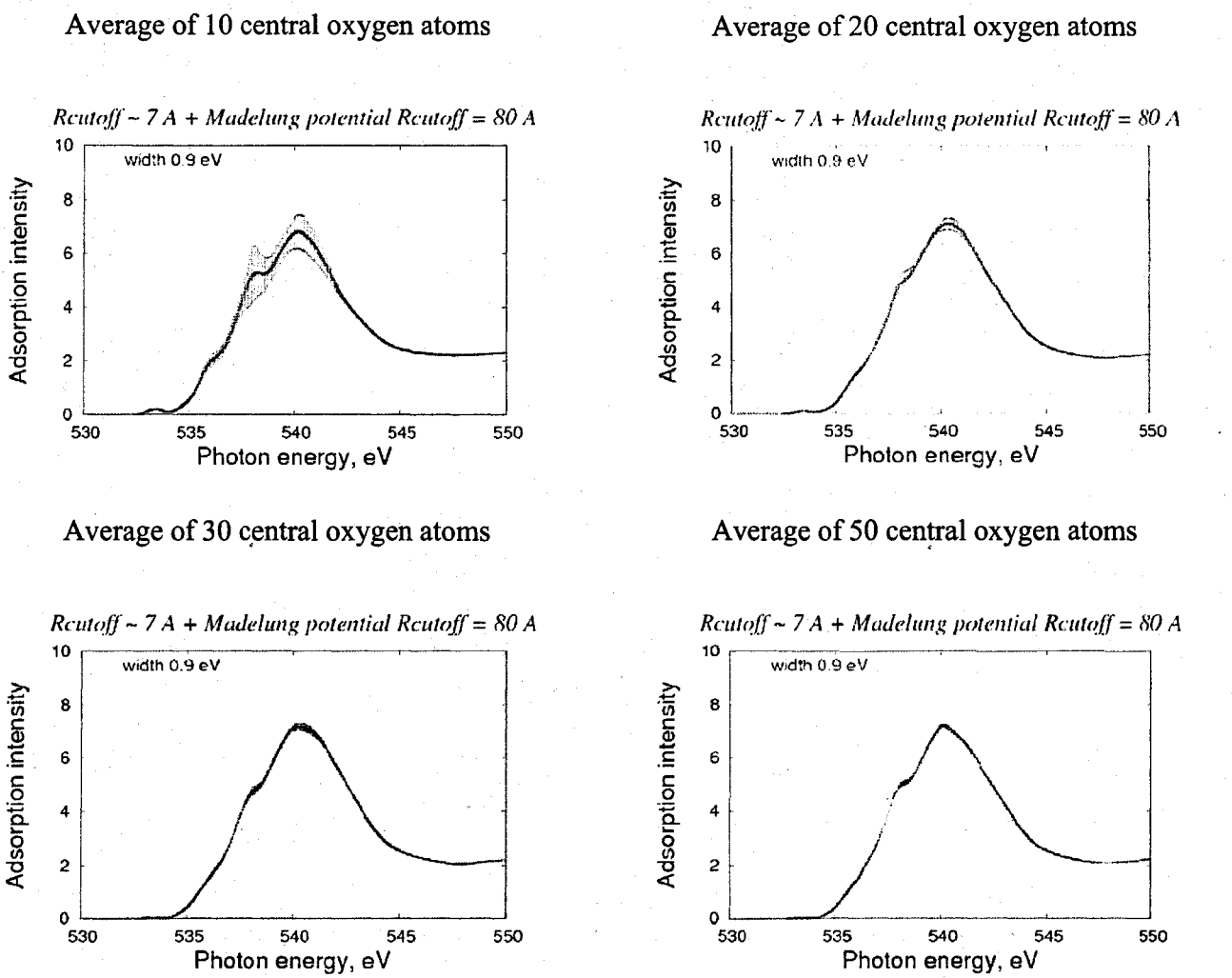

Figure 5-33 Average XAS spectra of water with average variance. Quantum cluster 7.00 Å radius with point charges 80 Å radius

5.3.6 Amorphous ice structures

The last structures to be studied were several amorphous ices. Those configurations were obtained from a run of molecular dynamics that ranged between the low density

structure known as LDA (density at atmospheric pressure of about 0.94 mg m^{-3}) and the high density structure labeled HDA (atmospheric density of about 1.17 mg m^{-3}). Inelastic X-ray scattering experiments suggest low local disorder for both ices.

Those structures being amorphous, the same procedure as used for the water spectra was employed. Therefore, the spectra presented here are the averaged spectra of 20 calculations performed on randomly chosen clusters with the smallest TIP3P dipole moment between 7 and 8 Å radius embedded in an 80 Å radius Madelung potential. For the amorphous ice clusters, the values in Equation 5-7 were chosen to be R_o=30 and D=8.

The spectra used to generate the averages spectra of amorphous ices are presented in Appendix 2.

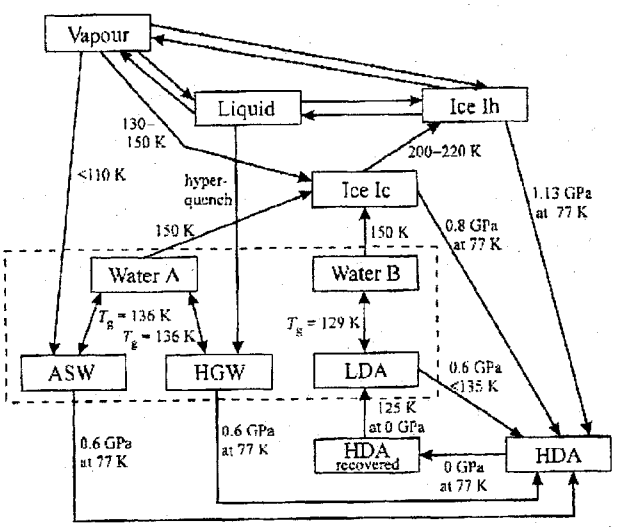

Figure 5-34 Flowchart of the forms of amorphous ice and other phases of ice and water. T_g indicates a glass transition and the dotted lines are a simplified approach where the entire region is considered LDA. ASW designates amorphous solid water and HGW hyperquenched glassy water.

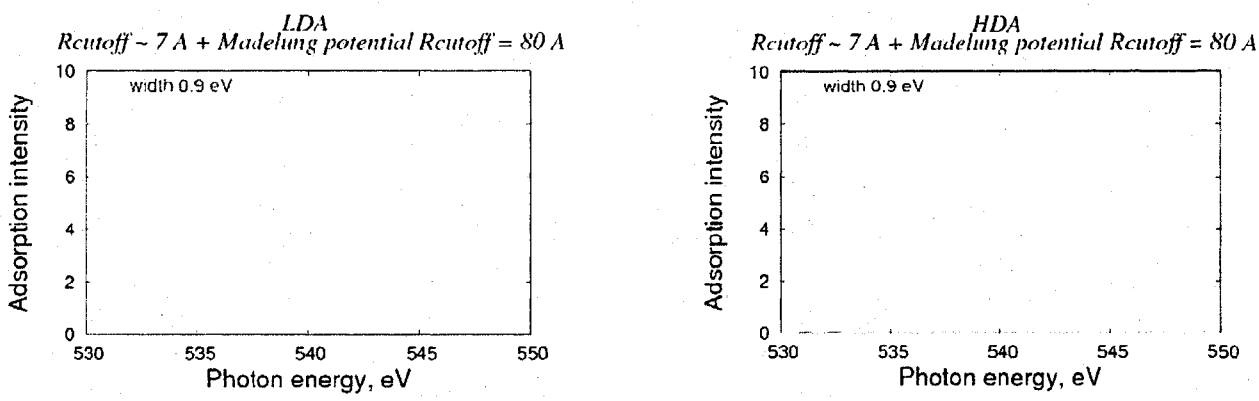

Figure 5-35 Average XAS spectra of LDA (left) and HDA (right) ices. Quantum cluster ~7 Å radius with point charges 80 Å radius

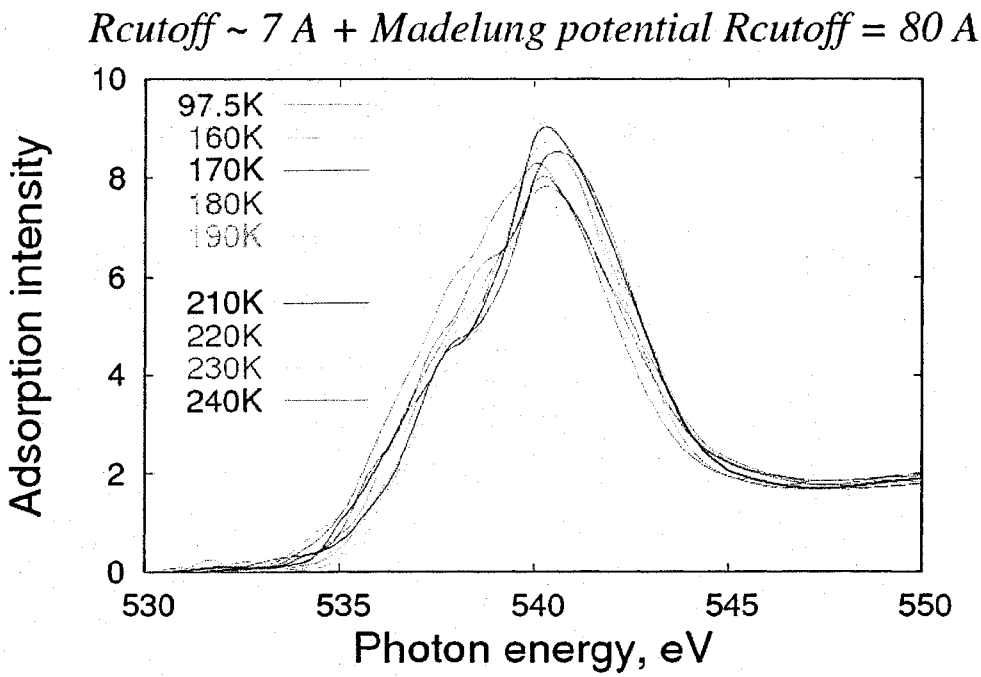

Figure 5-36 Average (20 central oxygen atoms) XAS spectra of amorphous ices at various temperatures. Quantum clusters ~7 Å radius with point charges 80 Å radius

5.4 Discussion

The gas phase spectrum of the oxygen *K*-shell, i.e. the spectrum of a single isolated water molecule, exhibits well-separated peaks corresponding to excitations of the 1s electron into the antibonding $4a_1$ and $2b_1$ molecular orbitals at low energies (534 and 536 eV), and transitions into the Rydberg orbitals at higher energies. The observed features of the oxygen *K*-shell spectra for water and ice can be divided into three regions: the pre-edge (535–537 eV), the main-edge (537–540 eV), and the post-edge (540–545 eV).

The ice spectrum is broadened with a pronounced post-edge peak at 541 eV and pre-edge and main-edge features at 535 eV and 537 eV, respectively. The spectrum of liquid water has a very strong pre-edge peak at 535 eV as well as an enhanced main-edge peak (537 eV) compared to ice. However, it has a weaker post-edge region (541 eV).

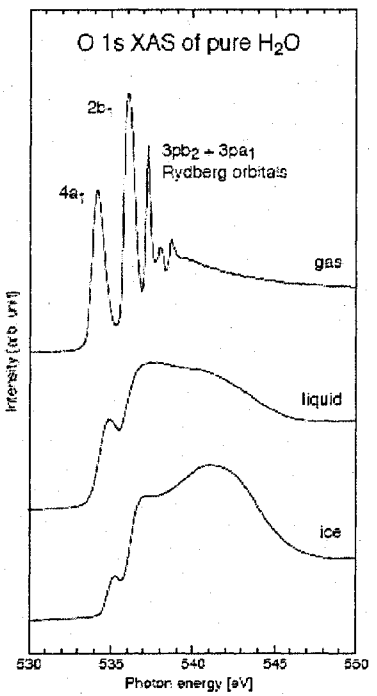

Figure 5-37 Experimental O *K*-edge XAS spectra of water in gas phase, liquid and ice [148, 168].

The first point to consider in the results of the calculations presented in section 5.3 is the influence of the Madelung potential on the calculated spectra. An exhaustive study was performed on the ice IX to determine the sizes of the quantum cluster and of the Madelung potential required to reach convergence. The bare quantum cluster calculations do not converge even for the largest clusters that include almost 70 water molecules. A quantum cluster having a radius taken between 7 and 8 Å and embedded in a 70 Å radius Madelung potential has proven to be well converged. Therefore, the same procedure was applied to all the other structures. The influence of the Madelung potential, beyond the drastic changes in the shape of the spectra, can also be envisaged by looking at the orbital energy levels. The HOMO-LUMO gap has been determined by several means and experiments by Grand et al. [169] and Coe et al. [170] found values of 7 eV and 6.9 eV respectively but DFT calculations seem to underestimate that value [171]. Incorporation of the Madelung potential leads to a significant increase in the band gap of the quantum mechanical cluster, from 2.8 eV for the bare site 1 oxygen cluster, to 5.1 eV for the same cluster embedded in a 70 Å radius Madelung potential. Furthermore, the HOMO-LUMO gap constantly decreases for the bare clusters but goes to the bulk band gap for clusters embedded in a Madelung potential.

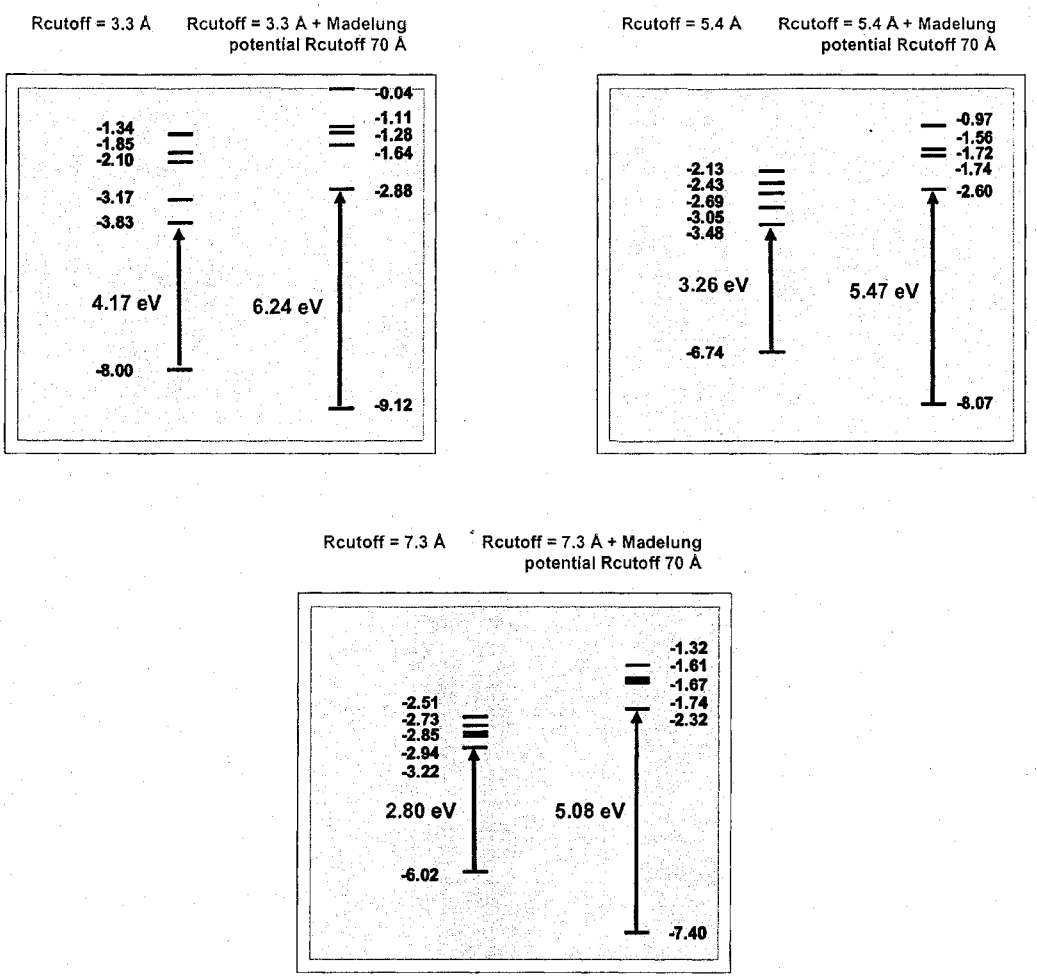

Figure 5-38 Influence of the Madelung potential on the HOMO-LUMO gap. Results come from site 1 of the ice IX structure (alpha spin).

As expected, the Slater approach (0.5 electron in the 1s core orbital) decreases the orbital energies due to the smaller screening.

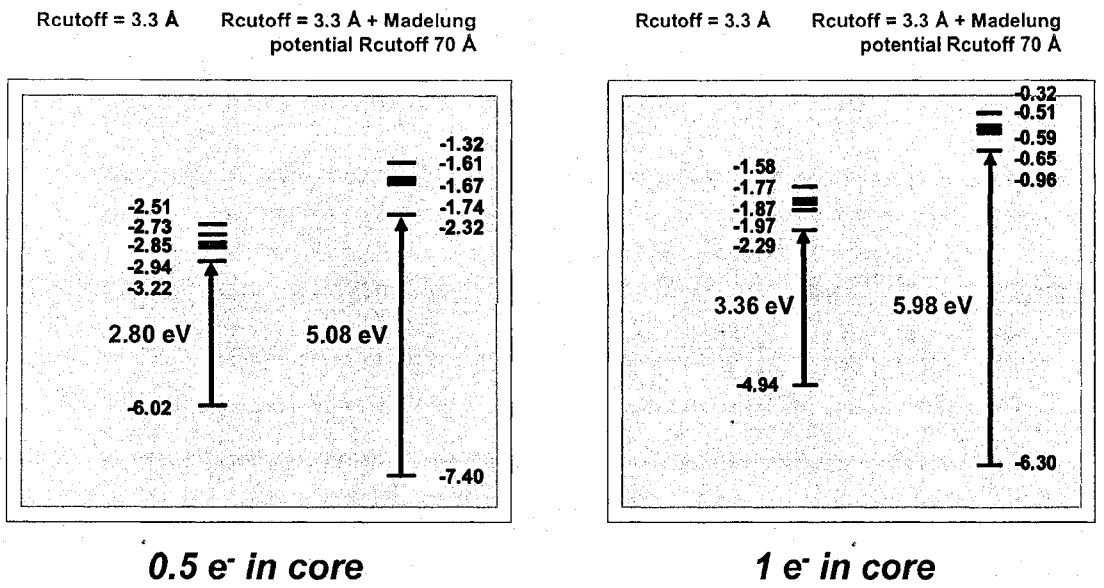

Figure 5-39 Influence of the Slater approach on the orbital energies with and without a Madelung potential. Results com from the site 1 of the ice IX structure (alpha spin).

The XAS spectrum is reported to be sensitive to broken or distorted hydrogen bonds. As can be seen in Figures 5-40 and 5-41, the hydrogen bond contribution on the central oxygen atom, almost non-existent in the bare cluster, is large, symmetric and similar to the one expected in the bulk for the cluster embedded in a Madelung potential. This is true for the smaller quantum cluster as well as for the larger one.

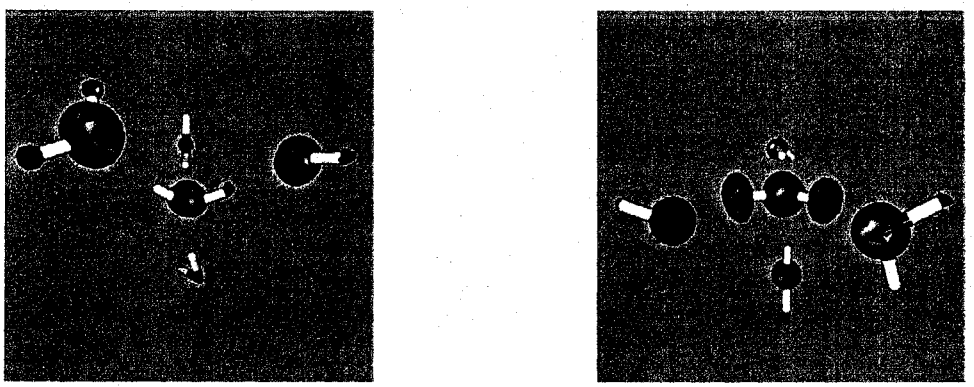

Figure 5-40 Influence of the Madelung potential on the orbital shapes. Contour plots of the LUMO orbital from site 1 of the ice IX structure for a 3.3 Å radius cluster without (left) and with (right) 70 Å radius point charges (isovalue 0.05).

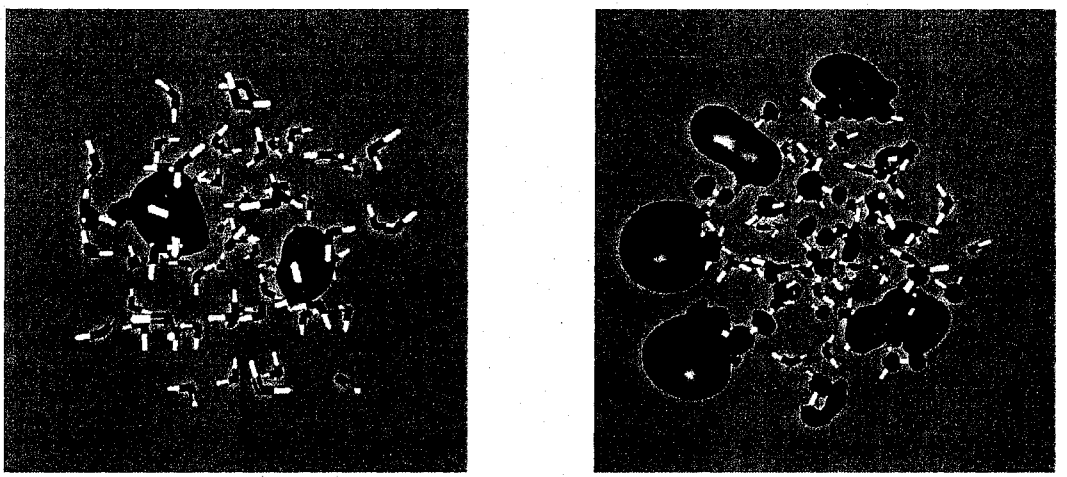

Figure 5-41 Influence of the Madelung potential on the orbital shapes. Contour plots of the LUMO orbital from the site 1 of the ice IX structure for a 7.3 Å radius cluster without (left) and with (right) 70 Å radius point charges (isovalue 0.07).

Convergence was reached for a quantum cluster chosen between 7 and 8 Å radius embedded in a 70 Å radius Madelung potential for all the structures but ice VIII. Three clusters with a radius ranging between 7 and 8 Å were found to have a small TIP3P dipole moment and the calculations on those three structures were performed. Ice VIII contains

only a single type of oxygen atom and therefore, the spectra should be identical. It is the case for the first two but the 7.32 Å cluster gives a different spectrum. To confirm these spectra were converged, the calculations were repeated on the same quantum clusters but with a large number of point charges. The first two spectra remain exactly the same but the third one is modified as can be seen in Figure 5-42. Thus, the 7.32 Å cluster seems not to be converged yet and this may be due to the large dipole moment of the ice VIII structure that is reflected in the Madelung potential embedding the quantum clusters.

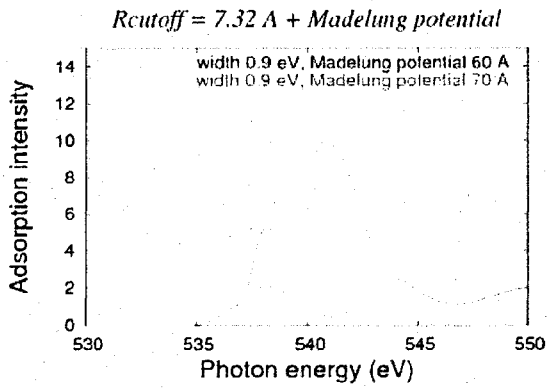

Figure 5-42 Comparison of the ice VIII spectra for the 7.32 Å radius cluster with different Madelung potentials.

However, as can be seen in Figure 5-43, the pre-edge peaks (A) already originate from orbitals localized on the central oxygen when then post-edge peaks (C) originate from delocalized orbitals. On the other hand, the main-edge features (B) come mostly from delocalized orbitals and only the B1 peak has contribution from an orbital localized on the excited oxygen atom. Not all the orbitals contributing to the three regions are presented but all the orbitals having large contributions to the labeled peaks have similar features to the one depicted in Figure 5-43.

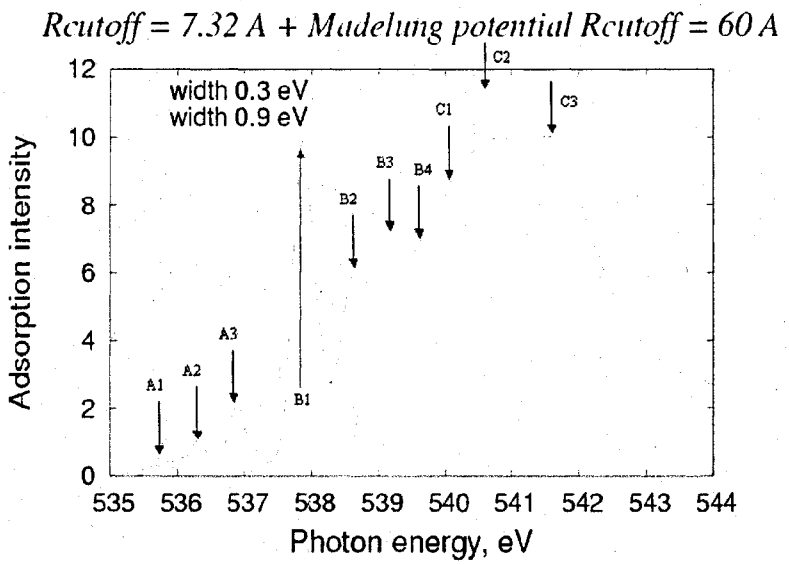

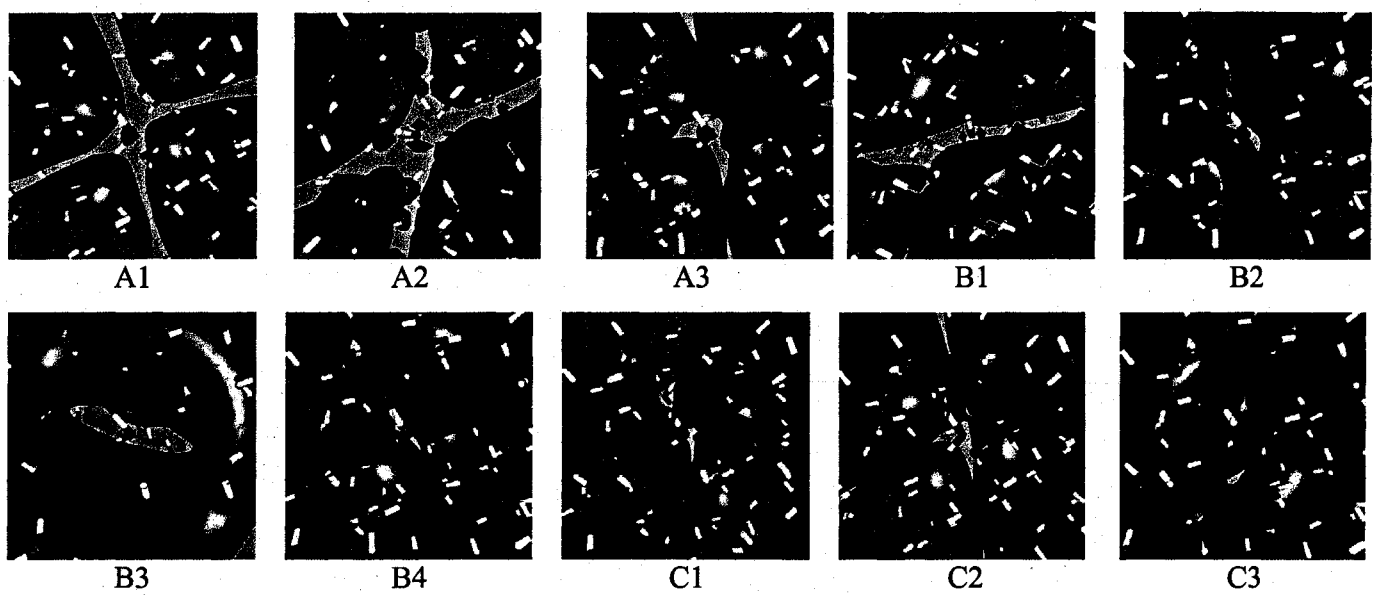

Figure 5-43 XAS spectrum of ice VIII for the 7.32 Å radius cluster with 60 Å Madelung potential. Plots of the molecular orbitals in which the 1s electron is excited (isovalue 0.09). A contribution of the central oxygen atom is present for all pre-edge features (A) and for the first main edge peak (B1). There is neither contribution from the central oxygen atom for the other main edge peaks (B2 to B4) nor for the post edge features (C).

This proved that convergence should always carefully be checked to ensure the validity of the spectra presented.

The experimental spectra of several of the structures studied here, i.e. liquid water, ice II and ice IX, are presented in the following figure.

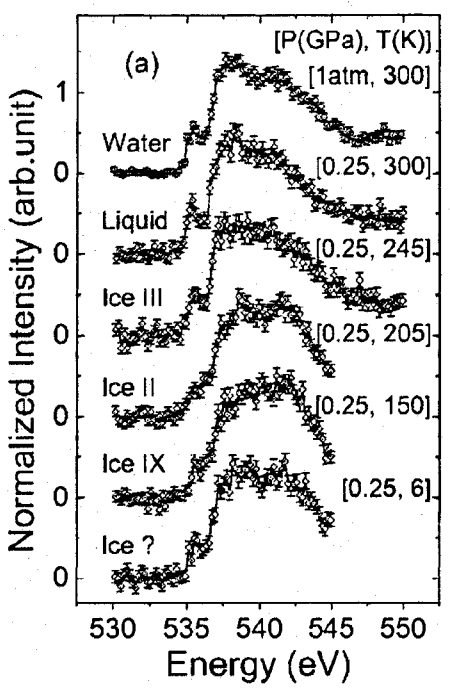

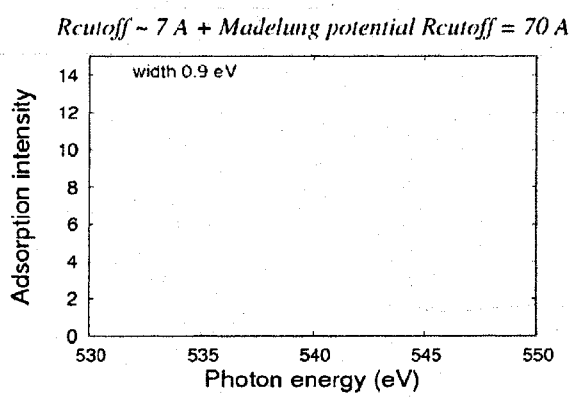

ice II

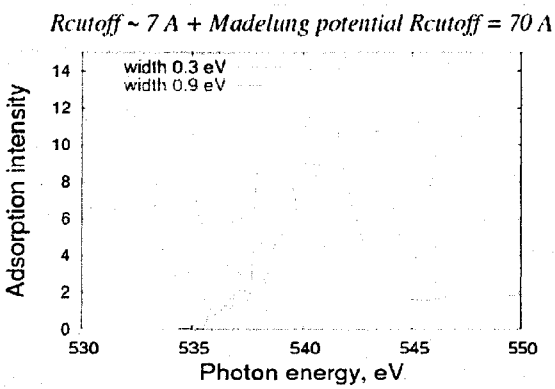

ice IX

Figure 5-44 Experimental spectra of various ice structures and water [172] and calculated spectra for ices II and IX.

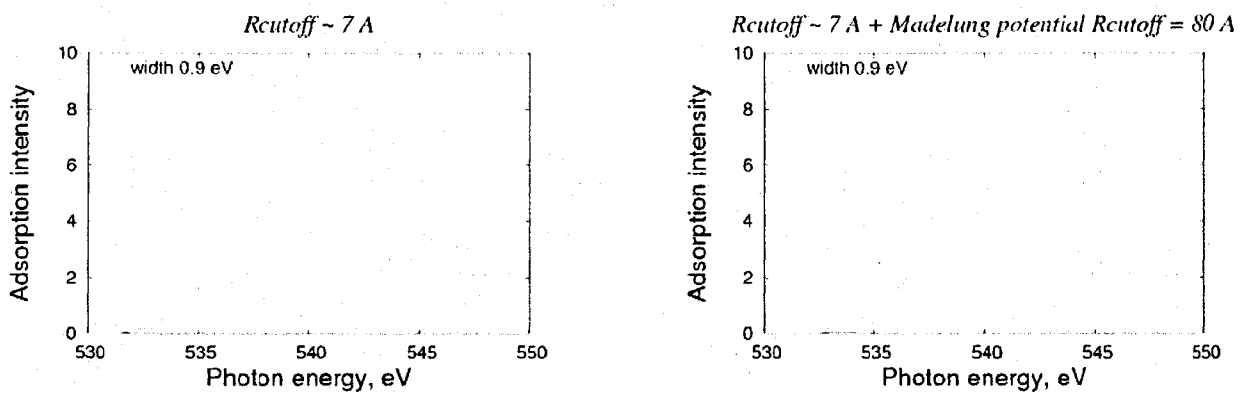

Figure 5-45 Average XAS spectrum of water (20). Quantum cluster ~7.00 Å radius without point charges and with point charges 80 Å radius.

It has been argued that the origin of the pre-edge feature in the water spectrum was due to unsaturated hydrogen bonds [173, 174] (a single hydrogen bond donor per water molecule) present in the water structure and that the rather weaker pre-edge peaks found in the experimental spectra of crystalline ices came from the surface contribution which encounters reconstruction and therefore does not have a perfectly tetrahedral geometry. A similar interpretation of the water surface was also provided [175]. The tetrahedral symmetry of ice induces an increase of the local symmetry resulting in the removal of the p character from the 4a1 level (lowest unoccupied orbital) leading to weak intensity in the pre-edge. In the case of a broken donating hydrogen bond, the asymmetry on the hydrogen side causes a1 and b2 orbitals mixing resulting in unoccupied antibonding orbitals that are localized along the internal O-H bond. The resulting increase of p-character translates to an intensity increase in the pre-edge region [91, 129, 174]. Furthermore, H-bonds have been found to be predominantly broken by bending rather than by elongation [91].

The post edge was assigned to water molecules with two strong donating hydrogen bonds, i.e. water molecules having a tetrahedral environment such as the one found in ice [91,

[95, 168, 176-179]. This feature is reported to be associated to excitation into antibonding localized O-H orbitals along the hydrogen bond [174]. Based on those results, a new model of water was proposed with a major presence of broken hydrogen bonds (2.2 hydrogen bonds per water molecule as opposed to the traditional almost tetrahedral structure with 3.5 hydrogen bonds per water molecule). However, a recent Compton scattering study [180, 181] could not corroborate those results but proved a correlation exist between the bond length and angle distortion in water. However, the calculations supporting this idea were performed on rather small clusters that were not embedded in a Madelung potential and consequently not converged. The present calculations performed on the proton-ordered ices have pre-edge features that are even enhanced by the presence of the Madelung potential, as well as the post-edge, compared to the equivalent bare clusters. Those crystalline ices have a perfect tetrahedral environment and therefore the assignment of the pre-edge peak to the presence of broken hydrogen bonds has been given a pounding as was previously done by Cai et al. [172] and particularly by Prendergast et al. [182].

Chemical bonding has a large impact on the valence electronic structure. Consequently, the various hydrogen bonding configurations influence the local molecular orbital structure and is expected to be reflected in XAS. It has been suggested that the first coordination shell surrounding the excited oxygen atom was the origin of the spectral profile. Therefore, varying the basis set on the nearest neighbors, water molecules within a radius of 3.5 Å from the central oxygen atom, and adding more diffuse functions should improve the agreement with experiment [168].

To assess the claim that the nearest neighbors have a major influence on the XAS spectra [183], more diffuse basis sets were added on the nearest neighbors of several structures to check the modifications of the pre-edge features. IGLO II (O (9s, 5p, 1d) → [5s, 4p, 1d]) or IGLO III (O (11s, 7p, 2d) → [7s, 6p, 2d]) [164, 165] replaced the previous basis set on the nearest oxygen atoms. The results presented in the three following Figures prove that adding diffuse functions to the nearest neighbors does not improve the fit of the calculated spectra with experiment as the initial results are only recovered when IGLO III are added on the nearest

neighbors. The pre-edge feature is not enhanced by the presence of an IGLO basis set on the first coordination shell, reinforcing the idea that this feature comes from localized orbitals. The main-edge and the post-edge are not improved either and this proves that the delocalization (broad conduction band in ice [129]) causing those features has to be taken account for on a much larger range.

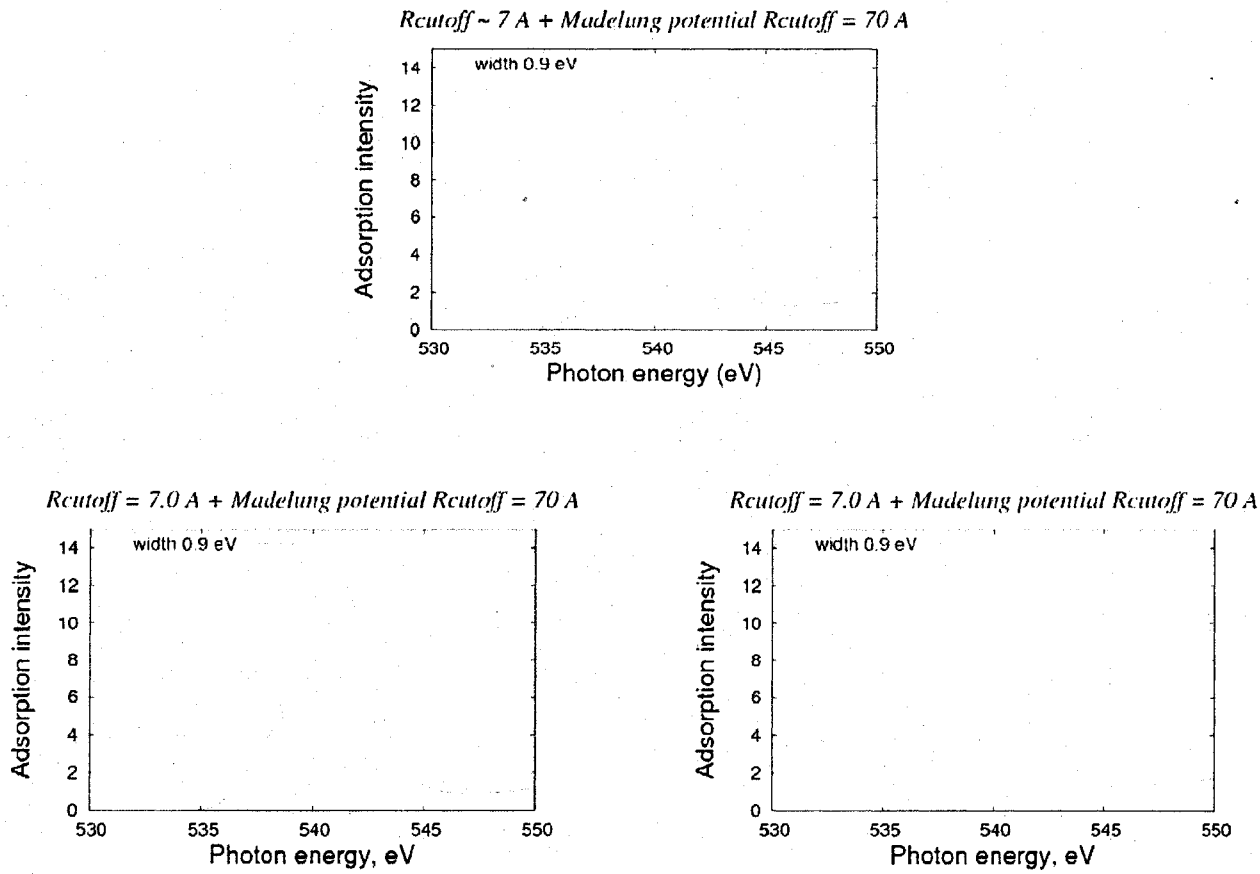

IGLO II IGLO III

Figure 5-46 Average XAS spectrum of ice II for quantum clusters ~7 Å radius with point charges 70 Å radius with various basis sets on the 4 nearest neighbors.

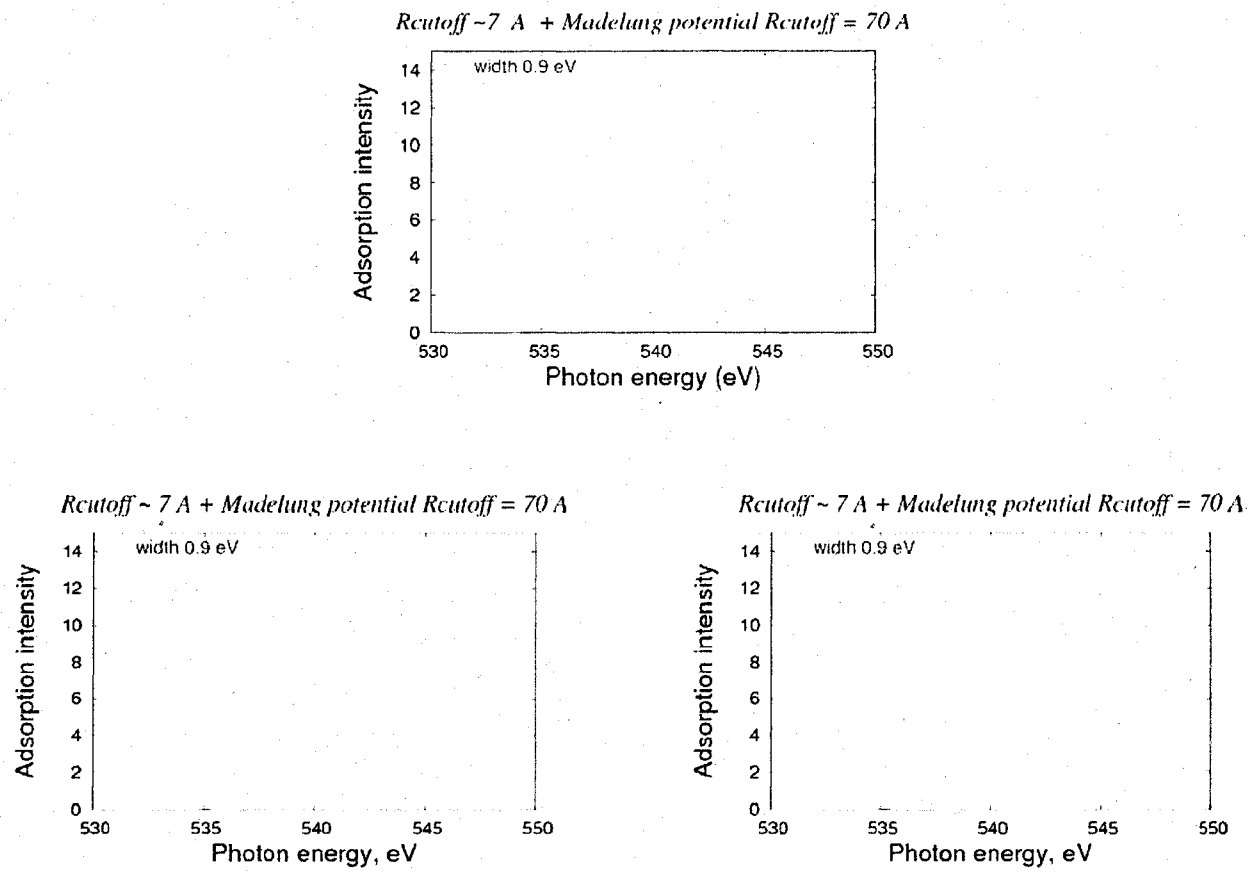

IGLO II IGLO III

Figure 5-47 Average XAS spectrum of the ice IX for quantum clusters ~7 Å radius with point charges 70 Å radius with various basis sets on the 4 nearest neighbors.

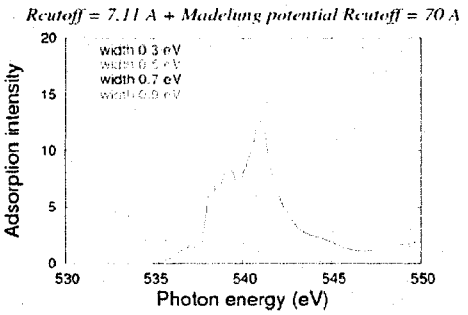

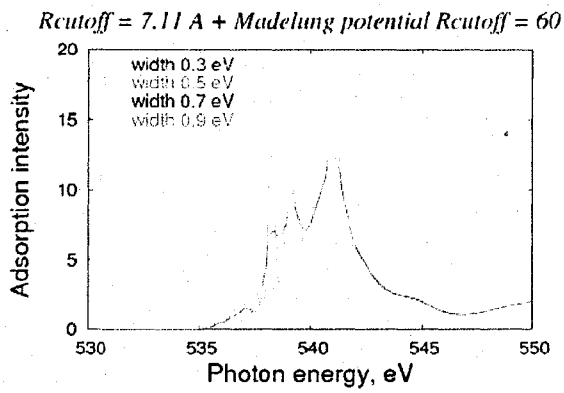

IGLO II on the 2 nearest neighbors

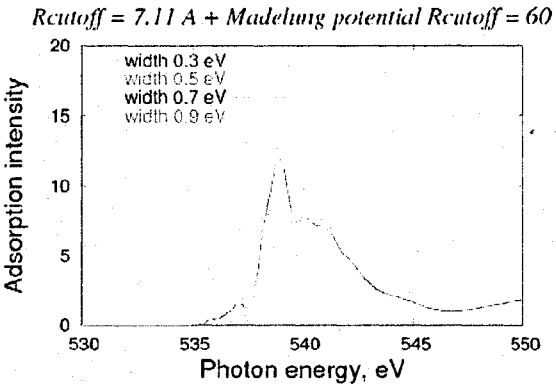

IGLO II on the 6 nearest neighbors

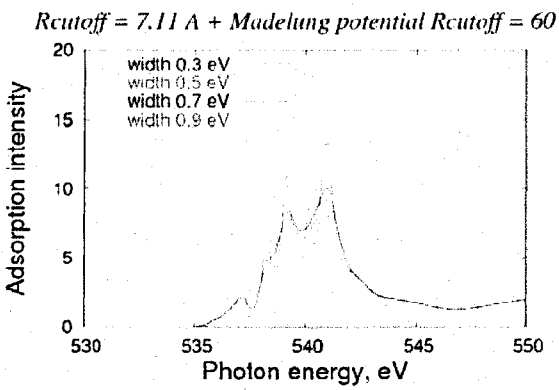

IGLO II on the 8 nearest neighbors

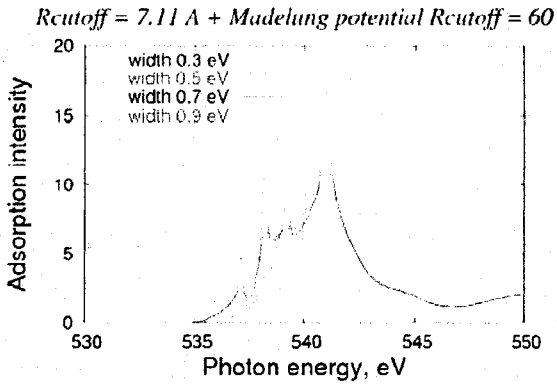

IGLO III on the 8 nearest neighbors

Figure 5-48 XAS spectrum of ice VIII for a quantum cluster 7.11 Å radius with point charges 70 Å radius with various basis sets on the nearest neighbors.

Finally, the comparison of experimental and calculated spectra for the amorphous ices HDA and LDA indicate the poor description of the main-edge and post-edge features. The broad pre-edge is qualitatively present in the calculated spectra but our methodology fails to reproduce the other features. The attempt to study the transition pathway from one amorphous ice to the other as shown in Figure 5-36, has been totally unsuccessful.

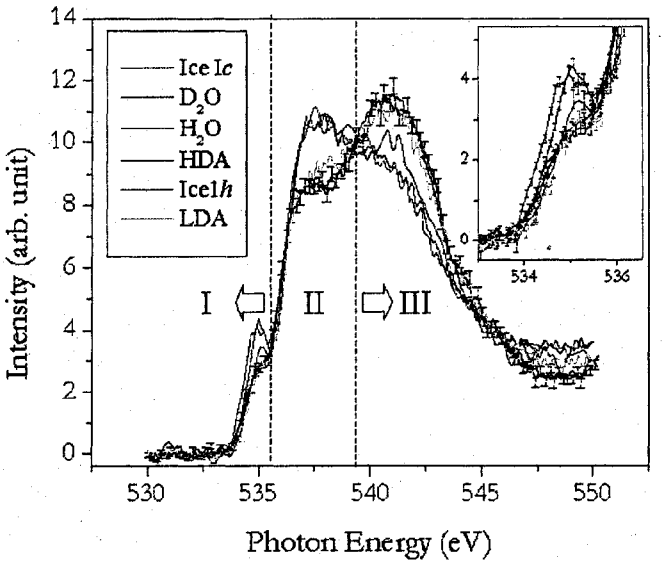

Figure 5-49 Experimental XAS spectra of LDA and HDA ices produced by J. S. Tse.

A study by Prendergast et al. found that the unoccupied states are sensitive to finite-size effects [184]. The same work demonstrates that the electronic structure of water is relatively insensitive to the long-range disorder and that the saturation of all hydrogen bonds in crystalline ice leads to a more delocalized state compared to water [184]. This is consistent with the present results for crystalline and amorphous structures. The main-edge and post-edge features will be more important in a crystalline structure where the delocalization plays a major role. The disruption in the band structure due to the emergence of defects (amorphous ices and water) will imply a localization and therefore an increase of the pre-edge feature in the spectra. The extent of cooperative effects demonstrated in Chapter 3 can explain the influence of the Madelung potential on the shape of the spectra, particularly on the pre-edge

peak. It has been suggested that some of the intensity of the pre-edge peak in crystalline ices may be due to the influence of the local electronic structure by the Madelung potential of the crystal lattice [172]. It has also been shown that introducing disorder will reduce the peak height at 539-540 eV when going from ice to amorphous structure [182] that is still coherent with a disruption of the band structure.

Finally, another attempt to obtain a better description of XAS features was made. The full core hole method, where an entire electron is removed from the 1s orbital, should reproduce more accurately the higher energy excitations to progressively more delocalized states. It however overestimates the pre-edge and consequently underestimates the main peak height by virtue of the oscillator strength sum rule [182]. The calculations performed did not improve the half core results, as was found by previous work [185], and therefore, they will not be presented here.

A periodic approach could potentially solve the problem of description of the delocalized structure but other drawbacks will occur with such methods, such as the description of the localized core or the Z+1 method that overestimates final states [186]. The discrepancy may also be caused by neglecting multi-electron excitations near the ionization threshold [172].

5.5 Conclusion

The influence of the periodic crystalline environment was proven to be drastic on the computed spectra of the four proton-ordered ices as well as the disordered structures of water and various amorphous ices. The influence of the size of the quantum cluster was studied and it was found that small clusters can be used, as long as it is subject to a converged Madelung potential. In the case of water and amorphous ices, sampling a large number of oxygen centers is required to obtain a converged spectrum. A study of the influence of the

basis set on the nearest neighbors of the excited oxygen atom was performed. The outer coordination shells and the long-range electrostatic potential must be taken into account in a quantitative simulation. A reasonable agreement was obtained with experimental results. Though the method used here seems to perform well in the pre-edge region involving localized molecular orbitals, it fails to reproduce the main-edge and post-edge regions exactly as a localized basis set, even including diffuse functions, cannot account for a delocalized band structure. The case of water and amorphous ices, for which calculated spectra did not provide good results, also prove that in some cases, multiple electron transitions might have to be considered in the calculation of X-ray absorption spectra.

General Conclusion

The major influence of cooperativity in hydrogen bonded water systems has been demonstrated in this work. In a first step, the lengthening of a chain of water molecules has proven to decrease drastically the activation barrier in the reaction pathway leading to the formation of the amino alcohol NH_2CH_2OH from ammonia and formaldehyde. The water molecules can in this case be considered as a catalyst in this reaction.

A more systematic study of cooperative effects in different models of ice has been performed. The extent of cooperativity was evaluated and found to be quite large and it occurs on a very long length scale. It is found that charge transfer and electrostatic effects play a role in cooperativity. The results are important, particularly in reactions where ions are involved. This is not uncommon in many biological systems.

The last chapter is concerned with the X-ray absorption study of several ices and water structures and provide examples on the importance of cooperativity. It is found that a cluster embedded in a converged Madelung potential is needed to account for the cooperative effects in order to achieve reasonable agreement of the calculated O K-edge X-ray absorption spectra with experiments. The investigation of the local structure of liquid water performed here did not support a recent controversial model for the structure of liquid water with a highly broken hydrogen bond network. The results show that the approximations employed in the calculations of the X-ray absorption spectra is not exact and sufficient enough to reproduce accurately main-edge and post-edge features which originated from delocalized band structure.

In summary, the research performed in this thesis shows that cooperativity is a vital part of hydrogen bonded systems. Quantum treatment of a system must be able to account for charge transfer embedded within an electrostatic potential that accounts for long-range effects.

Appendix

See attached disc.

References

1. Buckingham, A. D.; Fowler, P. W.; Hutson, J. M., *Chem. Rev.* **1988,** 88, 963.

2. Dang, L. X., *J. Phys. Chem.* **1998,** 102, 620.

3. Sokolov, N. D., Electrostatic model of cooperative effects in hydrogen-bonded systems: cooperative effect of base and cation on the A-H stretching vibrational frequency. *J. Mol. Struct. (Theochem)* **1997,** 436-437, 201.

4. Bryce, R. A.; Vincent, M. A.; Malcolm, N. O. J.; Hillier, I. H.; Burton, N. A., Cooperative effects in the structuring of fluoride water clusters: Ab initio hybrid quantum mechanical/molecular mechanical model incorporating polarizable fluctuating charge solvent. *J. Chem. Phys.* **1998,** 109, (8), 3077.

5. King, B. F.; Weinhold, F., *J. Chem. Phys.* **1995,** 103, 333.

6. Reed, A. E.; Curtiss, L. A.; Weinhold, F., *Chem. Rev.* **1988,** 88, 899.

7. Szabó, A.; Ostlund, N. S., *Modern quantum chemistry : introduction to advanced electronic structure theory*. Macmillan Pub.: New York, 1982; p xvi, 446 p.

8. Born, M.; Oppenheimer, R., *Ann. Phys.* **1927,** 84, 457.

9. Levine, I. N., *Quantum Chemistry*. Prentice Hall: 2000.

10. Blinder, S. M., *Am. J. Phys.* **1927,** 33, 431.

11. Roothaan, C. C. J., *Rev. Mod. Phys.* **1951,** 23, 69.

12. Leach, A., *Molecular Modelling: Principles and Applications*. 1st Ed ed.; Addison Wesley Longman: Essex, 1996.

13. Daudel, R.; Leroy, G.; Peeters, D.; Sana, M., *Quantum Chemistry*. Wiley: New York, 1983.

14. Hehre, W. J.; Radom, L.; Schleyer, P. v. R.; Pople, J. A., *Ab Initio Molecular Orbital Theory*. Wiley: New York, 1985.

15. Christoffersen, R. E., *Basic principles and techniques of molecular quantum mechanics*. Springer-Verlag: New York, 1989.

16. Bartlett, R. J., *Annu. Rev. Phys. Chem.* **1981,** 32, 359.

17. Møller, C.; Plesset, M. S., Note on an Approximation Treatment for Many-Electron Systems. *Phys. Rev* **1934,** 46, 618.

18. Leininger, M. L.; Allen, W. D.; Schaefer, H. F.; Sherrill, C. D., Is Moller-Plesset perturbation theory a convergent ab initio method? *J. Chem. Phys.* **2000,** 112, (21), 9213.

19. Pople, J. A.; Seeger, R., Electron density in Moller-Plesset theory. *J. Chem. Phys.* **1975,** 62, (11), 1566.

20. Head-Gordon, M.; Pople, J. A.; Frisch, M. J., MP2 energy evaluation by direct methods. *Chem. Phys. Lett.* **1988,** 153, (6), 503.

21. Frisch, M. J.; Head-Gordon, M.; Pople, J. A., A direct MP2 gradient method. *Chem. Phys. Lett.* **1990,** 166, (3), 275.

22. Frisch, M. J.; Head-Gordon, M.; Pople, J. A., Semi-direct algorithms for the MP2 energy and gradient *Chem. Phys. Lett.* **1990,** 166, (3), 281.

23. Hoffmann, M. R.; Schaefer, H. F., A full coupled-cluster singles, doubles, and triples model for the description of electron correlation. *Adv. Quant. Chem.* **1986,** 18, 207.

24. Kucharski, S. A.; Bartlett, R. J., Fifth-order many-body perturbation theory and its relationship to various coupled-cluster approaches. *Adv. Quant. Chem.* **1986,** 18, 281.

25. Yamaguchi, K., configuration interaction, coupled-cluster and many-body perturbation approaches in the unrestricted Hartree-Fock-Slater model. *Chem. Phys. Lett.* **1979,** 68, (2-3), 477.

26. Cramer, C. J., *Essentials of Computational Chemistry: Theories and Models*. Wiley: 2004.

27. Kümmel, H. G. In *A biography of the coupled cluster method - found in R.F. Bishop, T. Brandes, K.A. Gernoth, N.R. Walet, Y. Xian Recent progress in many-body theories,*

Proceedings of the 11th international conference, Singapore, 2002; World Scientific Publishing: Singapore, 2002; p 334.

28. Noga, J.; Bartlett, R. J., The full CCSDT model for molecular electronic structure. *J. Chem. Phys.* **1987,** 86, (12), 7041.

29. Noga, J.; Bartlett, R. J.; Urban, M., Towards a full CCSDT model for electron correlation. CCSDT-n models. *Chem. Phys. Lett.* **1987,** 134, (2), 126.

30. Scuseria, G. E.; Schaefer, H. F., A new implementation of the full CCSDT model for molecular electronic structure. *Chem. Phys. Lett.* **1988,** 152, (4,5), 382.

31. Parr, R. G.; Yang, W., *Density-functional theory of atoms and molecules*. Oxford University Press: New York, 1989; p ix, 333 p.

32. Seminario, J. M., *Recent developments and applications of modern density functional theory*. Elsevier: 1996.

33. Koch, W.; Holthausen, M. C., *A chemist's guide to density functional theory*. Wiley: 2000.

34. Engel, E.; Dreizler, R. M.; Gross, E. K. U.; Dobson, J. F.; Petersilka, M.; Rajagopal, A. K.; Buot, F. A., *Density functional theory II*. Springer: 1996; Vol. 181.

35. Hohenberg, P.; Kohn, W., *Phys. Rev. B* **1964,** 136, 864.

36. Kohn, W.; Sham, L. J., *Phys. Rev. A* **1965,** 140, 1133.

37. Seminario, J. M.; Burke, K.; Ludeña, E. V.; Zhou, Z.; Dunlap, B. I.; Johnson, B. G.; Delley, B.; Scherrer, P.; Abashkin, Y.; Malkin, V. G.; Broclawik, E.; Politzer, P.; Balbuena, P. B., *Modern Density Functional Theory - A Tool for Chemistry, Theoretical and Computational Chemistry*. Elsevier: Amsterdam, 1995; Vol. 2.

38. Salahub, D. R.; Fournier, R.; Mynarski, P.; Papai, I.; St-Amant, A.; Ushio, J., *Density Functional Methods in Chemistry*. Springer-Verlag: New York, 1991; p 77-100.

39. Slater, J. C., *Quantum Theory of Molecules and Solids:The self-consistent field for molecules and solids* McGraw-Hill: New York, 1974; Vol. 14.

40. Johnson, B. G., *Modern Density Functional Theory - A Tool for Chemistry, Theoretical and Computational Chemistry*. Elsevier: Amsterdam, 1995; Vol. 2, p 169.

41. Dunlap, B. I., *Modern Density Functional Theory - A Tool for Chemistry, Theoretical and Computational Chemistry*. Elsevier: Amsterdam, 1995; Vol. 2, p 151.

42. Thomas, L. H., *Proc. Camb. Phil. Soc.* **1927,** 23, 542.

43. Fermi, E., *Z. Phys.* **1928,** 48, 73.

44. Vosko, S. H.; Wilk, L.; Nusair, M., *Can. J. Phys.* **1980,** 58, 1200.

45. Ceperly, D. M.; Alder, B. J., *J. Phys. Rev. Lett.* **1980,** 45, 566.

46. Perdew, J. P.; Zunger, A., *Phys. Rev. B* **1981,** 23, 5048.

47. Becke, A. D., *J. Chem. Phys.* **1988,** 88, 1053.

48. Becke, A. D., *Phys. Rev. A* **1988,** 38, 3098.

49. Perdew, J. P.; Burke, K.; Wang, Y., *Phys. Rev. B* **1996,** 84, 16533.

50. Lee, C.; Yang, W.; Parr, R. G., *Phys. Rev. B* **1988,** 37, 785.

51. Becke, A. D., *J. Chem. Phys.* **1993,** 98, 1372.

52. Becke, A. D., *J. Chem. Phys.* **1993,** 98, 5648.

53. Rabuck, A. D.; Scuseria, G. E., Performance of recently developed kinetic energy density functionals for the calculation of hydrogen binding strengths and hydrogen-bonded structures. *Theor. Chem. Acc.* **2000,** 104, 439.

54. Eisenberg, D.; Kauzmann, W., *The structure and properties of water*. Oxford Press: 2005.

55. Schuster, P.; Zundel, G.; Sandorfy, C., *The hydrogen bond*. North-Holland Publishing Company: Amsterdam, 1976; Vol. 3.

56. Hobbs, P. V., *Ice Physics*. Clarendon Press: Oxford, 1974.

57. Herzenberg, A.; Woolfson, M. M.; Ziman, J. M., *The chemical physics of ice*. Cambridge Monographs on Physics: 1970.

58. http://www.lsbu.ac.uk/water/models.html

59. Scheiner, S., Ab initio studies of hydrogen bonds: the water dimer paradigm. *Annu. Rev. Phys. Chem.* **1994,** 45, 23.

60. Fletcher, N. H., Structural aspects of the ice-water system. *Rep. Prog. Phys.* **1971,** 34, 913.

61. Bernal, J. D.; Fowler, R. H., A theory of water and ionic solution, with particular reference to hydrogen and hydroxyl ions. *J. Chem. Phys.* **1933,** 1, 515.

62. Fortes, A. D.; Wood, I. G.; Brodholt, J. P.; Vocadlo, L., *Icarus* **2003,** 162, 59.

63. Fortes, A. D.; Wood, I. G.; Brodholt, J. P.; Vocadlo, L., Ab initio simulation of the ice II structure. *J. Chem. Phys.* **2003,** 119, (8), 4567.

64. Kuhs, W. F.; Finney, J. L.; Vettier, C.; Bliss, D. V., *J. Chem. Phys.* **1984,** 81, (8), 3612.

65. Londono, J. D.; Kuhs, W. F.; Finney, J. L., *J. Chem. Phys.* **1993,** 98, 4878.

66. Leadbetter, A. J.; Ward, R. C.; Clark, J. W.; Tucker, P. A.; Matsuo, T.; Suga, H., The equilibrium low-temperature structure of ice. *J. Chem. Phys.* **1985,** 82, (1), 424.

67. Johari, G. P., An interpretation for the thermodynamic features of ice Ih - ice XI transformation. *J. Chem. Phys.* **1998,** 109, (21), 9543.

68. Howe, R.; Whitworth, R. W., A determination of the crystal structure of ice XI. *J. Chem. Phys.* **1989,** 90, (8), 4450.

69. Pisani, C.; Casassa, S.; Ugliengo, P., Proton-ordered ice structures at zero pressure. A quantum-mechanical investigation. *Chem. Phys. Lett.* **1996,** 253, 201.

70. Barkema, G. T.; de Boer, J., Properties of a statistical model of ice at low temperatures. *J. Chem. Phys.* **1993,** 99, (3), 2059.

71. Li, J.-C.; Nield, V. M.; Jackson, S. M., Spectroscopic measurements of ice XI. *Chem. Phys. Lett.* **1995,** 241, 290.

72. Itoh, H.; Kawamura, K.; Hondoh, T.; Mae, S., Polarized librational spectra of proton-ordered ice XI by molecular dynamics simulations. *J. Chem. Phys.* **1998,** 109, (12), 4894.

73. Line, C. M. B.; Whitworth, R. W., A high resolution neutron powder diffraction study of D2O ice XI. *J. Chem. Phys.* **1996,** 104, (24), 10008.

74. Benoit, M.; Bernasconi, M.; Focher, P.; Parrinello, M., New high-pressure phase of ice. *Phys. Rev. Lett.* **1996,** 76, (16), 2934.

75. Umemoto, K.; Wentzcovitch, R. W.; Baroni, S.; de Gironcoli, S., Anomalous Pressure-Induced Transition(s) in Ice XI. *Phys. Rev. Lett.* **2004,** 92, (10), 105502.

76. Ludwig, R., Water : from clusters to the bulk. *Angew. Chem. Int. Ed.* **2001,** 40, 1808.

77. Espinosa, E.; Molins, E.; Lecomte, C., Hydrogen bond strengths revealed by topological analyses of experimentally observed electron densities. *Chem. Phys. Lett.* **1998,** 285, 170.

78. Benoit, M.; Romero, A. H.; Marx, D., Reassigning hydrogen-bond centering in dense ice. *Phys. Rev. Lett.* **2002,** 89, (14), 145501.

79. Stanley, H. E.; Teixeira, J., Interpretation of the unusual behavior of H2O and D2O at low temperature: tests of a percolation model. *J. Chem. Phys.* **1980,** 73, 3404.

80. Bartha, F.; Kapuy, O.; Kozmutza, C.; Van Alsenoy, C., Analysis of weakly bound structures: hydrogen bond and the electron density in a water dimer. *J. Mol. Struct. (Theochem)* **2003,** 666-667, 117.

81. Tombari, E.; Ferrari, C.; Salvetti, G., Heat capacity anomaly in a large sample of supercooled water. *Chem. Phys. Lett.* **1999,** 300, 749.

82. Luck, W. A. P., The importance of cooperativity for the properties of liquid water. *J. Mol. Struct.* **1998,** 448, 131.

83. Keutsch, F. N.; Saykally, R. J., Water clusters: Untangling the mysteries of the liquid, one molecule at a time. *Proc. Natl. Acad. Sci. USA* **2001,** 98, 10533.

84. Eaves, J. D.; Loparo, J. J.; Fecko, C. J.; Roberts, S. T.; Tokmakoff, A.; Geissler, P. L., Hydrogen bonds in liquid water are broken only fleetingly. *Proc. Natl. Acad. Sci. USA* **2005,** 102, 13019.

85. Loparo, J. J.; Roberts, S. T.; Tokmakoff, A., Multidimensional infrared spectroscopy of water. I. Vibrational dynamics in two-dimensional IR line shapes. *J. Chem. Phys.* **2006,** 125, 194521.

86. Loparo, J. J.; Roberts, S. T.; Tokmakoff, A., Multidimensional infrared spectroscopy of water. II. Hydrogen bond switching dynamics. *J. Chem. Phys.* **2006,** 125, 194522.

87. Truskett, T. M.; Dill, K. A., A simple analytical model of water. *Biophys. Chem.* **2003,** 105, 449.

88. Delle Site, L.; Alavi, A.; Lynden-Bell, R. M., The electrostatic properties of water molecules in condensed phases: an ab initio study. *Mol. Phys.* **1999,** 96, (11), 1683.

89. Ojamae, L.; Hermansson, K., Ab initio study of cooperativity in water chains: binding energies and anharmonic frequencies. *J. Phys. Chem.* **1994,** 98, 4271.

90. Jorgensen, W. L.; Chandrasekhar, J.; Madura, J. D.; Impey, R. W.; Klein, M. L., Comparison of simple potential functions for simulating liquid water. *J. Chem. Phys.* **1983,** 79, 926.

91. Wernet, P., The Structure of the First Coordination Shell in Liquid Water. *Science* **2004,** 304, (5673), 995.

92. Head-Gordon, T.; Johnson, M. E., Tetrahedral structure or chains for liquid water. *Proc. Natl. Acad. Sci. USA* **2006,** 103, 7973.

93. Head-Gordon, T.; Johnson, M. E., Correction for Head-Gordon et al., Tetrahedral structure or chains for liquid water. *Proc. Natl. Acad. Sci. USA* **2006,** 103, 16614.

94. Soper, A. K., *Chem. Phys.* **2000,** 258, 121.

95. Smith, J. D.; Cappa, C. D.; Wilson, K. R.; Messer, B. M.; Cohen, R. C.; Saykally, R. J., Energetics of hydrogen bond network rearrangements in liquid water. *Science* **2004,** 306, 851.

96. Xenides, D.; Randolf, B. R.; Rode, B. M., Hydrogen bonding in liquid water: An ab initio QM/MM MD simulation study. *J. Mol. Liquids* **2006,** 123, 61.

97. Kusalik, P. G.; Svishchev, I. M., The spatial structure in liquid water. *Science* **1994,** 265, 1219.

98. Bernstein, M. P.; Allamandola, L. J.; Sandford, S. A., *Adv. Space Res.* **1997,** 19, 991.

99. Tielens, A. G. G. M.; Hagen, W.; Greenberg, J. M., *J. Phys. Chem.* **1983,** 87, 4220.

100. Scharberg, M. A., *Astrophys. J.* **1995,** 454, 327.

101. Allamandola, L. J.; Bernstein, M. P.; Sandford, S. A.; Walker, R. L., *Space Sci. Rev.* **1999,** 90, 219.

102. Woon, D. E., *Icarus* **2001,** 149, 227.

103. Schutte, W.; Greenberg, J. M., *Light on Dark Matter*. Reidel: Dordrecht, 1986; p 229.

104. Kobayashi, K.; Kasamatsu, T.; Kaneko, T.; Koike, J.; Oshima, T.; Saito, T.; Yamamoto, T.; Yanagawa, H., *Adv. Space Res.* **1995,** 16, 21.

105. Schutte, W. A.; Allamandola, L. J.; Sandford, S. A., *Icarus* **1993,** 104, 118.

106. Hudson, R. L.; Moore, M. H., *Icarus* **1999,** 140, 451.

107. McCoustra, M.; Williams, D. A., *Mon. Not. R. Astron. Soc.* **1996,** 279, L53.

108. Hammam, E.; Lee, E. P. F.; Dyke, J. M., *J. Phys. Chem. A* **2000,** 104, 4571.

109. Bianco, R.; Hynes, J. T., *Int. J. Quantum Chem.* **1999,** 75, 683.

110. Pierazzo, E.; Chyba, C. F., *Meteor. Planet. Sci.* **1999,** 34, 909.

111. Scott, A. P.; Radom, L., *J. Phys. Chem.* **1996,** 100, 16502.

112. Frisch, M. J. *Gaussian98*, Revision A. 7; Gaussian Inc.: Pittsburgh, PA, 1998.

113. Woon, D. E., *Icarus* **1999,** 142, 550.

114. Williams, I. H., *J. Am. Chem. Soc.* **1987,** 109, 6299.

115. Donaldson, D. J., *J. Phys. Chem. A* **1999,** 103, 62.

116. Jursic, B. S., *J. Mol. Struct. (Theochem)* **1999,** 490, 1.

117. Peterson, K. A.; Xantheas, S. S.; Dixon, D. A.; Dunning Jr, T. H., *J. Phys. Chem. A* **1998,** 102, 2449.

118. Masella, M.; Flament, J.-P., A theoretical study of five water/ammonia/formaldehyde cyclic trimers:influence of cooperative effects. *J. Chem. Phys.* **1999,** 110, (15), 7245.

119. Schafer, L.; Cao, M.; Ramek, M.; Teppen, B. J.; Newton, S. Q.; Siam, K., Conformational geometry functions: additivity and cooperative effects. *J. Mol. Struct. (Theochem)* **1997,** 413-414, 175.

120. Guo, H.; Salahub, D. R., Cooperative Hydrogen Bonding and Enzyme Catalysis. *Angew. Chem. Int. Ed.* **1998,** 37, (21), 2985.

121. Rulisek, L.; Havlas, Z., Theoretical Studies of Metal Ion Selectivity. 2. DFT Calculations of Complexation Energies of Selected Transition Metal Ions (Co2+, Ni2+, Cu2+, Zn2+, Cd2+, and Hg2+) in Metal-Binding Sites of Metalloproteins. *J. Phys. Chem. A* **2002,** 106, 3855.

122. Masella, M.; Gresh, N.; Flament, J.-P., *J. Chem. Soc., Faraday Trans.* **1998,** 94, 2745.

123. Van der Rest, G.; Masella, M., Do Cooperative Effects Influence the Bending HOH Vibrational Spectra of Small (H2O)n Clusters (n=2-4)? *J. Mol. Spectrosc.* **1999,** 196, 146.

124. Xantheas, S. S., *J. Chem. Phys.* **1994,** 100, 7523.

125. Lankau, T., (H2O)6 on a Virtual Metal Surface: Many-Body Effects in the Bilayer Structure. *J. Phys. Chem. A* **2002,** 106, 6154.

126. Masella, M., Cooperative effects in water tetramers. Comparison between the empirical many-body model TCPE and ab initio calculations. *C. R. Acad. Sci. Paris / physical and theoretical chemistry* **1998,** 1, (II c), 441.

127. Mo, O.; Yanez, M.; Elguero, J., Cooperative (nonpairwise) effects in water trimers: An ab initio molecular orbital study. *J. Chem. Phys.* **1992,** 97, (9), 6628.

128. Vorobyov, I.; Yappert, M. C.; DuPre, D. B., Energetic and Topological Analyses of Cooperative σH- and πH-Bonding Interactions. *J. Phys. Chem. A* **2002,** 106, 10691.

129. Nilsson, A.; Ogasawara, H.; Cavalleri, M.; Nordlund, D.; Nyberg, M.; Wernet, P.; Pettersson, L. G., The hydrogen bond in ice probed by soft x-ray spectroscopy and density functional theory. *J. Chem. Phys.* **2005,** 122, (15), 154505.

130. Hirata, S.; Iwata, S., Ab Initio Hartree-Fock and Density Functional Studies on the Structures and Vibrations of an Infinite Hydrogen Fluoride Polymer. *J. Phys. Chem. B* **1998,** 102, (43), 8426.

131. Lozynski, M.; Rusinska-Roszak, D.; Mack, H.-G., Hydrogen Bonding and Density Functional Calculations: The B3LYP Approach as the Shortest Way to MP2 Results. *J. Phys. Chem. A* **1998,** 102, (17), 2899.

132. Sirois, S.; Proynov, E. I.; Nguyen, D. T.; Salahub, D. R., Hydrogen-bonding in glycine and malonaldehyde: Performance of the Lap1 correlation functional. *J. Chem. Phys.* **1997,** 107, (17), 6770.

133. Calhorda, M. J., Weak hydrogen bonds: theoretical studies. *Chem. Commun.* **2000,** 801.

134. Oliveira, B. G.; Pereira, F. S.; de Araujo, R. C. M. U.; Ramos, M. N., The hydrogen bond strenght: New proposals to evaluate the intermolecular interaction using DFT calculations and the AIM theory. *Chem. Phys. Lett.* **2006,** 427, 181.

135. Tsuzuki, S.; Luthi, H. P., Interaction energies of van der Waals and hydrogen bonded systems calculated using density functional theory: Assessing the PW91 model. *J. Chem. Phys.* **2001,** 114, (9), 3949.

136. Van der Wijst, T.; Fonseca Guerra, C.; Swart, M.; Bickelhaupt, F. M., Performance of various density functionals for the hydrogen bonds in DNA base pairs. *Chem. Phys. Lett.* **2006,** 426, 415.

137. Gonzalez, L.; Mo, O.; Yanez, M.; Elguero, J., Cooperative effects in water trimers. The performance of density functional approaches. *J. Mol. Struct. (Theochem)* **1996,** 371, 1.

138. Masella, M.; Flament, J.-P., Relation between cooperative effects in cyclic water, methanol/water, and methanol trimers and hydrogen bonds in methanol/water, ethanol/water, and dimethylether/water heterodimers. *J. Chem. Phys.* **1998,** 108, (17), 7141.

139. Casassa, S.; Calatayud, M.; Doll, K.; Minot, C.; Pisani, C., Proton ordered cubic and hexagonal periodic models of ordinary ice. *Chem. Phys. Lett.* **2005,** 409, 110.

140. Kresse, G.; Hafner, J., *Phys. Rev. B* **1994,** 49, 14251.

141. Perdew, J. P.; Chevary, J. A.; Vosko, S. H.; Jackson, K. A.; Pederson, M. R.; Singh, D. J.; Fiolhais, C., *Phys. Rev. B* **1992,** 46, 6671.

142. Kresse, G.; Hafner, J., *J. Phys. Condens. Matter* **1994,** 6, 8245.

143. Monkhorst, H. J.; Pack, J. D., *Phys. Rev. B* **1976,** 13, 5188.

144. Stohr, J., *NEXAFS Spectroscopy*. Springer Verlag: Berlin, 1992.

145. Naslund, L.-A. "Probing unoccupied electronic states in aqueous solutions." Ph.D. diss. Stockholm University, Stockholm, Sweden, 2004.

146. Rehr, J. J.; Albers, R. C., Theoretical approaches to x-ray absorption fine structure. *Rev. Mod. Phys.* **2000,** 72, (3), 621.

147. Cabaret, D. XANES: approche monoélectronique. http://www-ext.lmcp.jussieu.fr/~cabaret/transp_aussois06.pdf

148. Cavalleri, M. "Local Structure of Hydrogen-Bonded Liquids." Ph.D. diss. Stockholm University, Stockholm, Sweden, 2004.

149. Cabaret, D. Spectroscopie d'absorption X au voisinage des seuils:une introduction sur les méthodes d'interprétation. http://www-ext.lmcp.jussieu.fr/~cabaret/coursSESTEA1.pdf

150. Slater, J. C., *Adv. Quant. Chem.* **1972,** 6, 1.

151. Janak, J. F., Proof that dE/dni=ei in density-functional theory. *Phys. Rev. B* **1978,** 18, (12), 7165.

152. Valiev, M. M.; Fernando, G. W., Occupation numbers in density-functional calculations. *Phys. Rev. B* **1995,** 52, (15), 10697.

153. Goransson, C.; Olovsson, W.; Abrikosov, I. A., Numerical investigation of the validity of the Slater-Janak transition-state model in metallic systems. *Phys. Rev. B* **2005,** 72, 134203.

154. Plashkevych, O.; Agren, H.; Karlsson, L.; Pettersson, L. G. M., Calculations of valence electron binding energies using Kohn-Sham theory and transition potentials. *J. Elec. Spec. Relat. Phenom.* **2000,** 106, 51.

155. Triguero, L.; Pettersson, L. G. M.; Agren, H., Calculations of X-ray emission spectra of molecules and surface adsorbates by means of density functional theory. *J. Phys. Chem. A* **1998,** 102, 10599.

156. Triguero, L.; Pettersson, L. G. M.; Agren, H., Calculations of near-edge x-ray-absorption spectra of gas-phase and chemisorbed molecules by means of density-functional and transition-potential theory. *Phys. Rev. B* **1998,** 58, (12), 8097.

157. Triguero, L.; Luo, Y.; Pettersson, L. G. M.; Agren, H.; Vaterlein, P.; Weinelt, M.; Fohlisch, A.; Hasselstrom, J.; Karis, O.; Nilsson, A., Resonant soft-x-ray emission spectrascopy of surface adsorbates: theory, computations, and mesurements of ethylene and benzene on Cu(110). *Phys. Rev. B* **1999,** 59, (7), 5189.

158. Hermann, K.; Pettersson, L.; Casida, M.; Daul, C.; Goursot, A.; Koester, A.; Proynov, E.; St-Amant, A.; Salahub, D. *STOBE Software*, 2002.

159. Perdew, J. P.; Burke, K.; Ernzerhof, M., Generalized Gradient Approximation Made Simple. *Phys. Rev. Lett.* **1996,** 77, (18), 3865.

160. te Velde, G.; Baerends, E. J., Precise density-functional method for periodic structures. *Phys. Rev. B* **1991,** 44, (15), 7888.

161. Delphenich, D. H. A geometric origin for the Madelung potential. http://arxiv.org/ftp/gr-qc/papers/0211/0211065.pdf

162. Gutdeutsch, U.; Birkenheuer, U.; Kruger, S.; Rosch, N., On cluster embedding schemes based on orbital space partitioning. *J. Chem. Phys.* **1997,** 106, (14), 6020.

163. Boese, A. D.; Martin, J. M. L.; Handy, N. C., The role of the basis set: assessing density functional theory. *J. Chem. Phys.* **2003,** 119, (6), 3005.

164. van Wullen, C.; Kutzelnigg, W., The MC-IGLO method. *Chem. Phys. Lett.* **1993,** 205, (6), 563.

165. Schindler, M.; Kutzelnigg, W., Theory of magnetic susceptibilities and NMR chemical shifts in terms of localized quantities. II. Application to some simple molecules. *J. Chem. Phys.* **1982,** 76, (4), 1919.

166. Kutzelnigg, W.; Fleischer, U.; Schindler, M., *NMR-Basic Principles and Progress.* Springer: Heidelberg, 1990.

167. Pettersson, L. G. M.; Wahlgren, U.; Gropen, O., Effective Core Potential. *J. Chem. Phys.* **1987,** 86, 2176.

168. Myneni, S., Spectroscopic probing of local hydrogen-bonding structures in liquid water. *J. Phys.: Condens. Matter* **2002,** 14, L213-L219.

169. Grand, D.; Bernas, A.; Amouyal, E., *Chem. Phys.* **1979,** 44, 73.

170. Coe, J. V.; Earhart, A. D.; Cohen, M. C.; Hoffman, G. J.; Sarkas, H. W.; Bowen, K. H., *J. Chem. Phys.* **1997,** 107, 6023.

171. Cabral do Couto, P.; Guedes, R. C.; Costa Cabral, B. J., The density of states and band gap of liquid water by sequential Monte Carlo/Quantum mechanics calculations. *Braz. J. Phys.* **2004,** 34, (1), 42.

172. Cai, Y. Q.; Mao, H.-K.; Chow, P. C.; Tse, J. S.; Ma, Y.; Patchkovskii, S.; Shu, J. F.; Struzhkin, V.; Hemley, R. J.; Ishii, H.; Chen, C. C.; Jarrige, I.; Chen, C. T.; Shieh, S. R.; Huang, E. P.; Kao, C. C., Ordering of hydrogen bonds in high-pressure low-temperature H2O. *Phys. Rev. Lett.* **2005,** 94, 025502.

173. Bergmann, U.; Wernet, P.; Glatzel, P.; Cavalleri, M.; Pettersson, L. G. M.; Nilsson, A.; Cramer, S. P., X-ray Raman spectroscopy at the oxygen K edge of water and ice: implications on local structure models. *Phys. Rev. B* **2002,** 66, 092107.

174. Cavalleri, M.; Ogasawara, H.; Pettersson, L. G. M.; Nilsson, A., The interpretation of X-ray absorption spectra of water and ice. *Chem. Phys. Lett.* **2002,** 364, 363.

175. Wilson, K. R.; Cavalleri, M.; Rude, B. S.; Schaller, R. D.; Nilsson, A.; Pettersson, L. G. M.; Goldman, N.; Catalano, T.; Bozek, J. D.; Saykally, R. J., Characterization of hydrogen bond acceptor molecules at the water surface using near-edge x-ray absorption fine-structure spectroscopy and density functional theory. *J. Phys.: Condens. Matter* **2002,** 14, L221.

176. Odelius, M.; Cavalleri, M.; Nilsson, A.; Pettersson, L. G. M., X-ray absorption spectrum of liquid water from molecular dynamics simulations: asymmetric model. *Phys. Rev. B* **2006,** 73, 024205.

177. Naslund, L.-A.; Luning, J.; Ufuktepe, Y.; Ogasawara, H.; Wernet, P.; Bergmann, U.; Pettersson, L. G. M.; Nilsson, A., X-ray absorption spectroscopy measurements of liquid water. *J. Phys. Chem.* **2005,** 109, 13835.

178. Odelius, M.; Ogasawara, H.; Nordlund, D.; Fuchs, O.; Weinhardt, L.; Maier, F.; Umbach, E.; Heske, C.; Zubavichus, Y.; Grunze, M.; Denlinger, J. D.; Pettersson, L. G. M.; Nilsson, A., Ultrafast core-hole-induced dynamics in water probed by x-ray emission spectroscopy. *Phys. Rev. Lett.* **2005,** 94, 227401.

179. Nilsson, A.; Wernet, P.; Nordlund, D.; Bergmann, U.; Cavalleri, M.; Odelius, M.; Ogasawara, H.; Naslund, L.-A.; Hirsch, T. K.; Ojamae, L.; Glatzel, P.; Pettersson, L. G. M., Comment on "energetics of hydrogen bond network rearrangements in liquid water". *Science* **2005,** 308, (5723), 793a.

180. Hakala, M.; Nygard, K.; Manninen, S.; Huotari, S.; Buslaps, T.; Nilsson, A.; Pettersson, L. G. M.; Hamalainen, K., Correlation of hydrogen bond lenghts and angles in liquid water based on Compton scattering. *J. Chem. Phys.* **2006,** 125, 084504.

181. Nygard, K.; Hakala, M.; Manninen, S.; Andrejczuk, A.; Itou, M.; Sakurai, Y.; Pettersson, L. G. M.; Hamalainen, K., Compton scattering study of water versus ice Ih: intra and intermolecular structure. *Phys. Rev. E* **2006,** 74, 031503.

182. Prendergast, D.; Galli, G., X-ray absorption spectra of water from first principles calculations. *Phys. Rev. Lett.* **2006,** 96, 215502.

183. Guo, J.-H.; Luo, Y.; Augustsson, A.; Rubensson, J.-E.; Sathe, C.; Agren, H.; Siegbahn, H.; Nordgren, J., X-ray emission spectroscopy of hydrogen bonding and electronic structure of liquid water. *Phys. Rev. Lett.* **2002,** 89, (13), 137402.

184. Prendergast, D.; Grossman, J. C.; Galli, G., The electronic structure of liquid water within density-functional theory. *J. Chem. Phys.* **2005,** 123, 014501.

185. Cavalleri, M.; Odelius, M.; Nordlund, D.; Nilsson, A.; Pettersson, L. G. M., Half or full core hole in density functional theory X-ray absorption spectrum calculations of water? *Phys. Chem. Chem. Phys.* **2005,** 7, (15), 2854.

186. Cavalleri, M.; Odelius, M.; Nilsson, A.; Pettersson, L. G. M., X-ray absorption spectra of water within a plane-wave Car-Parrinello molecular dynamics framework. *J. Chem. Phys.* **2004,** 121, (20), 10065.